MAGNETRON SPUTTERING GROWTH OF AZO / ZnO / Zn(O,S) MULTILAYERS FOR Cu_2ZnSnS_4 THIN FILM SOLAR CELLS: MATERIAL AND DEVICE CHARACTERIZATION

A Thesis submitted to
The Graduate School of Engineering and Science of
İzmir Institute of Technology
in Partial Fulfillment of the Requirements for the Degree of

DOCTORA OF PHILOSOPHY

in Materials Science and Engineering

by
Fulya KÖSEOĞLU

June 2017
İZMİR

We approve the thesis of **Fulya KÖSEOĞLU**

Examining Committee Members:

Prof. Dr. Lütfi ÖZYÜZER
Department of Physics, İzmir Institute of Technology

Prof. Dr. E. Sıddık İÇLİ
Solar Energy Institute, Ege University

Asst. Prof. Dr. Enver TARHAN
Department of Physics, İzmir Institute of Technology

Assoc. Prof. Dr. Ekrem ÖZDEMİR
Department of Chemical Engineering, İzmir Institute of Technology

Asst. Prof. Dr. Özge SAĞLAM
Department of Mechanical Engineering, İzmir University of Economics

20 June 2017

Prof. Dr. Lütfi ÖZYÜZER
Supervisor, Department of Physics
İzmir Institute of Technology

Assoc. Prof. Dr. Gülnur Aygün ÖZYÜZER
Co-Supervisor, Department of Physics
İzmir Institute of Technology

Prof. Dr. Mustafa M. DEMİR
Head of the Department of
Material Science and Engineering

Prof. Dr. Aysun SOFUOĞLU
Dean of the Graduate School of
Engineering and Sciences

To my Family…

ACKNOWLEDGEMENTS

First of all, I would like to express my gratitude to Prof. Dr. Lütfi Özyüzer for giving me the possibility of carrying out this work under his supervision. I appreciate him, for his instructive guidance, inspiring suggestions, encouragement and understanding throughout the preparation of this thesis. I also would like to acknowledge Assoc. Prof. Dr. Gülnur Aygün Özyüzer for her contribution to this thesis.

I wish to extend my thanks to İzmir Institute of Technology for providing Research Assistantship throughout my graduate study, to TUBITAK for funding the project ‘‘TBAG-114F341’’ and to Applied Quantum Research Center (AQuReC) for their facilities during my thesis.

I am also very thankful to my colleagues from İzmir Institute of Technology and my group members, especially, F. Gülşah Akça, Şebnem Yazıcı, Ayten Cantaş, Dilara Gökçen Buldu and Ece Meriç for their helps and creating a nice environment while studying together.

I am thankful to my family for their unconditional love, unending support and understanding during my whole life and providing me with more than I can ever repay them for. I would like to express my deepest thanks to my husband, Hasan Köseoğlu, for his love, support and encouragement over the past fourteen years, and for his unwavering belief in me even when I doubted myself. Last, but not least, I would like to thank to my little sunshine, Defne Köseoğlu, who make me happy with a kiss or smile even when I feel so desperate.

ABSTRACT

MAGNETRON SPUTTERING GROWTH OF AZO / ZnO / Zn(O,S) MULTILAYERS FOR Cu_2ZnSnS_4 THIN FILM SOLAR CELLS: MATERIAL AND DEVICE CHARACTERIZATION

Cu_2ZnSnS_4 (CZTS) absorber layer attracts so much attention in photovoltaic industry since it contains earth abundant, low cost and non-toxic elements contrary to other chalcogenide based solar cells such as $CuInGa(S,Se)_2$ (CIGS) and CdTe. Although, CZTS studies have been newly started, recently 9.4 % efficiency has been achieved. In the present thesis, all layers used in the CZTS device structure were investigated using energy-dispersive X-ray spectroscopy (EDX), X-ray diffraction (XRD), scanning electron microscopy (SEM), spectrophotometry and Raman spectroscopy. For CZTS absorber layer, CZTS films based on a stacked precursor (Cu/Sn/Zn/Cu) were prepared. The effect of sulfurization time and the thickness of top and bottom Cu layer in precursors on the properties of CZTS thin films were investigated. We addressed the importance of Cu layer thickness adjacent to Sn to avoid developing detrimental phases and to get complete formation of kesterite CZTS absorber layer. We also addressed the importance of sulfurization time to restrict the Sn and Zn losses, formation of oxides such as SnO_2 and ZnO, formation of MoS_2 and voids between Mo/CZTS interface. Effect of the sulfur concentration on the properties of Zn(O,S) thin films were investigated. We showed that key parameters such as energy gap and crystal structure of the Zn(O,S) thin films can be tuned by changing the sulfur concentrations of the films. We succeed substitute conventionally used CdS buffer layer with environmentally friendly alternative Zn(O,S) buffer layer in CZTS solar cells. Effect of substrate position and rotation speed during the deposition of AZO thin films were investigated. We addressed that stress on the films can be significantly reduced by off-center deposition and rotating the sample holder during the deposition. In this way, high transmission in the visible range and metal like resistivity were achieved simultaneously at room temperature. We observed strong dependence of device performances on both sulfurization time and the thickness of Cu layer adjacent to Sn in CZTS absorber. The best device was based on CZTS films sulfurized for 30 minutes and having thicker Cu layer adjacent to Sn layer in precursors.

ÖZET

Cu_2ZnSnS_4 İNCE FİLM GÜNEŞ HÜCRELERİ İÇİN AZO / ZnO / Zn(O,S) ÇOKLU KATMANLARININ MIKNATISSAL SAÇTIRMA İLE BÜYÜTÜLMESİ: MALZEME VE AYGIT KARAKTERİZASYONU

$CuInGa(S,Se)_2$ (CIGS) ve CdTe gibi diğer kalkojenit esaslı güneş pillerinin aksine düşük maliyetli, yeryüzünde bol miktarda bulunan ve toksik olmayan elementler içerdiğinden Cu_2ZnSnS_4 (CZTS) soğurucu tabaka fotovoltaik endüstrisinde çok dikkat çekmektedir. CZTS çalışmaları yeni başlatılmış olsa da, son zamanlarda CZTS güneş hücrelerinden % 9.4'lük bir verimlilik elde edilmiştir. Mevcut çalışmada, CZTS cihaz yapısında kullanılan tüm katmanlar, enerji dağılımlı X-ışını spektroskopisi (EDX), X-ışını kırınımı (XRD), taramalı elektron mikroskobu (SEM), spektrofotometri ve Raman spektroskopisi kullanılarak incelenmiştir. CZTS soğurucu tabaka için, istiflenmiş öncül katman bazlı (Cu/Sn/Zn/Cu) CZTS filmleri hazırlanmıştır. Sülfürleme süresinin ve öncül katmanlardaki üst ve alttaki Cu tabakasının kalınlıklarının CZTS ince filmlerinin özellikleri üzerine olan etkisi araştırılmıştır. Zararlı fazların gelişmesini önlemek ve kesterit CZTS soğurucu katmanın tam oluşumunu sağlamak için Sn'ye komşu Cu katman kalınlığının önemi belirtilmiştir. Sn ve Zn kayıplarını, SnO_2 ve ZnO gibi oksitlerin oluşumunu, Mo/CZTS ara yüzünde MoS_2'nin ve boşlukların oluşumunu sınırlamak için sülfürleme süresinin önemi de belirtilmiştir. Sülfür konsantrasyonunun Zn(O,S) ince filmlerin özelliklerine etkisi araştırılmıştır. Zn(O,S) ince filmlerin enerji aralığı ve kristal yapısı gibi anahtar parametrelerin, filmlerin sülfür konsantrasyonlarının değiştirilmesiyle ayarlanabileceği gösterilmiştir. Geleneksel olarak kullanılan CdS tampon tabakasının, CZTS güneş hücrelerinde çevre dostu alternatif Zn(O,S) tampon tabakasıyla değiştirilmesi başarılmıştır. AZO ince filmlerin kaplanması esnasında alttaş pozisyonunun ve örnek tutucu dönüş hızının etkisi araştırılmıştır. Filmler üzerindeki stresin filmlerin hedef ekseninden uzağa yerleştirilmesi ve kaplama sırasında örnek tutucunun döndürülmesi ile önemli ölçüde azaltılabileceği gösterilmiştir. Bu sayede, oda sıcaklığında, görünür aralıktaki yüksek geçirgenlik ve metal benzeri özdirenç elde edilmiştir. Cihaz performanslarının hem sülfürleme süresi hem de CZTS soğurucuda Sn'ye bitişik Cu tabakasının kalınlığı üzerine kuvvetli bir bağımlılık gözlemlenmiştir. En iyi cihaz 30 dakika boyunca sülfürlenen ve öncüllerde Sn tabakasına bitişik kalın Cu tabakasına sahip olan CZTS filmlerine dayanmaktadır.

TABLE OF CONTENT

LIST OF FIGURES

Figure **Page**

LIST OF TABLES

CHAPTER 1

INTRODUCTION

1.1. Overview

As the world population continues to increase, global energy demand is expected to increase by about 50% over the next 25 years (EIA, 2011). Currently, the main part of this energy demand (~83%) is being produced by fossil fuels such as coal, oil and natural gas (Conti et al., 2011). Due to the finiteness of fuels, the energy produced from these sources is becoming expensive. In addition, burning those fuels produce greenhouse gases, e.g. carbon dioxide and methane. These greenhouse gases absorb infrared radiation, contributing to global warming (Ramanathan et al., 2003). Due to abundant availabilities and ecofriendly natures, renewable energy sources seem to provide an optimal solution to the global energy problem. Among the other renewable energy sources, solar energy is of particular interest because it is the only renewable source that can potentially cover the world's energy consumption. Solar energy reaching the Earth's surface within an hour is almost equal to the world's energy consumption within a year (Zhu, Long, & Ort, 2008). Photovoltaic (PV) technology, which converts solar radiation directly into electricity by solar cells, is still not competitive with fossil fuel generation of electricity due to high cost of electricity production. In order to provide widespread use of solar cells, their production and installation cost should be competitive with current sources of electricity (Wadia, Alivisatos, & Kammen, 2009). Crystalline silicon (c-Si) and multi-crystalline silicon (mc-Si) are the most commonly used material for solar panels. In the laboratory scale, best efficiencies obtained by sc-Si and mc-Si solar cells are 25.6 % (Masuko et al., 2014) and 21.25 % (Green, Emery, Hishikawa, Warta, & Dunlop, 2016), respectively, whereas the records for silicon modules are 22.9 % for sc-Si and 18.5 % for mc-Si (Green et al., 2016). Although a relatively high efficiency can be achieved by using c-Si as a light absorber material, Si solar modules require a high budget for manufacturing. Since silicon has an indirect band gap, a few hundred micrometers in thickness of wafers are necessary to absorb sufficient energy from sunlight to have high efficiencies. Thin film solar cells are emerging as an alternative technology to a traditional

wafer based crystalline solar cells. Although these thin film solar cells are generally less efficient than single crystalline silicon cells, they are cost competitive with Si cells by avoiding expensive single crystal processing steps and reducing material usage. Since the absorption coefficient of typical thin film absorber materials is about 100 times higher than that of the crystalline silicon, thin film material with 100 times thinner than crystalline silicon, can absorb an equivalent amount of energy as crystalline silicon. Moreover, since the grain boundaries in thin films materials increase charge separation and transport, and allow only negligible recombination, purity and crystal quality requirements on thin film solar cell materials are less stringent than crystalline silicon solar cells (Li, Chawla, & Clemens, 2012).

Currently, there exist two major thin film technologies that have been commercialized, namely cadmium telluride (CdTe) and copper indium gallium diselenide ($CuIn_xGa_{1-x}S(e)_2$, or CIGS). These technologies have high conversion efficiencies both in commercial production and in laboratory scale. Conversion efficiencies reached recently up to 22.1 % (Solar, 2011) for CdTe and 21.7 % (Jackson et al., 2015) for CIGS (NREL, 2015). Despite the higher conversion efficiencies of these semiconductors, the toxicity of Cd element and availability problem and high cost of In and Ga elements, restrict the production capacity of these thin film solar cells. Figure 1.1. illustrate the cost and abundance of these materials in the earth's crust. Non-toxic and earth abundant materials are needed for long term viability of thin films solar cells. One such material is Cu_2ZnSnS_4; commonly known as CZTS. Since this material is non-toxic and its component elements are abundant in the earth's crust, CZTS solar cells are free from both resource-saving concerns and environmental pollution (Figure 1.1.). In addition, CZTS is a p-type semiconductor with talented physical properties, such as the direct band gap of 1.5 eV, high optical absorption coefficient ($>10^{-4}$ cm^{-1}), low thermal conductivity etc. (Katagiri, Ishigaki, Ishida, & Saito, 2001). Band gap of CZTS is ideal to convert the maximum amount of energy from the solar spectrum into electricity (Katagiri et al., 1997). Owing to its high absorption coefficient, only a few microns thick layer of CZTS is enough to absorb all the photons with energies above its band gap (Katagiri et al., 1997). Due to these important features, CZTS is expected to be one of the promising materials for thin film solar cells. To date, the world record efficiencies of 9.2 % and 9.4 % for pure sulfide CZTS solar cell have been achieved by Hiroi, et al. 2013 (Hiroi, Sakai, Kato, & Sugimoto, 2013) and Tajima, et al. 2017 (Tajima, Umehara, Hasegawa, Mise, & Itoh, 2017), respectively. Although this is somewhat less efficient than the current efficiencies

of other technologies, it offers a cost-effective solution by utilizing less expensive materials and large-scale production.

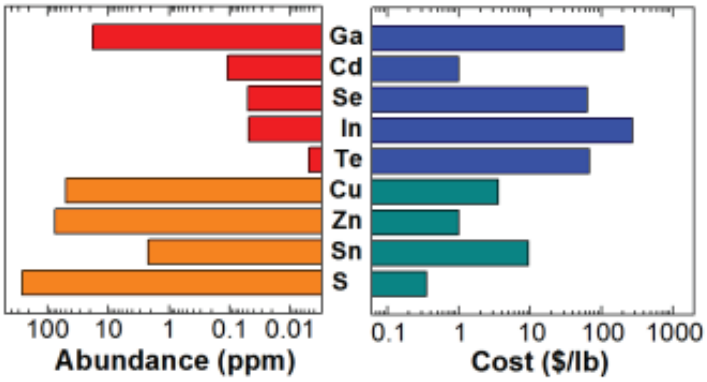

Figure 1.1. A comparison of the abundance in the earth's crust and cost of the various elements used for manufacturing thin film solar cells. Data is plotted on a logarithmic scale.

Currently the standard technique of producing CZTS solar cells is to use cadmium sulphide (CdS) grown by chemical bath deposition (CBD) as buffer layer. Although yielding the best device performance, there are some debates on the fundamental issues with this buffer layer, first because it contains cadmium, which is toxic, secondly because the CBD process implies additional production costs compared to the dry process when industrially implemented. In addition, the usage of a material with a wider bandgap than CdS ($E_{g(CdS)}$=2.4 eV) (Weinhardt et al., 2005) could lead to increase in the cell performance due to minimization of the photon loss in the blue wavelength range. Therefore, alternative materials are being sought that can replace this layer with something that is environmentally suitable and that does not lower the performance. Among the different alternatives to CdS, $ZnO_{1-x}S_x$ (Zn(O,S)) alloys has emerged to be one of the most promising candidates for this purpose, and high efficiency devices up to 21 % efficiency have already been reported for CIGS.

Aluminum doped zinc oxide (AZO) thin film is currently most used material for CZTS solar cells to make transparent conducting electrode. During the growth of AZO, a high deposition temperature is necessary to improve the crystallinity of the films and get a desired transparent conducting oxide (TCO) property. However, a room temperature (RT) deposition process is required to avoid inter-diffusion between the layers of a solar cell.

1.2. Aim of The Thesis

This thesis is devoted to the development of relatively new, rapidly developing Cu_2ZnSnS_4 thin film solar cells. The objectives of this thesis are to:

1) provide easy adaptation to large-scale and reproducible manufacturing of the CZTS solar cells using only the magnetron sputtering technique for all thin films in the CZTS solar cell structure.
2) optimize the sputtering conditions and sulfurization parameters of the precursor to get CZTS absorber with desired properties.
3) investigate the effect of sulfurization time and precursor stacking on the opto-electronic properties of CZTS films.
4) substitute conventionally used CdS buffer layer with environmentally friendly alternative Zn(O,S) buffer layer.
5) analyze how to material properties of Zn(O,S) layer affect the solar cell performance.
6) get a desired TCO property for AZO thin film deposited at room temperature.

CHAPTER 2

BASIC CONCEPTS OF SOLAR CELLS

A solar cell is an opto-electronic device which directly converts the energy of sun into electricity by the photoelectric effect. All solar cells are based on semiconductor p-n junction. When the sunlight is absorbed, an electron-hole pair is produced, and segregated by the junction producing a current flow and a voltage across the contacts (see Figure 2.1.). Metal contacts at the edges of the p-n junction allow power dissipation when the solar cell is connected to a load. The basic concepts of solar cells are discussed below.

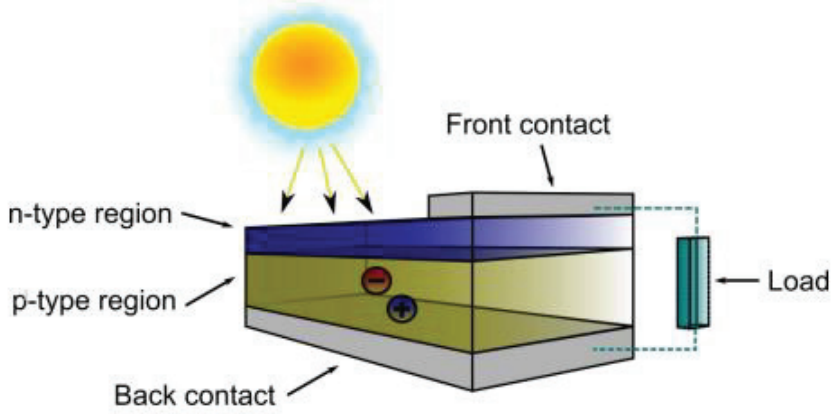

Figure 2.1. Schematic of a solar cell.

2.1. Solar Energy

Among the other renewable energy sources, solar energy is of particular interest because it is the only renewable source that can potentially cover the world's energy consumption. Massive amounts of power, 10^{26} W (Williams, 2004), is generated by the sun. Only a small part of that power reaches the Earth's surface, approximately 1000 W/m^2 (Green, 1992), far exceeding human demand several times (Chopra & Das, 1983).

The sun completely absorbs all kinds of radiation and emits a temperature-dependent black body radiation. The spectrum looks like the orange line in Figure 2.2., which corresponds to the irradiance of the sun at 5800 K. When photons enter the atmosphere, some wavelengths are absorbed by water, oxygen, ozone and other

molecules in the atmosphere and the spectral irradiance looks like the black curve. The radiation just outside the earth's is denoted with AM0. AM stands for Air Mass and indicates the path length of sun light through the atmosphere (Figure 2.3.).

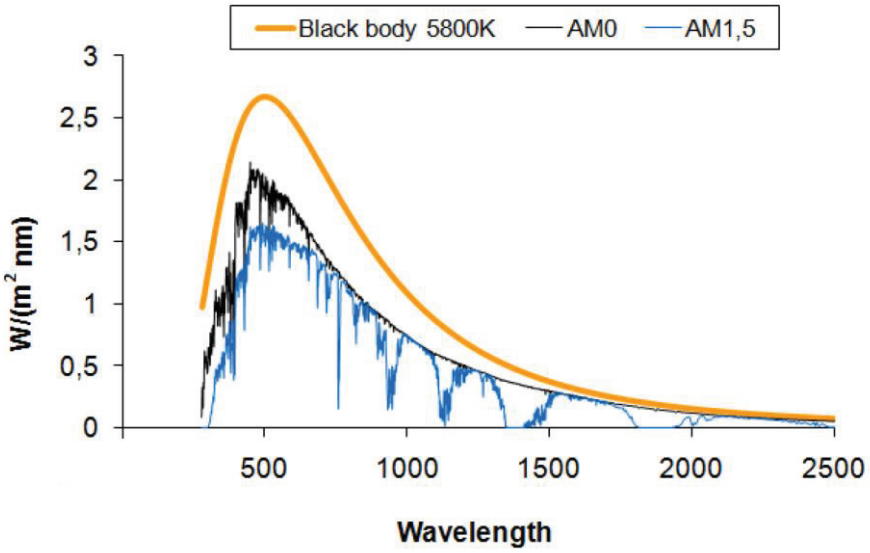

Figure 2.2. Spectral irradiance of the sun for different wavelengths.
(Source: Bird, Hulstrom, & Lewis, 1983)

The Air Mass is defined as $AM = 1/\cos(\theta)$, where θ is the angle between the position of sun and the zenith. AM1 represents that the radiation on earth's surface is perpendicular to incident light. The standard spectrum for measurements on solar cells is called AM1.5 (blue line in Figure 2.2.), which represents angle of incidence of 48 °.

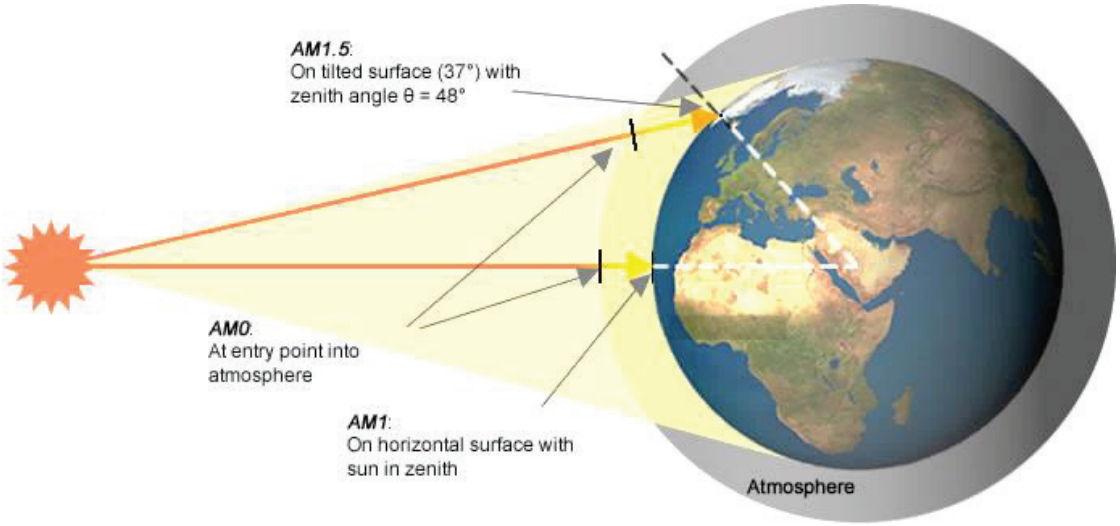

Figure 2.3. The path length of sun light through the atmosphere.
(Source: GreenRhinoEnergy, 2013)

2.2. Photovoltaic Effect

Photovoltaic effect is a process of direct conversion of light into electricity in a photovoltaic cell. When the energy of incident photons is equal to or higher than the bandgap of the semiconductor, the light is absorbed, and an electron is excited from the valence band (E_v) to the conduction band (E_c) bandgap of the semiconductor leaving a hole behind. This means that an electron-hole pair is created. The excited electron probably recombines rapidly with a hole. Electric field provided by a p-n junction avoid recombination, thus electric current and a voltage difference over the material is created.

2.3. p-type and n-type Semiconductors

Semiconductor is a material with electrical conductivity intermediate between that of metals and insulators. According to the position of the energy level of the atoms in the band gap of a semiconductor, there are two major types of impurities, donors and acceptors. Donors donate an electron to the conduction band of the semiconductor, while acceptors accept an electron from the valance band, in this manner creates a hole. Therefore, a semiconductor doped with impurities, which are ionized (since impurity atoms either have donated or accepted an electron) will therefore contain free charge carriers. Ionized donors provide an excess free electron in a semiconductor, which is then called n-type semiconductor, while an ionized acceptor provide free holes forms p-type semiconductor material.

2.4. p-n Junction

When a p-type and an n-type semiconductor are brought into contact with each other a p-n junction is formed between the two materials.

2.4.1. p-n Junction Under Equilibrium

Once the two semiconductors are in contact, because of the random thermal motion of the free electrons, electrons from the n-type region diffuse in the p-type region,

leaving behind positively charged donor atoms. Similarly, holes from the p-type region, diffuse in the n-type region, leaving behind negatively charged acceptor atoms. Because of this diffusion process, the region near the junction becomes almost completely depleted of mobile charge carriers. This region loses its neutrality and become charged and called as space charge region (or namely, depletion region). Regions outside the space charge region, the charge neutrality is conserved, this region is called as the quasi-neutral region (QNR).

The consequence of the formation of the space charge region at the junction is an electric field across the junction which allows the carriers to drift in the opposite direction to the diffusion current. That is, holes accelerate in the same direction of the field and electrons accelerate in the opposite direction of the field. When an equilibrium condition is reached, drift current balances the diffusion current and the net current becomes zero. At equilibrium, the electrochemical potential, which is represented by the Fermi energy, is constant. Figure 2.4. shows the schematic of the p-n junction under equilibrium condition.

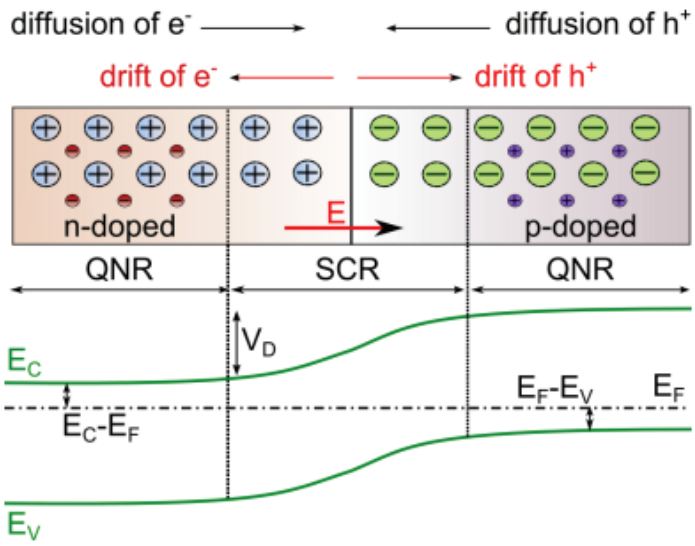

Figure 2.4. p-n junction under equilibrium condition. Electrons (red particles), holes (violet particles), donor atoms (blue particles), acceptor atoms (green particles).

The energy gap between Fermi level and the conduction/valence bands is the same in the QCR and is the same as in isolated n and p-type semiconductors. In SCR, conduction/valence bands are curved, which indicates the presence of an electric field. Presence of the internal electric field inside the p-n junction point out that there is a

potential difference, V, across the SCR. The n-type region becomes positive relative to the p type region since n-type region loose electrons, and p-type region receives electrons.

2.4.2. p-n Junction Under Bias

When an external voltage V is applied across the junction, there is no equilibrium anymore so that the drift and diffusion currents no longer compensate each other and a net current can flow.

If negative voltage is applied to the p-type region, the applied voltage will increase the potential difference across the p-n junction (Figure 2.5. and Figure 2.7. (a)), namely about the value eV. This is called as reverse biased condition. As the potential barrier across the junction is increased, the diffusion current vanishes at some point. The drift current, however, is relatively unchanged by the increased voltage since it is limited by the number of minority carriers on either side of the p-n junction. Due to the small increase in the width of the depletion region, drift current experience small increase. This increment is a second-order effect in silicon solar cells. However, in many thin film solar cells, where the depletion region is about half the thickness of the solar cell, the variation in the width of the depletion region with voltage has a great influence on cell operation.

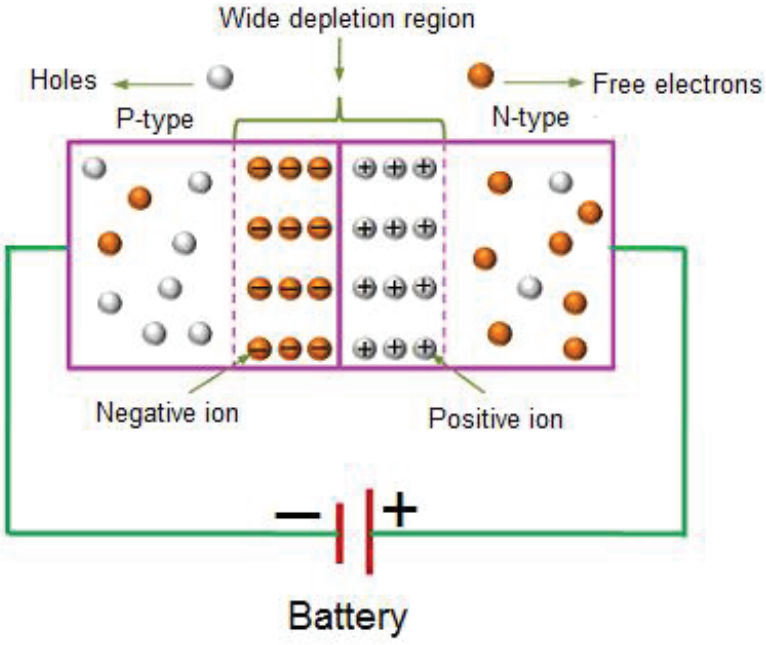

Figure 2.5. p-n junction under reverse bias condition.
(Source: Physics-and-Radio-Electronics, 2013)

If positive voltage is applied to the p-type region, the applied voltage will decrease the potential difference across the p-n junction (Figure 2.6. and Figure 2.7. (b)), that is, the electric field at the junction is reduced. This is called as forward biased condition. As the potential barrier across the junction is decreased, more free electrons from n-type region can now diffuse to the p-side. That means the diffusion current increases. At the same time, the drift current is unchanged since it depends on the number of carriers produced within a diffusion length of the depletion region. Since the depletion region is only reduced in width by a small amount, the number of minority carriers swept through the junction is substantially unchanged.

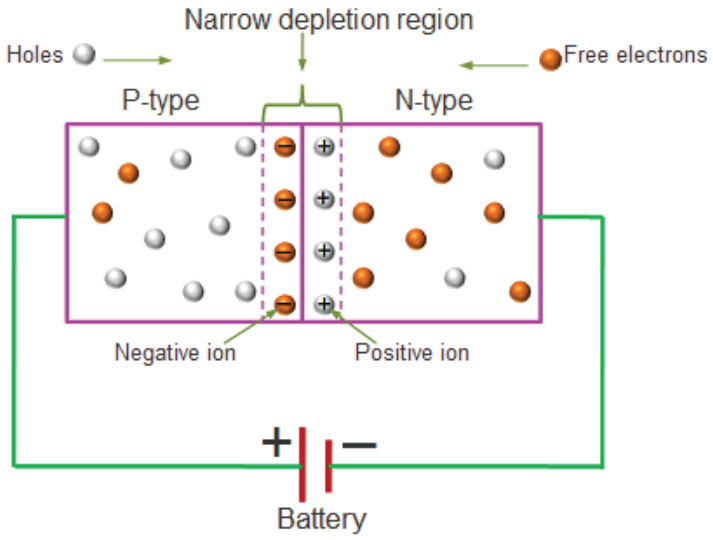

Figure 2.6. p-n junction under forward bias condition.
(Source: Physics-and-Radio-Electronics, 2013)

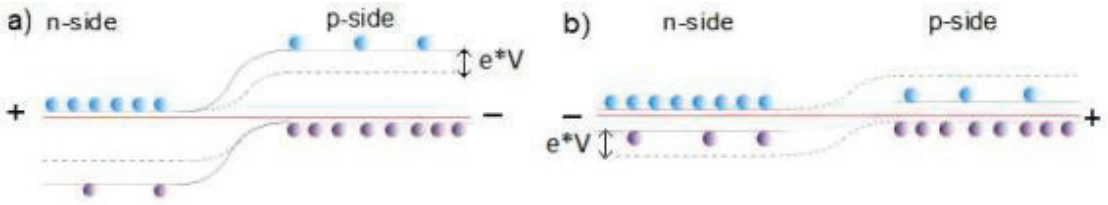

Figure 2.7. Band bending due to an applied voltage V. (a) reverse biased condition, (b) forward biased condition.

Shockley equation defines the current-voltage behavior of an ideal diode. The resulting formula of the total current I in a diode is given by;

$$I = I_0 \left(e^{\frac{qV}{kT}} - 1 \right) \tag{2.1}$$

where q is electronic charge, I_0 is the reverse saturation current, V is the applied external bias voltage, k is the Boltzmann constant and T is absolute temperature.

2.4.3. p-n Junction Under Illumination

When the junction is illuminated, photons with energy higher than the band gap energy of the semiconductors are absorbed and additional electron-hole pairs are generated in SCR and QCR.

Carriers generated in the SCR are easily swept out by the associated electric field at the junction. Electrons moves towards n-side region and holes towards p-side region. Carriers generated in the QCR, those within the diffusion length can reach the junction and will be pull to the other side. Only minority carriers will cross the junction. The electrons in the p-side will come toward the n-side and the holes in the n-side will come toward the p-side. Thus, there is a net increase of the negative charge in the n-side and the positive charge in the p-side. This causes a potential across the p-n junction due to the illumination of the junction and is known as the photovoltaic effect. Under illumination, the direction of the current flow is from n-side to p-side. This current is known as light generated current (I_L).

When the voltage is applied to the terminals of the illuminated p-n junction, the junction is exposed to both optical and electrical bias. Now, only a part of the photo-generated current flow through the external circuit. The electrochemical potential difference between the n-type and p-type regions is reduced by the voltage drop across the load. This leads to an increase in the recombination current by reducing the electrostatic potential on the depletion region. The net current through the load is determined by the sum of recombination current and light generated current. Under applied voltage, the net current of the illuminated p-n junction is given by;

$$I = I_0 \left(e^{\frac{qV}{kT}} - 1 \right) - I_L \tag{2.2}$$

2.4.4. I-V Characteristics of p-n Junction

The illuminated I-V characteristic of the p-n junction is represented in Figure 2.8. The curve follows the dark IV curve, shifts down to negative currents and keeps its shape.

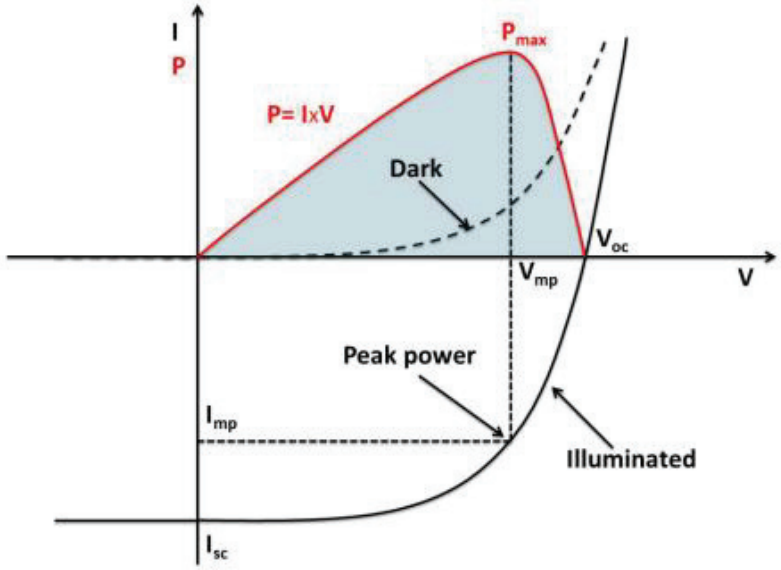

Figure 2.8. Dark and illuminated I-V characteristics of a solar cell.

In the typical current-voltage (I-V) curve of a solar cell there are some electrical parameters that determine the performance of solar cell, namely open circuit voltage (V_{oc}), short circuit current (I_{sc}), fill factor (FF) and efficiency (η) of the cell.

Short circuit current (I_{sc}) is defined as the current that is produced by a solar cell under illumination when the device is short-circuited. The short circuit current is due to the production and collection of light-generated carriers. The short-circuit current and the light-generated current are identical for an ideal solar cell. Therefore, the short circuit current is the maximum current delivered by a solar cell. In order to remove the dependence of the solar cell area, it is more common to use the short circuit current density (J_{sc} in mA/cm^2) to describe the maximum current delivered by a solar cell.

I_{sc} from a solar cell is strongly depends on the light intensity and the optical properties (band gap, absorption coefficient and reflection coefficient) of the solar cell material. Since every photon above the bandgap gives one charge carrier in the external circuit in an ideal device so the highest current is for the lowest bandgap material (Figure 2.9. (a)). It additionally depends on the collection probability of the solar cell, which is also mainly due to surface passivation and the minority carrier lifetime.

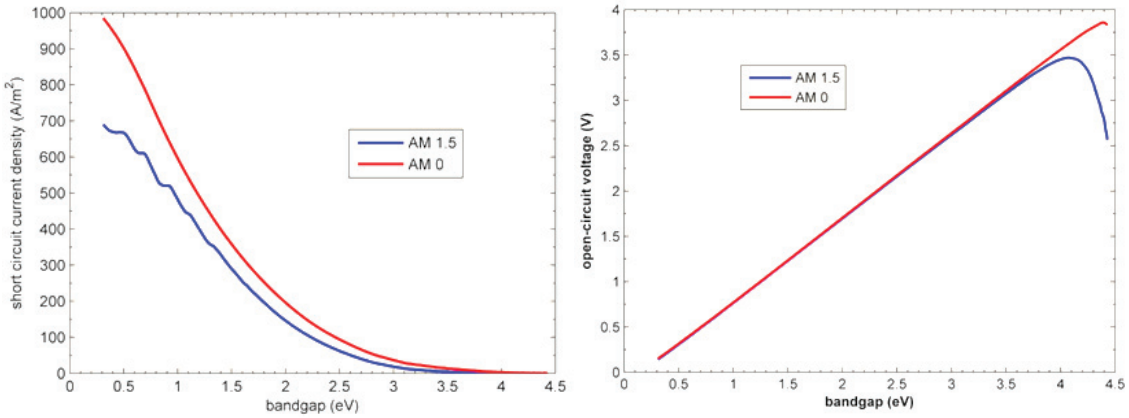

Figure 2.9. (a) I_{sc} and (b) V_{oc} as function of bandgap for a cell with AM 0 and AM 1.5.

Another important parameter is the open circuit voltage (V_{oc}), which is the maximum voltage that is available from a solar cell at zero current. No net current can flow inside the p-n junction under open circuit condition. It implies that the current originating from the flux of photo-generated and thermally-generated carriers must be balanced by the reverse recombination current. The recombination current increases through the reduction of the electrostatic-potential barrier along the depletion region by an amount V_{oc}. V_{oc} depends on light generated current. Assuming that the shunt resistance is sufficiently high to ignore the last term of the characteristic equation, V_{oc}, is given by;

$$V_{oc} \approx \frac{nkT}{q} \ln\left(\frac{I_L}{I_0} - 1\right) \tag{2.3}$$

This equation implies that the I_0 should be lower for higher V_{oc}. V_0 is actually a measure of the amount of recombination in the solar cell due to recombination dependence of I_0. It also depends on the band gap of the material, it increases with band gap since the recombination current reduces (Figure 2.9. (b)). Due to the very low I_{sc} at high band gaps, V_{oc} drop off.

Fill factor (FF), is a parameter which determines the maximum power that can be obtained from a solar cell. It is defined as the ratio of the maximum power from the solar cell to the product of V_{oc} and I_{sc} as given by the equation;

$$FF = \frac{V_m \times I_m}{V_{oc} \times I_{sc}} = \frac{P_{max.}}{V_{oc} \times I_{sc}} \tag{2.4}$$

Graphically, the FF is the measure of the area of the largest rectangle which will fit in the IV curve. Energy conversion efficiency (η) of a solar cell is defined as the ratio of the output energy (P_{max}) from the solar cell to input energy incident on the cell (P_{inc});

$$\eta = \frac{P_{max.}}{P_{inc.}} = \frac{V_{oc} \times I_{sc} \times FF}{P_{inc}} \tag{2.5}$$

Since solar cell efficiency depends on spectrum and intensity of incident sunlight and temperature of solar cell, efficiencies are measured under standard test conditions (STC) which specifies temperature of 25 °C and irradiance of 1000 W/m^2 with AM 1.5 spectrum.

2.5. Losses in Solar Cells

For an ideal solar cell with no losses, each photon striking the surface of the solar cell transfers its total energy to an electron-hole pair and all the carriers maintain the absorbed energy and transfer it to the contacts of the device. In this situation 100 % efficiency would be achieved. However, there are several loss mechanisms that reduce the possible efficiency of a solar cell. In the 1960s, the theoretical performance of a solar cell was first studied in depth (Shockley & Queisser, 1961) and the limit describes loss mechanisms is known as the Shockley–Queisser limit. Maximum solar conversion efficiency is placed around 33.7 % assuming a single p-n junction with band gap of 1.4-1.5 eV. Figure 2.10. shows the variation of conversion efficiency as a function of band gap.

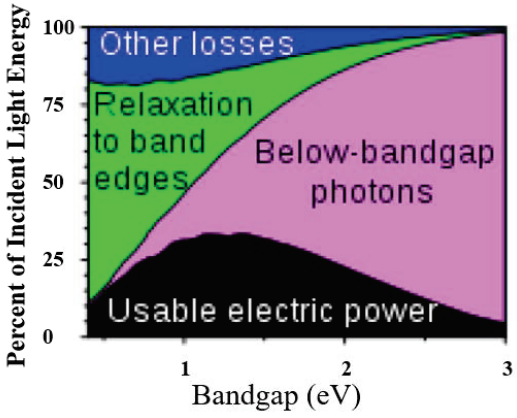

Figure 2.10. Maximum conversion efficiency of a single junction solar cell under one sun illumination.

2.5.1. Optical Losses

Optical losses inhibit the generation of an electron-hole pair for each photon striking the surface of the solar cell and decrease the efficiency of a solar cell by lowering the short circuit current. Reasons of optical loses can be summarized as fallows;

- Reflection of the light from the first layer of a solar cell, reflection at the interfaces between the individual layers of a solar cell.
- Shading active area of the cell by the electrode which reflects the light and does not allow the light to enter the solar cell.
- Transmission of photons with long wavelengths through the absorber

2.5.2. Recombination

Some of the charge carries that are generated in a solar cell are not collected at the electrodes, some of them recombine, i.e. electron and hole recombine and send out a photon. Since those charge carriers are lost for the current, I_{sc} is reduced. This effect also has a great influence on the V_{oc} which is higher for the lower the recombination. Typically, recombination can occur in the bulk, at the interfaces and at the surfaces of the junction. Lattice defects or impurity atoms with energy transition levels within the bandgap of the semiconductor act as recombination centers for the charge carriers.

2.5.3. Thermalization

Only photons with energy higher than the band gap energy of the absorber layer produce electron-hole pairs. The excess energy that the electron-hole pairs receive from the photons is released as heat into the semiconductor lattice. This energy lost is known as thermalization.

In order to decrease thermalization effect, the band gap should be as high as possible. However, a low band gap is desirable to collect as many photons as possible without losing them through the transmission. Therefore, maximum theoretical efficiency of around 30 % can be obtained for the band gap is somewhere around 1,4 - 1,5 eV.

2.5.4. Electrical losses

The maximum power generated by a solar cell is mainly affected by the fill factor (FF). In a practical solar cell, the FF is reduced due to series resistance and shunt resistance. The equivalent circuit of a solar cell with series and shunt resistance can be seen in Figure 2.11.

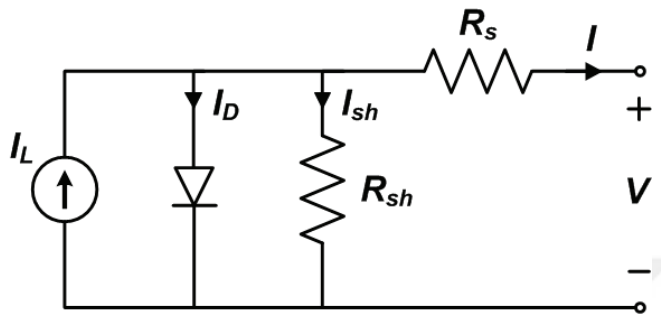

Figure 2.10. The equivalent circuit of a solar cell with series and shunt resistance.

here, I_L is photo current, I_D is the diode current, I is the output current, I_{sh} is the shunt current, R_s series resistance and R_{sh} is the shunt resistance. Output current is given by;

$$I=I_L-I_D-I_{sh} \tag{2.6}$$

Potential across the diode V_D and output voltage V is given by;

$$V_D= I_{sh}\, R_{sh} \tag{2.7}$$

$$V=V_D-IR_s \tag{2.8}$$

Combining above equations with Equation (2.2), output power for non-ideal solar is obtained as;

$$I = I_L - I_0\left[exp\left(\frac{V+IR_s}{kT}\right) - 1\right] - \frac{V+IR_s}{R_{sh}} \tag{2.9}$$

2.5.4.1. Series Resistance

The series resistance is introduced by the sum of resistances of the path of the current through which the photo-generated carriers arrive to the external circuit. It arises from the bulk resistance of the junction, the contact resistance between the junction and electrodes, the resistance of the electrodes. The main effect of the series resistance is to reduce the fill factor, but extremely high values can also reduce the short circuit current. Series resistance should be zero for an ideal solar cell. At open circuit voltage, the series resistance does not affect the solar cell since the overall current flow through the solar cell. On the other hand, near the open-circuit voltage, the IV curve is strongly influenced by the series resistance. A simple and straightforward way to estimate series resistance of a solar cell is to determine the slope of the I-V curve at the open-circuit voltage point. More voltage drops occur in the cell as the series resistance increases and I-V begins to deviate from the low R_s case (Figure 2.11. (a)). For a very high value of R_s, I-V curve becomes straight line with reduced I_{sc}, but V_{oc} remains the same.

2.5.4.2. Shunt Resistance

Shunt resistance results from the leakage of the current through the cell due to local defects in the junction or the shunts at the edges of solar cells (Nelson, 2003). The low shunt resistance provides an alternating current path for the light generated current and causes power losses. As shunt resistance decreases, the amount of current flowing through the solar cell is reduced. This results in the reduction of the voltage from the solar cell. A simple and straightforward way to estimate shunt resistance of a solar cell is to determine the slope of the I-V curve near the short-circuit current point. To prevent lost in V_{oc}, R_{sh} must be as highest as possible contrary to R_s (Figure 2.11. (b)).

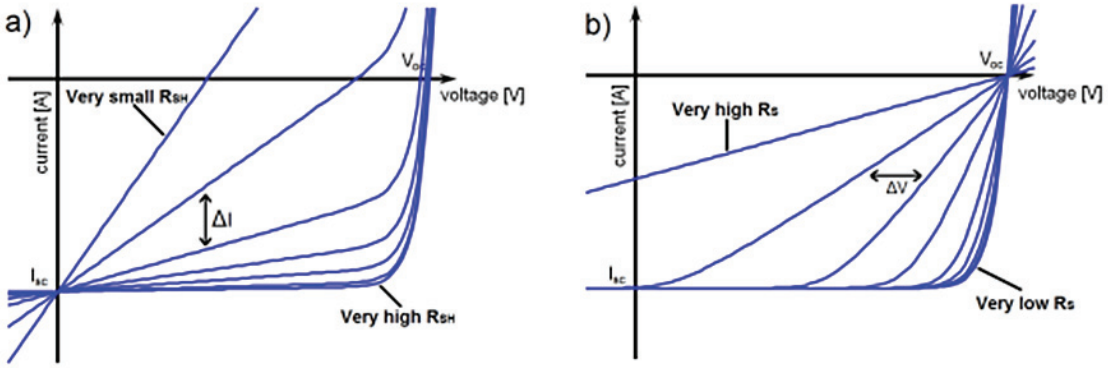

Figure 2.11. Impact of (a) R_{SH} and (b) R_S on the I-V characteristics of a solar cell.

2.5. Thin Film Solar Cells

Despite all the advantages of Photovoltaics (PV), we must not ignore the fact that there are still some issues need to be worked on to increase the efficiency of solar cells and to make solar cells cheaper to shorten the economical payback period. Silicon-based solar cells are the dominant technology in the photovoltaic industry, accounting more than 90 % of total production. In 2014, a record efficiency of 25.6 % (Masuko et al., 2014) was achieved for sc-Si with J_{sc}, V_{oc}, and FF of of 41.8 mA/cm^2, 750 mV, and 82.7 %, respectively. For mc-Si, a record efficiency of 21.25 % in late 2015 was achieved with J_{sc}, V_{oc}, and FF of 39.80 mA/cm^2, 667.8 mV and 80 %, respectively (Green et al., 2016). However, since silicon has an indirect band gap, a few hundred micrometers in thickness of wafers are necessary to absorb sufficient energy from sunlight to have high efficiencies. One approach to eliminate this cost is the replacement of wafers by thin films of semiconductors deposited onto a supporting substrate (Green, 2007). Much less material is consumed in thin film solar cells compared to crystalline silicon solar cells. Since the absorption coefficient of typical thin film absorber materials is about 100 times higher than crystalline silicon, 100 times thinner film material is sufficient to absorb the same amount of energy. While crystal silicon requires 100 cm^3 (100 µm x 1 m x 1 m) material for 1 m^2 solar cells, only 1 cm^3 is required for thin film material. Moreover, there is a loss of more than 50 % of the silicon material when it is sawn from the ingots.

Another advantage of thin film solar cells is that purity and crystal quality requirements on thin film solar cell materials are less stringent than in crystalline silicon solar cells (Li et al., 2012) which also reduce cost. In addition, they can be fabricated on

flexible materials such as metal foils or polyimides which provide completely new applications. Moreover, the installations of silicon cells require heavy glass protection plates that will reduce residential applications (Kessler & Rudmann, 2004). They can be fabricated on flexible materials.

Yet another advantage is that it is possible to adjust the band gap of some thin film materials such as CIGS by varying the composition. By adjusting the band gap, a larger portion of the solar spectrum can be used better and higher efficiencies can be achieved since the theoretical possible efficiencies are strongly dependent on the band gap, as can be seen from Figure 2.12.

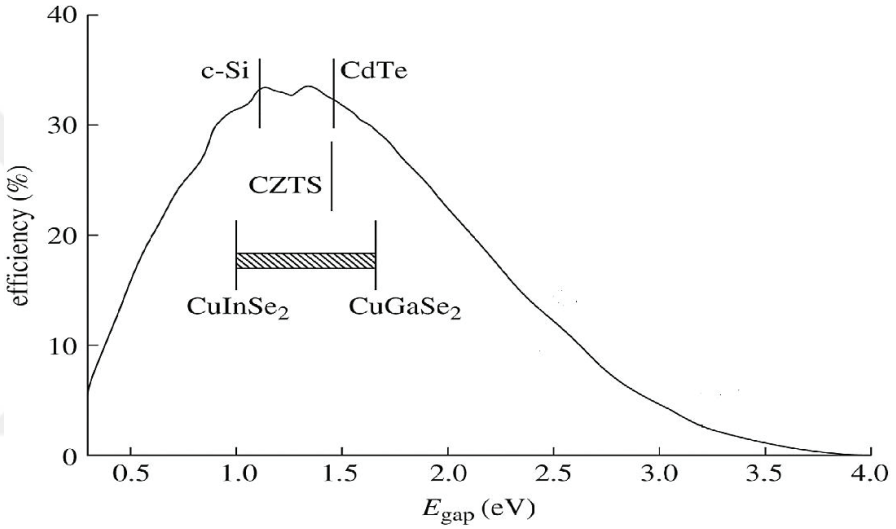

Figure 2.12. Theoretical efficiencies of solar cells for different band gaps.

2.6. Possible Materials

Materials for thin film solar cells should satisfy some important criteria to be usable. Of course, an essential precondition is a large absorption coefficient, since almost all of the existing photons should be absorbed only in a few micrometers. In addition, the band gap should be in the range of roughly 1 - 1,7 eV (see Figure 2.12.) to reach sufficient efficiencies. There is quite a lot of materials that satisfy these conditions. Amorphous silicon (a-Si), is one of the suitable material for the thin film solar cell technology. It exhibits non-crystalline structure whose properties are significantly different from the crystalline silicon. Hydrogen is incorporated to passivate the dangling bonds resulting from the random arrangement of the atoms. The absorption coefficient of a-Si ($\alpha > 10^5$

cm^{-1}) is much higher than that of the crystalline silicon, and the band gap increases from 1.1 eV in crystalline silicon to a direct bandgap of 1.7 eV in the a-Si. Performance of a-Si cells mainly suffer from a phenomenon known as the Staebler-Wronski effect (SWE) when exposed to sunlight (Staebler & Wronski, 1977). For a-Si, the highest efficiency of 10.2 % (Matsui et al., 2013) for a single junction and 13.6 % (Sai et al., 2015) for multijunction were achieved. For organic semiconductors, the light absorption is relatively low because their bandgaps are larger than 2.2 eV. Additional layers are required to trap light for organic solar cell devices.

An approach often followed when it is necessary to find alternative materials is the principle of isoelectronic or cross-substitution (Pamplin, 1960). Following the isoelectronic substitution, atoms of the group IV (Si) are substituted by an equal number of cations and anions of group III and V (like GaAs) or II and VI (like CdTe) respectively to form binary compounds (Lewerenz & Jungblut, 2013). Other compound semiconductors can be formed by substituting one half of the group-II element with a group-I and one half with a group-III element. A common example for such an I–III–VI-compound semiconductor is CIS ($CuInS_2$) or replacing partly the Indium by Gallium forms copper indium gallium selenide ($CuInGaSe_2$). Various further substitutions are also possible, for example replacing the half of element in group-III with an element in group-III and the half with an element in group IV. For CIGS, substitution of In/Ga with Zn and Sn leads to CZTS (Cu_2ZnSnS_4). However, it should be realized that not all substitutional compounds give solar cell materials; only materials that form junctions with other materials and exhibit a photovoltaic effect when exposed to light can be used in thin film solar cell applications.

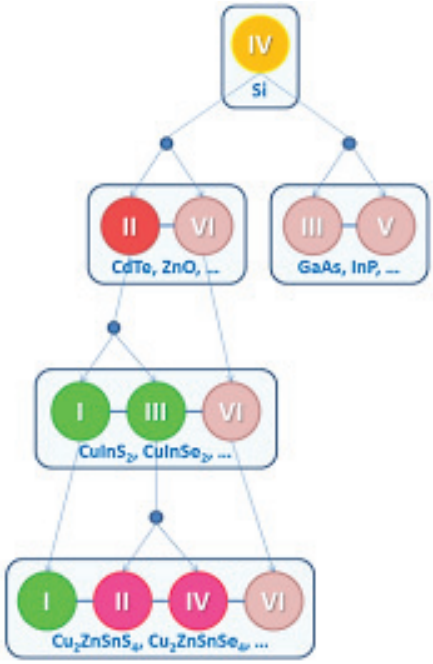

Figure 2.13. Various possible compound semiconductors obtained by gradual substitution of elements from higher and lower groups.

To date, only thin film solar cells based on direct band gap materials such as CIGS and CdTe have reached the status of mass production. CdTe is one of the optimal candidate for thin film solar cells since it is a chemically stable semiconductor with a direct bandgap of about 1.45 eV and large absorption coefficient above 10^4 cm^{-1} (Bai, Yang, & Wang, 2011; Romeo, Bosio, & Romeo, 2010). CdTe devices are fabricated in superstrate structure. Firstly, TCO is deposited on a glass substrate as a front contact, then n-type CdS buffer layer deposited on TCO, followed by an CdTe layer deposited on the CdS at temperatures between 400 °C and 600 °C using close-spaced sublimation (CSS), electrodeposition, sputtering, and screen printing techniques. The efficiency of CdTe based solar cells has reached 22.1 % in 2016. The other successful candidate for thin film solar cell is CIGS chalcopyrite absorber with a record efficiency of 21.7 % (Jackson et al., 2015). Typically, CIGS devices are fabricated in substrate configuration. Firstly, molybdenum (Mo) layer deposited on a glass substrate as a back contact, then CIGS absorber layer deposited on Mo layer, followed by an n-type CdS buffer layer, ZnO layer is deposited on the CdS, finally AZO layer is deposited as a front contact. Unfortunately, both of these technologies have disadvantages. Semiconductor materials usually utilized for their production are either toxic like cadmium or rare in the earth's crust like indium and tellurium. This can be seen in Figure 1.1., which shows both the cost and abundance of these materials in the earth's crust. For long term viability of thin films solar cells,

copper zinc tin sulfide (Cu_2ZnSnS_4; commonly known as CZTS) is an alternative material that is non-toxic and abundant in the earth's crust. CZTS absorber layer will be discussed in fallowing chapter.

CHAPTER 3

Device Structure of CZTS Solar Cell

Despite the differences in the various semiconductor materials, device structures of the many thin film solar cells are similar and CZTS is shown here as an example. CZTS solar cells are multilayer structures and is typically made up of the five thin film layers on glass substrate. The schematic cross section of CZTS solar cell structure is shown in Figure 3.1. Light enters the cell through the Aluminum doped zinc oxide Transparent Conductive Oxide layer (TCO), passes through the ZnO shunt preventing layer and CdS buffer layer, and enters the CZTS absorber layer. The p-n junction is formed between the p-type CZTS absorber layer and the n-type CdS buffer layer.

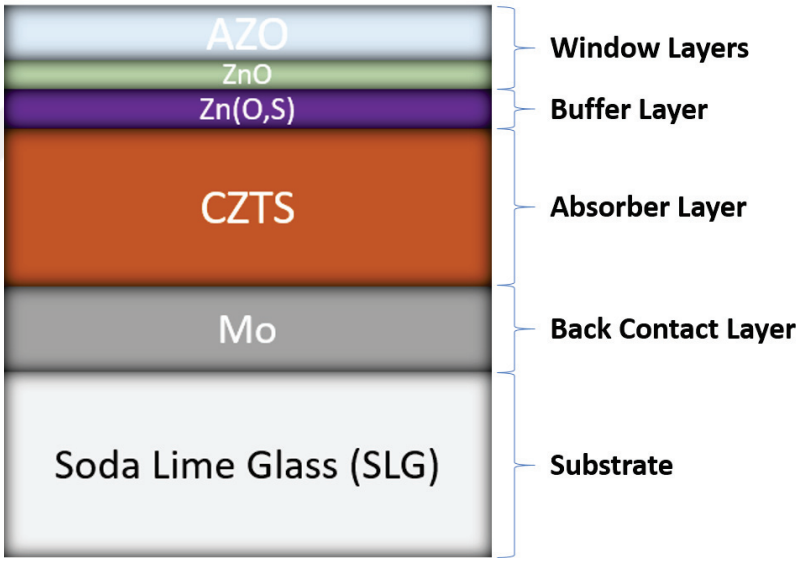

Figure 3.1. Typical structure of solar cell based on CZTS absorber layer.

In the following section, materials used for the fabrication of CZTS solar cell are briefly presented.

3.1. Substrate

Since thin film solar cells are so thin, they have to be deposited on a substrate. For CZTS solar cells, soda-lime glass is the most common substrate and has by now yielded the highest efficiencies (Hiroi et al., 2013; Tajima et al., 2017). One of the advantages of thin films is that they can be deposited on flexible substrates like polymers and metal foils. Polymers can withstand the temperatures up to 450 – 500 °C, while the metal foils can be used at higher temperatures without any deterioration of the substrate. In addition, the need of the metallic conductive back contact layer is eliminated using metallic substrates and the production cost of solar cell modules would be substantially lowered.

3.2. Back Contact

On the substrate, metallic conductive back contact is needed. The requirements for a good the back contact is low resistance, good work function and stability against corrosion, oxidation etc. For good performance and long-term stability of CZTS solar cells, a certain inertness of the back contact (BC) layer is essential for reproducible CZTS absorber growth in an extremely corrosive process atmosphere. Moreover, to minimize optical losses, a high optical reflectance is necessary.

Many metals and semi-metals with these properties can be selected as the back contact, but the formation of a good electrical contact to CZTS is still challenging due to Schottky barrier formation at the CZTS/BC interface. An ohmic metal/semiconductor contact is formed when the BC for the CZTS satisfies the fallowing condition, otherwise Schottky barrier is formed

$$\Phi_m > E_g + x \tag{3.1}$$

where E_g and x are the band gap and electron affinity for a p-type semiconductor, and Φ_m is the work function of a metal.

As a conducting back contact, a thin layer of Molybdenum (Mo) is generally used for CZTS solar cells, it complies well with most requirements. The preferred contact resistivity of Mo is $\leq 0.3\ \Omega$.cm (Singh & Patra, 2010). It is already known that MoS_2 which inevitably forms between Mo and CZTS during sulfurization. The formation of a

Schottky barrier at CZTS/MoS_2 interfacial layer could lead to electrical problems and adhesion problems (Wang et al., 2010). Reaction of Mo with S can occur through decomposition reactions at CZTS-back contact and/or during the CZTS sulfurization process which supply S (Scragg, Dale, Colombara, & Peter, 2012; Scragg, Watjen, et al., 2012). CZTS-back contact decomposition reactions were explained by Scragg et al., 2012 at an instable kesterite/Mo interface;

$$2Cu_2ZnSnS(e)_4 + Mo \rightarrow 2Cu_2S(e) + 2ZnS(e) + 2SnS(e) + MoS(e)_2$$

Formation of secondary phases (SnS, Cu_2S, ZnS) due to decomposition at kesterite/Mo interface could enhance recombination. High S partial pressure should be ensured during sulfurization to prevent the CZTS surface decomposition reaction involving SnS evaporation (Redinger, Berg, Dale, & Siebentritt, 2011) and to prevent CZTS/back contact decomposition reaction to provide MoS_2 formation without CZTS decomposition (Scragg et al., 2013).

3.3. CZTS Thin Films

CZTS is a p-type semiconductor with talented physical properties, such as the direct band gap of 1.5 eV, high optical absorption coefficient ($>10^{-4}$ cm^{-1}), low thermal conductivity etc. (Katagiri et al., 2001). It is derived from the CIGS structure by the isoelectronic substitution of the indium (In) and gallium (Ga) with zinc (Zn) and tin (Sn). Since this material is non-toxic and its component elements are abundant in the earth's crust, CZTS solar cells are free from both resource-saving concerns and environmental pollution. In addition, grain boundaries in CZTS thin films are suitable for increasing the minority carrier collection (Li et al., 2012). Theoretical calculations have shown that a high conversion efficiency of 32.2 % (Shockley & Queisser, 1961) for CZTS thin film solar cells with a few micrometer CZTS layer is possible. For existing PV technologies, minimum cost of raw materials was calculated by Wadia et al., 2009 (Wadia et al., 2009). For CZTS PV technology, the cost of raw materials is much lower than other existing thin film PV technologies. Due to these important features, CZTS is expected to be one of the promising materials for thin film solar cells.

It is expected that CZTS phase forms from intermediate binary metal sulfides and ternary Cu-Sn sulfides such as CuS, Cu_2S, ZnS, SnS, SnS_2, and Cu_2SnS_3 (Hergert & Hock, 2007; Schorr, Weber, Honkimäki, & Schock, 2009).

Hergert, et al. 2007 proposed the formation of kesterite CZTS phase by fallowing two-step reaction pathway (Hergert & Hock, 2007);

$$Cu_{2-x}S + SnS_2 \rightarrow Cu_2SnS_3$$

$$Cu_2SnS_3 + ZnS \rightarrow Cu_2ZnSnS_4$$

Schorr, et al. 2009 described the reaction of three different mixtures of binary and ternary sulfide compounds at 700 °C to form kesterite CZTS (Schorr et al., 2009);

$$2CuS + SnS + ZnS \rightarrow Cu_2ZnSnS_4$$

$$Cu_2S + SnS_2 + ZnS \rightarrow Cu_2ZnSnS_4$$

$$Cu_2SnS_3 + ZnS \rightarrow Cu_2ZnSnS_4$$

It is reported that CZTS phase starts to form below 300 °C with CuS, SnS, and ZnS phases in addition to CZTS. At a temperature range of 350 °C–450 °C, ZnS and Cu_2SnS_3 phases are present in addition to CZTS.

3.3.1. Crystal Structure of CZTS

CZTS compound may exist in two main crystal structures, known as stannite type and kesterite type (Hall, Szymanski, & Stewart, 1978). These two crystal structures are very similar; both are tetragonal structures, consisting of cubic closed packed array of sulfur anions, with cations that occupy one half of the tetrahedral voids, and are formed with a stack similar to the zinc blend. The structural differences are related to the different arrangements of Cu and Zn atoms along the c-axis (Figure 3.2.).

The cationic layers along the c-axis are arranged in Cu-Sn, Cu-Zn, Cu-Sn and Cu-Zn fashion in kesterite structure. One Cu atom is in position 2a with Madelung potential

of -15.04 V while Zn atom and the other Cu atom are in positions 2d and 2c with the corresponding Madelung potentials of -21.88 and -15.21 V, respectively. In the stannite structure, a periodic arrangement of the Zn-Sn cationic layer between the Cu-Cu layers is repeated with both Cu atoms at the 4d position and the Zn atom at 2a position with the corresponding Madelung potentials of -15.30 and -21.62 V, respectively. Sn atom site is in position 2b in both structures (Catlow et al., 2010; Persson, 2010). Theoretical studies have predicted that CZTS usually appears in kesterite phase because it is thermodynamically more stable as compared to stannite phase (Maeda, Nakamura, & Wada, 2009; Schorr, 2007). Most of CZTS samples have been reported to have kesterite structure as predicted theoretically.

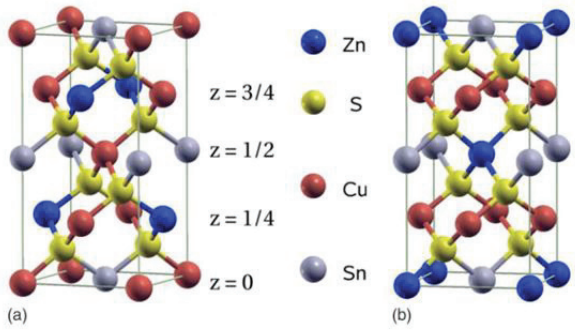

Figure 3.2. Schematic representations of the (a) kesterite and (b) stannite crystalline structure of CZTS.
(Source: Paier, Asahi, Nagoya, & Kresse, 2009)

According to Paier et al., 2009, the lattice constants for kesterite CZTS structure are a=0.546 nm and c=1.093 nm (Paier et al., 2009), but slightly different values can be found in other works (Persson, 2010; Schorr, 2011).

3.3.2. Electrical Properties of CZTS

For a series of intrinsic point defects and defect complexes in CZTS, first principle theoretical calculations of formation energy and transition energy levels show that Cu_{Zn} antisite defects, which has a lower formation energy and relatively deeper acceptor level compared to the Cu vacancy, causes p-type conductivity (Chen, Yang, Gong, Walsh, & Wei, 2010). Due to the low formation energy of acceptor defects, n-type doping in CZTS is difficult.

Most resistivity values reported for CZTS thin films range from ~ 10^{-3} Ω.cm to 10^{1} Ω.cm (Kumar, Bhaskar, Babu, & Raja, 2010; Moriya, Tanaka, & Uchiki, 2008; Nakayama & Ito, 1996; Tanaka et al., 2005; Zhang, Lexi, Yujun, & Erqing, 2006; Zhang & Shao, 2009). Resistivity values as high as 200 Ω.cm were reported by (Nakayama & Ito, 1996), for CZTS samples which are prepared upon heat treatment in H_2S of spray-deposited quaternary polycrystalline precursors. For increasing copper content, a rapid decrease in resistivity (down to 10^{-2} Ω.cm) was observed by the same authors and a similar behavior was also reported for the CZTSe samples prepared by co-evaporation. For Cu-rich samples, conductive copper sulfide phases are usually observed and proposed to be responsible for the low sample resistivity (Nakayama & Ito, 1996; Tanaka et al., 2005). On the other hand, the high conductivity of Cu-rich CZTS thin films may also be due to higher Cu_{Zn} defect concentration compared to the stoichiometric film.

Depending on the film composition and growth technique, there are many conductivity and mobility values in the literature (Nakayama & Ito, 1996; Tanaka et al., 2005; Zhang & Shao, 2009). Free carrier mobility is heavily influenced by the scattering mechanisms and therefore different results are acquired relying upon the material qualities such as defect density and spurious phases. Results of Hall effect measurement showed that hole mobility of CZTS varies from 0,1 to 30 $cm^2/(V.s)$, with most of the published values being in the range of 1-10 $cm^2/(V.s)$ (Chan, Lam, & Surya, 2010; Ito & Nakazawa, 1988; Liu, Li, et al., 2010; Rajeshmon et al., 2011; Xinkun, Wei, Shuying, Yunfeng, & Hongjie, 2012). The highest reported mobility for CZTS with a resistivity of 5.4 Ω.cm (Liu, Zhang, et al., 2010) obtained for a film grown by reactive co-sputtering deposition of metallic precursors in H_2S atmosphere. Table 3.1. shows some reported resistivity, mobility and hole density values obtained from Hall effect measurements.

Table 3.1.Reported resistivity, mobility and carrier density values for CZTS.

ρ (Ω.cm)	μ ($cm_2/(V.s)$)	p (cm^{-3})	Reference
0.15	6.3	8.2 10^{18}	(Zhang & Shao, 2009)
0.13	6	8.0 10^{18}	(Tanaka, Shimakawa, Miyata, Sato, & Minami, 2005)
~ 0.13	12.6	3.8 10^{18}	(Zhou, Wang, Xu, & Zhang, 2010)
0.36	11.6	4.5 10^{17}	(Zhou et al., 2010)
5.4	30	3.9 10^{16}	(Zhang, et al., 2010)

Capacitance-Voltage (C-V) measurements (Katagiri, 2005; Scragg, Dale, Peter, Zoppi, & Forbes, 2008) were also performed on the final devices to obtain the hole concentration. Hole concentration was found to be 10^{16}-10^{17} cm^{-3} for good performance devices, while materials with higher hole concentration (about 10^{18} cm^{-3}) gave the low performance devices (Katagiri, 2005). According to the analysis of QE curves of these solar cells, the minority carrier diffusion length increases with decreasing acceptor concentration.

These outcomes demonstrate that good quality CZTS thin films need to have adequately high resistivity, probably associating with low defect concentration. To obtain working devices, the lower limit for resistivity seems to be 10 Ω.cm, which corresponds to a free carrier concentration of about 10^{17} cm^{-3} using a mobility of 5 $cm^2/(V.s)$.

3.3.3. Optical Properties of CZTS

The band gap of stoichiometric kesterite CZTS was theoretically calculated as 1.5 eV by Chen et al., 2009 (Chen, Gong, Walsh, & Wei, 2009). The reported band gap for CZTS prepared with various deposition techniques changes between 1.4 eV and 1.55 eV (Ito & Nakazawa, 1988; Moriya, Watabe, Tanaka, & Uchiki, 2006; Prabhakar & Nagaraju, 2010; Sekiguchi, Tanaka, Moriya, & Uchiki, 2006; Seol, Lee, Lee, Nam, & Kim, 2003). However, due to the deviation in stoichiometry, very low band gap of 1.20 eV was also reported (Tanaka, Moritake, Oonuki, & Uchiki, 2008). Variation in the bandgap of CZTS was observed by changing the material composition or using different sulfurization conditions (Babu, Kumar, Bhaskar, & Vanjari, 2010; Katagiri, 2005; Moriya, Tanaka, & Uchiki, 2007).

The absorption coefficient of CZTS thin films was found to be larger than 10^4 cm^{-1} (Cui, Zuo, Jiang, Yuan, & Chu, 2011; Fernandes, Salomé, & Da Cunha, 2011). High frequency dielectric constant of CZTS was theoretically determined as 6.8 using three different approaches by Zhao et al., 2011 (Zhao & Persson, 2011). For CZTS thin film deposited by RF magnetron sputtering and annealed at 400 °C, a refractive index value of 2.07 was reported by Seol et al., 2003 (Seol et al., 2003).

3.3.4. The Role of Intrinsic Defects in CZTS

Several intrinsic point defects are possible for CZTS quaternary compound, including antisite defects (Cu_{Zn}, Zn_{Cu}, Cu_{Sn}, Sn_{Cu}, Zn_{Sn}, and Sn_{Zn}), vacancies (V_{Cu}, V_{Zn}, V_{Sn}, and V_S) and interstitial defects (Cu_i, Zn_i, and Sn_i). These defects can manifest as shallow or deep levels within the band gap, can serve as donor or acceptor, can act as traps or recombination centers, thus the opto-electronic properties of the host material are affected. CZTS shows p-type conductivity due to the presence of intrinsic acceptor defects with low formation energy. Defect formation in CZTS compounds have been studied theoretically since 2010 (Chen, Gong, Walsh, & Wei, 2010; Chen, Yang, et al., 2010; Maeda, Nakamura, & Wada, 2011; Nagoya, Asahi, Wahl, & Kresse, 2010). Chen et al., 2010 predicted the values of the intrinsic defect ionization levels within the band gap of CZTS (Chen, Yang, et al., 2010). These values are summarized in Figure 3.3. (Walsh, Chen, Wei, & Gong, 2012). As indicated by these works, copper vacancy causes a shallow acceptor level at 0.02 eV above the valence band, while Cu_{Zn} antisite results in a higher energy level of 0.12 eV. ab-initio calculations (Chen, Gong, et al., 2010; Nagoya et al., 2010) show that the intrinsic dominant defect in CZTS is Cu_{Zn} antisite and shows the lowest formation energy. While a negative value of Cu_{Zn} formation energy is reported in (Nagoya et al., 2010), the calculations reported in (Chen, Yang, et al., 2010) predict that it will be negative if the Fermi level is higher than 0.12 eV. A self-compensation mechanism revealed by both works prevents the possibility of a n-type doping for CZTS.

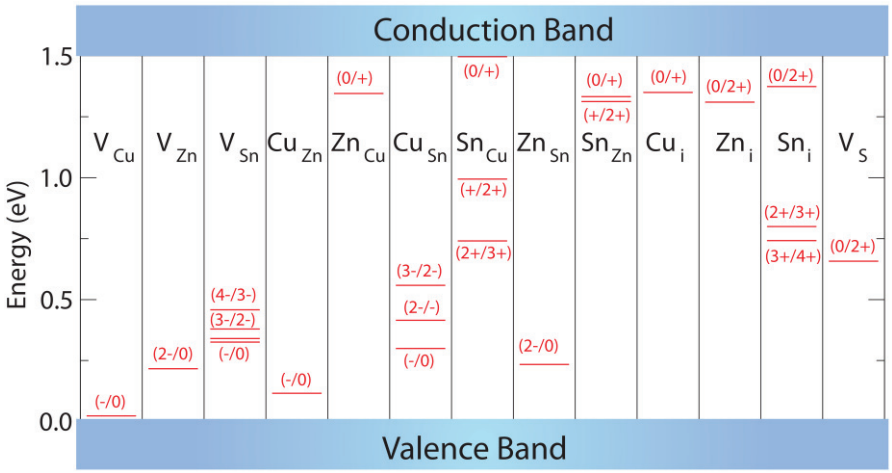

Figure 3.3. The ionization energy levels of intrinsic defects within the bandgap of CZTS. (Source: Walsh et al., 2012)

In addition to the Cu_{Zn} antisites, four other dominant defects are estimated, indicating a relatively low formation energy for the Cu-poor CZTS composition that is typically used in PV applications. In the order of increasing formation energy, these defects are V_{Cu}, Zn_{Sn}, V_{Zn} and Cu_{Sn}.

Intrinsic defects in absorber layers play an important role in view of solar cell performances. As deep levels introduce traps or recombination centers for photo generated electron-hole pairs, they are detrimental for photovoltaic performances. According to first principle calculations reported by Chen et al., 2010 (Chen, Gong, et al., 2010), the Cu_{Sn} antisite is a deep level acceptor defect, with energy close to the mid-gap and with low formation energy. For this reason, it is expected that this defect is the most active recombination center in CZTS (Chen, Gong, et al., 2010; Repins et al., 2011). It was predicted that the Sn_{Zn} antisite is one of the major deep electron traps in the bandgap of CZTS (Han et al., 2013). On the other hand, by the same calculations, it was demonstrated that that charge-compensated defect complexes like (Cu_{Sn} + Sn_{Cu}) are likely to form and passivate deep levels in CZTS (Chen, Gong, et al., 2010). (Cu_{Zn} + Sn_{Zn}) defect cluster is regarded as a detrimental defect for photovoltaic performances since it has a relatively low formation energy and produce a deep donor level (Chen, Wang, Walsh, Gong, & Wei, 2012). According to these works, Cu-poor and Zinc-rich composition may be desirable to suppress the formation of these harmful defects. This may also explain why the best CZTS solar cells have been produced with this kind of composition. In addition to the defect complexes mentioned earlier, numerous possibilities have been also predicted. Among them, (V_{Cu}^{-} + Zn_{Cu}^{+}), (Zn_{Sn}^{2-} + $2Zn_{Cu}^{+}$) and ($2Cu_{Zn}$ + Sn_{Zn}) (Chen et al., 2012) are the ones with the lowest formation energy for Cu-poor composition.

More recently, Rios et al., 2016 focused on the investigation of CZTS/Se according to four off-stoichiometry types; A-type is Cu-poor/Zn-rich which leads to formation of V_{Cu} and Zn_{Cu}, B-type is Cu-poor/Zn-rich which leads to formation of Zn_{Cu} and Zn_{Sn}, C-type is Cu-rich/Zn-poor which leads to formation of Cu_{Zn} and Sn_{Zn}, and D-type is Cu-rich/Zn-poor which leads to formation of Cu_{Zn} and Cu_i (Rios, Neldner, Gurieva, & Schorr, 2016). These cation substitutions are shown in Figure 3.4. and listed in Table 3.2. They prove that CZTS structure can self-adapt to Cu-poor and Cu-rich compositions without any structural change.

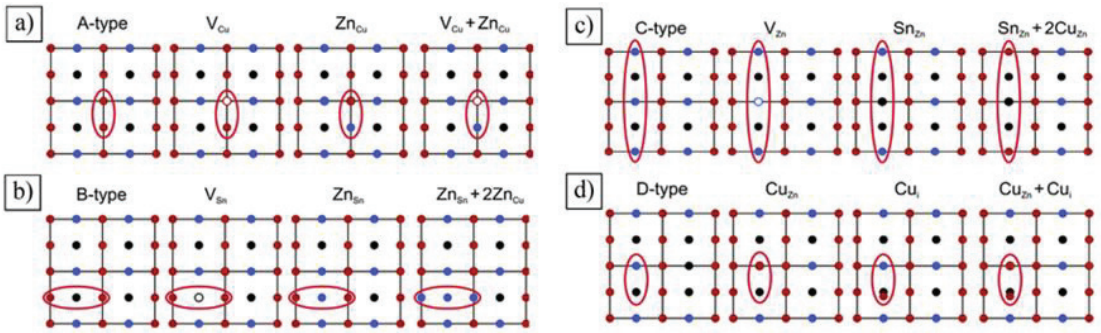

Figure 3.4. Cation substitution results from non-stoichiometric CZTS in A-, B-, C- and D-type. Copper, zinc and tin are represented in red, blue and black, respectively.
(Source: Rios et al., 2016)

Table 3.2. The classification of cation substitution types with related non-stoichiometry types and cation substitution reactions.
(Source: Rios et al., 2016)

Type	Composition	Cation substitution reaction	Intrinsic point defects
A	Cu-poor/Zn-rich/Sn-const.	$2Cu^{+} \rightarrow Zn^{2+}$	$V_{Cu} + Zn^{2+}{}_{Cu}$
B	Cu-poor/Zn-rich/Sn-const.	$2Cu^{+} + Sn^{4+} \rightarrow 3Zn^{2+}$	$2Zn^{2+}{}_{Cu} + Zn^{2+}{}_{Sn}$
C	Cu-rich/Zn-poor/Sn-rich	$3Zn^{2+} \rightarrow 2Cu^{+}+Sn^{4+}$	$2Cu^{+}{}_{Zn} + Sn^{4+}{}_{Zn}$
D	Cu-rich/Zn-poor/Sn- const.	$Zn^{2+} \rightarrow 2Cu^{+}$	$Cu^{+}{}_{Zn} + Cu^{+}{}_{i}$

3.3.5. CZTS Phase Stability and Secondary Phases

Control of phase stability is very important to develop high quality CZTS absorber layers. However, high purity CZTS synthesis is challenging, as other ternary and quaternary compounds can be easily generated in the synthesis process. The representation of the Cu-Zn-Sn-S quaternary system is quite complicated because four kinds of atoms would require a four-dimensional phase diagram and the temperature also introduces an additional variable.

Cu_2S–ZnS–SnS_2 quasi-ternary system developed at 400 °C in equilibrium for Cu_2ZnSnS_4 was investigated by Olekseyuk et al., 2004 (Olekseyuk, Dudchak, & Piskach, 2004). Assuming a perfect balance between metal and sulfur, Scragg et al. 2010 suggested a simplified a pseudo-ternary phase diagram (Figure 3.5.) based on the study of Olekseyuk et al., 2004 (Scragg, 2010). That is, it is assumed that the amount of sulfur contained in the material depends only on the amount and valence of the metals: Cu(I), Zn(II) and Sn(IV). Both works showed that Cu_2ZnSnS_4 single phase can be formed in a

very narrow stability region at the center of the diagram. Additional secondary phases can easily be formed in the synthesis process by the stoichiometry variations out of this region. Different secondary phases are expected in the respective regions of the phase diagram depending on the system composition.

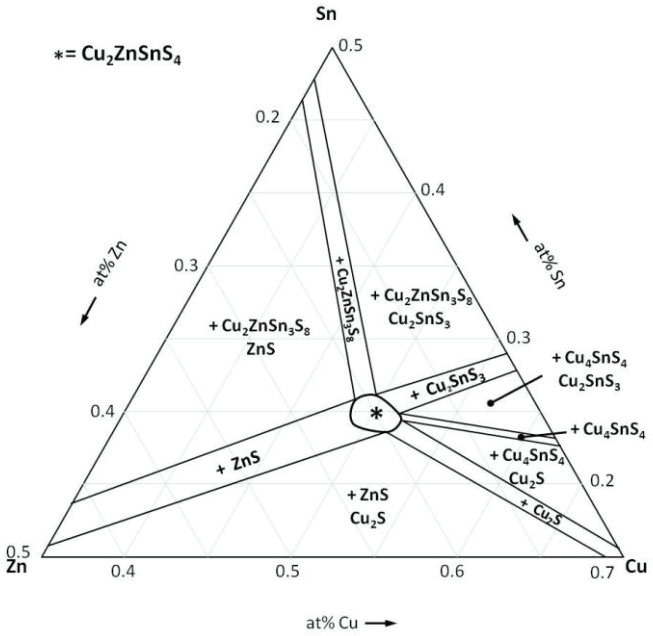

Figure 3.5. Ternary phase diagram for the Cu-Zn-Sn system at 400 °C.
(Source: Scragg, 2010)

A list of possible secondary phases detected either during CZTS formation (Schurr et al., 2009; Weber, Mainz, Unold, Schorr, & Schock, 2009) or in the final CZTS films (Fernandes et al., 2011; Wang et al., 2011) can be seen in Table 3.3. (Jost, 2008; Weber, 2009).

Table 3.3. Secondary phases detected for the Cu-Zn-Sn-S system.

Compound	Band gap (eV)	Electric Properties
Cu_2ZnSnS_4	1.5	p-type semiconductor
Cu_2SnS_3	1.0	p-type semiconductor
ZnS	3.6	Insulator
SnS_2	2.5	n-type semiconductor
SnS	1.0 indirect, 1.3 direct	p-type semiconductor
Cu_2S	1.2	p-type semiconductor, metal like, highly defective
CuS	1.2 indirect, 2.3 direct	

3.3.6. Effect of Secondary Phases on CZTS Absorber Layer and Solar Cells

Binary and ternary secondary phases such as CuS, Cu_2S, Cu_2SnS_3, ZnS, SnS, and SnS_2 can easily form during the growth process of CZTS since single phase CZTS can be formed in a very narrow stability region in phase diagram. Control of secondary phase formation in CZTS is a main point for achieving high efficiency devices.

Cu-S and Cu-Sn-S compounds are detrimental for the device performance of CZTS solar cells since they act as metals (Nozaki, Shibata, & Ohhashi, 1991; Wagner & Wiemhöfer, 1983; Wu et al., 2007). These secondary phases can form shunting paths in the devices, implying that front and back contact are connected inside of the cell so that the current cannot be utilized for an external load. Since conducting phases in a solar cell increase recombination, they can present a serious problem. Cu_2SnS_3 (CTS), which is a p-type semiconductor with metallic character (Wu et al., 2007), can reduce the E_g and increase the conductivity of the device by forming a solid solution with CZTS.

Copper sulfides ($Cu_{(2)}S$) can be expected for the Cu-rich as well as for the Sn- and Zn-poor compositions. They are p-type with good metallic conductivity due to a high concentration of holes in the valence band. The impact of the Cu-rich composition on CZTS is still controversial. An improvement in crystallinity has been reported with increasing copper content in co-evaporated CZTS films (Tanaka et al., 2010). However, opposing trends were observed for CZTS samples grown by sol-gel and electrochemical deposition (Ennaoui et al., 2009; Schurr et al., 2009; Tanaka, Fukui, Moritake, & Uchiki, 2011). Jimbo et al., 2007 observed the improvement of CZTS morphology by decreasing copper content for the films fabricated from co-sputtered precursors (Jimbo et al., 2007). Copper sulfides that segregate on the surface of CZTS can be removed by chemical treatment of KCN, but undesirable voids may occur after chemical treatment (Fernandes, Salomé, & Da Cunha, 2009; Yoo & Kim, 2011). In this manner, copper-poor and zinc-rich compositions are desirable for suppressing Cu-S phase formation, and are generally accepted in the literature for the realization of high efficiency CZTS devices (Katagiri et al., 2008; Wang et al., 2010). The copper-poor and zinc-rich compositions of CZTS films with $Cu/(Zn+Sn) \approx 0.8$ and $Zn/Sn \approx 1.2$ is suggested as the most suitable composition for high-performance solar cells both theoretically (Chen, Walsh, Gong, & Wei, 2013) and experimentally (Shin et al., 2013; Todorov et al., 2013; Wang et al., 2014).

For the Cu-poor and Zn-rich compositions, ZnS phases are expected in the CZTS films. It is not clear how this phase affects the device performances. Due to the high band gap of this material (3.6 eV), the presence of ZnS can give insulator regions in the CZTS. It doesn't influence the V_{oc}, but can cause an increase in the series resistance because of its low conductivity. ZnS segregations can both reduce the active area and inhibit the current conduction in the absorber, reduces the device performance. However, ZnS phases are frequently detected even in the best solar cells (Kato, Hiroi, Sakai, Muraoka, & Sugimoto, 2012; Kejia Wang et al., 2011), so their role in the device performances does not seem harmful.

Tin sulfide phases can also result from Cu-poor and Sn-rich composition. The SnS compound shows both p- and n-type conduction (Thangaraju & Kaliannan, 2000) with a bandgap of 1.2-1.7 eV (Avellaneda, Nair, & Nair, 2009; Ogah, Zoppi, Forbes, & Miles, 2009).Tin disulfide (SnS_2), which is a n-type semiconductor with a direct bandgap of 2.18–2.44 eV (Deshpande, Sagade, Gudage, Lokhande, & Sharma, 2007; Hu et al., 2013; Shibata, Muranushi, Miura, & Kishi, 1990; Thangaraju & Kaliannan, 2000), No harmful effects of Sn-S phases on the device performances have been reported. However, these secondary phases can act as an insulator, if it is present in larger quantities it is also possible to form a second diode with a polarity opposite to CZTS, which prevents the carrier collection and reduces the fill factor. Moreover, tin sulfides evaporate from CZTS films during sulfurization due to their high vapor pressure, which causes tin losses and can be harmful to both stoichiometry control and CZTS phase stability (Scragg, Ericson, Kubart, Edoff, & Platzer-Björkman, 2011).

Fig. 3. 6 illustrates a representation of the presence of secondary phases in four different locations in a thin film device. Detrimental effects on the device performance depends on where the secondary phase segregates. If the phase is conductive and located between the columnar grains of the absorber material, it causes shunting (situation (a)). If the phase is insulating and located at the back contact, the case for MoS_2, cause high series resistance in the device (situation (b)). If the phase such as ZnS is located between the absorber and the buffer layer, due to formation of barriers for the charge carriers V_{oc} and I_{sc} decreases (situation (c)). If the phase is located in the bulk of the absorber layer may act as recombination center and cause to a decrease of the V_{oc} and I_{sc} (situation (d)).

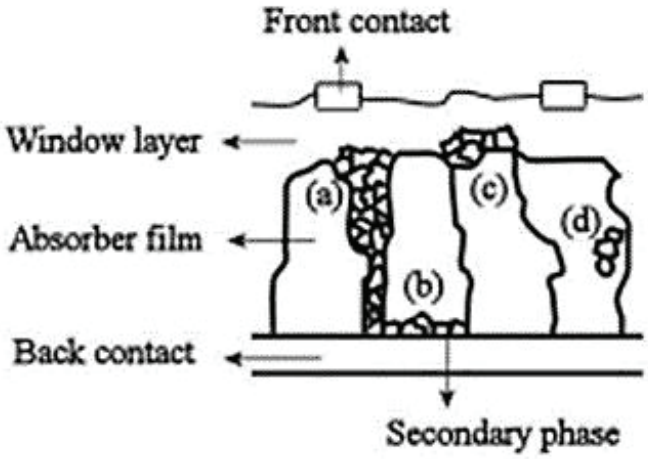

Figure 3.6. Schematic illustration of possible secondary phase segregations.

Figure 3.7 shows possible band alignments at heterointerfaces between CZTS and secondary phases proposed by Bao, 2014 (Bao, 2014). According to Type 1 band alignment, as shown in Figure 3.7. (a) and (b), depending on whether the band gap of the secondary phase is higher or lower than that of CZTS, position of CBM and VBM of the secondary phase changes with respect to CZTS. If the energy gap of the secondary phase is lower than that of CZTS (Figure 3.7. (a)), secondary phase serves as a sink for both the minority and majority carriers, and make the carrier recombination easier. Therefore, the cell efficiency would be reduced. If the energy gap of the secondary phase is larger than that of CZTS (Figure 3.7. (b)), band offset may be a barrier for both minority and majority carriers. According to Type 2 band alignment, as shown in Figure 3.7. (c) and (d), position of CBM and VBM of the secondary phase with respect to CZTS don't depend on the band gap of the secondary phase, both of CBM and VBM for the secondary phase are lower or higher than those of CZTS. For Type 2 band alignments, secondary phase serves as a sink for only one type of carrier, and make the carrier recombination harder.

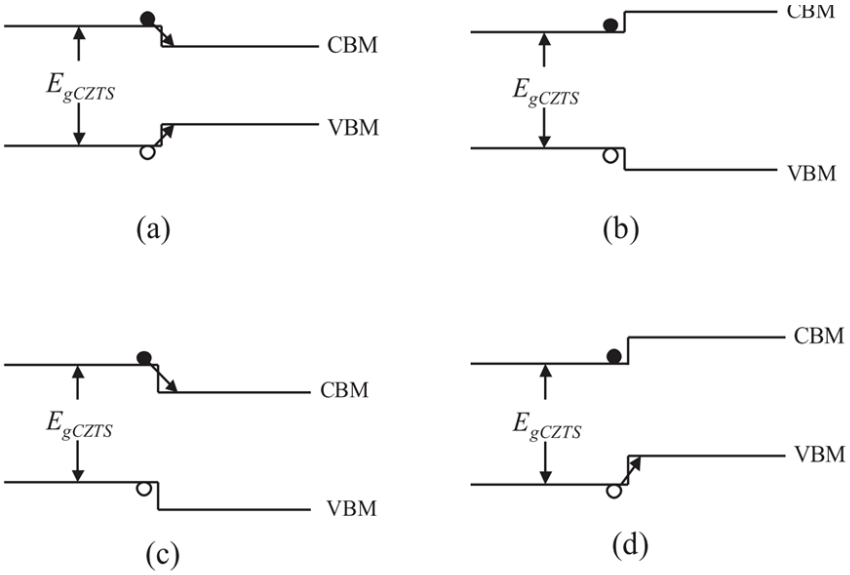

Figure 3.7. Possible band alignments at heterointerfaces between CZTS and secondary phases (a) type I heterointerface with E_g(s.p.)<E_g(CZTS), (b): type I heterointerface with E_g (s.p.)>E_g(CZTS) (c): type II heterointerface with CBM(s.p.)<CBM(CZTS) and VBM(s.p.)<VBM(CZTS) (d): type II heterointerface with CBM(s.p.)>CBM(CZTS) and VBM(s.p.)>VBM(CZTS)

3.3.7. Detecting Secondary Phases in CZTS

In order to characterize CZTS thin films, X-ray diffraction (XRD) and Raman Spectroscopy are generally used as supplementary techniques. Since $Cu_{2-x}S$ spurious phases and Sn_xS_y compounds (SnS, SnS_2 and Sn_2S_3) show diffraction peaks clearly distinct from those of CZTS, they can be easily identified by XRD. However, as it can be seen from Figure 3.8. (Walsh et al., 2012), it is quite difficult to distinguish ZnS and Cu_xSnS_{x-1} (CTS) phases from CZTS phase. Indeed, ZnS diffraction pattern overlaps with the CZTS one as the most probable ZnS cubic phase exhibits a crystal structure very similar to CZTS. similar to ZnS, the diffraction peaks of both cubic and tetragonal Cu_2SnS_3 overlaps with the CZTS phase (Fernandes et al., 2011) due to similar symmetry and lattice constant with CZTS. Among CTS compounds, only the orthorhombic Cu_3SnS_4 phase show diffraction peaks distinct from CZTS and can be detected by XRD.

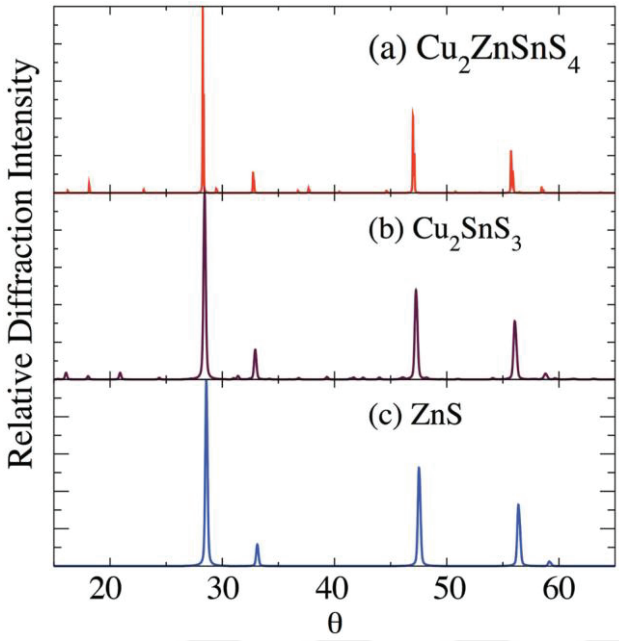

Figure 3.8. Overlapping of CZTS, Cu_2SnS_3 and ZnS XRD peaks.
(Source: Walsh et al., 2012)

Alternatively, Raman spectroscopy is used to distinguish secondary phases present in the CZTS thin films. It should be noted that only the surface region of the samples can be examined by Raman spectroscopy since the light penetration depth is in the order of hundred nanometers or less (the penetration depth can be roughly estimated as $1/(2\alpha)$, where α is the sample absorption coefficient) with the typical laser excitation sources (300-650 nm) used in Raman spectroscopy. In order to perform in-depth analysis, sample cross-section can be used. Figure 3.9. shows a clear Raman spectrum of a Cu_2ZnSnS_4 mono-grain powder with characteristic peaks (Altosaar et al., 2008). The list of Raman peaks of some secondary phases is also given in the Table 3.4.

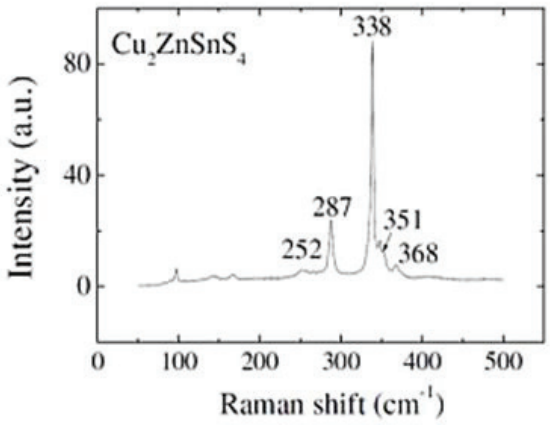

Figure 3.9. Typical Raman spectrum of a Cu_2ZnSnS_4 mono-grain powder.
(Source: Altosaar et al., 2008)

Table 3.4. Raman peaks of CZTS, ternary and binary phases.
(Source: Fernandes et al., 2011)

Phase	Raman Scattering Peak (cm^{-1})
CZTS	289, 339, 350, 370
Tetragonal-CTS-Cu_2SnS_3	297, 337, 352
Cubic-CTS-Cu_2SnS_3	267, 303, 356
Orthorombic-CTS-Cu_3SnS_4	318
Cubic-ZnS	275, 352
SnS	160, 190, 219
SnS_2	314, 215
Sn_2S_3	32, 60, 307
$Cu_{2-x}S$	264, 475
MoS_2	288, 384, 410

From these data, it can be seen that the main vibrational peaks of ZnS and tetragonal Cu_2SnS_3 are very close to the CZTS characteristic peaks. It may be difficult to clearly identify these phases using laser excitation in the red energy region, especially when only traces of ZnS and CTS coexist with CZTS. Quite recent works showed that it is possible to clearly identify ZnS (even when present only in small quantities) using Raman spectroscopy with UV resonant excitation conditions at 325 nm (Fairbrother et al., 2012).

There are also some other experimental techniques that can be useful to detect spurious phases in CZTS thin films. Wang et al., 2011 have reported EDX scans in STEM mode and identified secondary phases existing as segregated clusters both in the bulk and at the grain boundaries (Wang et al., 2011). Chemical depth profiles, using various techniques such as EDX, XPS, GDOES and SIMS, can also be useful to detect spurious phases. For example, ZnS segregations on the bottom of CZTS thin films can be clearly revealed by measuring the Zn-depth profile (Kato et al., 2012; Shin et al., 2013). Optical measurements can also be used to assess the presence of possible spurious phases, for example, sample transmittance is expected to be reduced due to presence of conductive copper sulphide phases. In fact, these phases exhibit a high absorption coefficient in the infrared region because of high defect and free carrier density. A contribution in the infrared region is also expected if the sample includes spurious phases with E_g lower than the CZTS bandgap such as SnS, Sn_2S_3, and Cu_2SnS_3.

3.3.8. Fabrication Techniques of CZTS Thin Film

In order to develop a suitable absorber preparation technique to have low cost and high efficiency CZTS thin film solar cells, several physical and chemical deposition methods have been investigated. The techniques employed to fabricate CZTS thin film can be broadly classified as vacuum-based and non-vacuum deposition methods. The vacuum-based method includes RF/DC magnetron sputtering (Dhakal, Peng, Tobias, Dasharathy, & Westgate, 2014; Ito & Nakazawa, 1988; Jimbo et al., 2007; Katagiri et al., 2008), evaporation (Hiroi et al., 2013; Katagiri et al., 1997; Kobayashi et al., 2005; Shin et al., 2013) and pulsed laser deposition (Moholkar et al., 2011; Nandur & White, 2014; Sekiguchi et al., 2006). The non-vacuum based method includes chemical vapor deposition (Ramasamy, Malik, & O'Brien, 2011; Washio et al., 2012), spray pyrolysis (Htay et al., 2011; Rajeshmon et al., 2011), chemical bath deposition (Wangperawong et al., 2011), photochemical deposition (Moriya, Tanaka, & Uchiki, 2005), screen printing (Wang, Huang, Lee, Wang, & Gong, 2012; Zhou et al., 2010), electrodeposition (Jiang, Ikeda, Harada, & Matsumura, 2014; Tao et al., 2015), and spin coating (Park et al., 2014; Su et al., 2014). The vacuum based method has advantages of producing CZTS films with high uniformity. Non-vacuum based techniques provides a low- cost, high-throughput roll-to-roll production opportunity of CZTS films. All these methods have been successfully used to fabricate CZTS solar cells with considerable power conversion efficiency.

3.3.9. A Brief Review of CZTS Solar Cell

The first CZTS solar cell with an open circuit voltage of 165 mV was developed by Ito and Nakazawa in 1988 (Ito & Nakazawa, 1988) by incorporating cadmium tin oxide on the CZTS thin film deposited by atom beam sputtering. By annealing the same device, open circuit voltage was increased up to 265 mV (Ito & Nakazawa, 1989). After that, many studies have been done to develop this material as an absorber layer, and intensive research has led to the rapid and continuous development of CZTS solar cell performances. In 1996, Katagiri et al. investigate device characteristics of AZO/CdS/CZTS/Mo/SLG solar cell in which CZTS absorber layer was grown by sulfurization of electron beam evaporated precursors (Katagiri et al. 1996). They report

an efficiency of 0.66 %. By removing the metal oxide particles in CZTS with de-ionized water the conversion efficiency increased to 5.45 % in 2003 (Katagiri et al. 2003).

An efficiency of 6.7 % was reported in 2008 by the same group Katagiri et al., 2008, using a Cu_2ZnSnS_4 thin film deposited by co-sputtering technique (Katagiri et al., 2008). A rapid improvement was then demonstrated, Shin et al., 2013 reported an 8.4 % efficiency solar cell obtained from co-evaporated CZTS (Shin et al., 2013). Vacuum-deposition based CZTS submodules with efficiency increasing from 6.2 (Hiroi, Sakai and Sugimoto, 2011) to 8.6 % (Sugimoto, Hiroi, Sakai, Muraoka, & Katou, 2012) have been reported. To date, the world record efficiencies of 9.2 % and 9.4 % for pure sulfide CZTS solar cell have been achieved by (Hiroi et al., 2013) and (Tajima et al., 2017), respectively. In the case of thin film solar cells based on $Cu_2ZnSnSe_4$ (CZTSe) (Bag et al., 2012) and $Cu_2ZnSn(Se,S)_4$ (CZTSSe) (Wang et al., 2014), a world-record efficiency has been reported with power conversion efficiency of 10.1 % and 12.6 %, respectively. Table 3.5. shows the list of the highest efficiency CZTS solar cells fabricated by different techniques.

Table 3.5. The list of the highest efficiency CZTS solar cells fabricated by different techniques

Deposition technique		**V_{oc} (mV)**	**J_{sc} (mA/cm^2)**	**FF (%)**	**η (%)**	**References**
Vacuum based approach	RF-Sputtering	700	21.3	63	9.4	Tajima et al., 2016
	DC-Sputtering	545	15.44	54.6	4.59	Chalapathy et al., 2011
	Thermal Evaporation	708	21.6	60.1	9.19	Hiroi et al., 2013
	Pulsed Laser Deposition (PLD)	376	38.9	40	5.85	Nandur et al., 2014
Non-vacuum based approach	Spray Pyrolysis	620	15.5	45	4.32	Htay et al., 2011
	Chemical Vapor Deposition (CVD)	658	16.5	55	6.03	Washio et al., 2012
	Spin Coating	558	18.5	51.2	5.29	Park et al., 2014
	Electrodeposition	705	18	63.2	8.10	Jiang et al., 2015

3.4. Buffer layer

The basic function of a buffer layer in a heterojunction is to form a junction with the absorber layer while receiving a maximum amount of light to the junction region and absorber layer (McCandless & Hegedus, 1991). In addition to its obvious function, it helps to protect the absorber layer from the upcoming deposition processes (ion damage during the ZnO/ZnO:Al sputtering) (Kemell, Ritala, & Leskelä, 2005) and to minimize the interface recombination at the absorber/buffer interface (Tanaka, Oonuki, Moritake, & Uchiki, 2009) by smoothing its surface. Moreover, the absorber film becomes more suitable for air exposure while being protected by a buffer layer. The buffer layer must have minimum absorption losses and must be able to drive out photo-generated carriers with minimum recombination losses and transport photo-generated carriers to the outer circuits with minimum electrical resistance. The bandgap of the buffer layer should be sufficiently wide for high optical throughput and the layer should be sufficiently thin to maintain low series resistance. Ideally, carrier density of the buffer layer must sufficiently higher than the absorber, such that most of the space-charge region extends into the absorber, where its electric field helps to separate charge carriers (Klenk, 2001). The higher doping density in the buffer layer reduce the bucking current density by suppressing the minority carrier generation and suppress the interface recombination by holding the Fermi level away from the middle of the band gap at the interface. Lattice mismatch at the junction is also important for epitaxial or highly oriented layers. Out of these items, the conduction band offset (CBO) between the buffer layer and absorber layer is most important to achieve high device performance (Barkhouse et al., 2012). Figure 3.10. shows two different conduction band alignments that can occur in a CZTS solar cell. Positive conduction band offset, which is commonly referred as a spike conformation, forms where the conduction band minimum of the buffer layer is higher than that of the absorber layer (Figure 3.10. (a)). On the other hand, negative conduction band offset, which is commonly referred as a cliff conformation, forms where the conduction band minimum of the buffer layer is lower than that of that of the absorber layer (Figure 3.10. (b)). It is theoretically demonstrated that the CBO at the CIGS/CdS interface should be in the range of 0 to 0.4 eV to achieve high device performance (Liu et al., 2016). For the CBO higher than 0.4 eV, J_{sc} decreases dramatically since the high barrier prevents the flow of light-generated electrons. The cliff conformation inhibits the

flow of injection electrons under forward bias by acting as a barrier and leads to the interfacial recombination between the majority hole carriers in CIGS and accumulated electrons at the CIGS/CdS interface, and thereby losses in V_{oc} and FF (Minemoto et al., 2001; Naghavi et al., 2010; Turcu, Pakma, & Rau, 2002). To sum up, spike conformation with a CBO of 0 eV to 0.4 eV is ideal for CIGS/CdS devices because it does not form a barrier for injection electrons and V_{oc} is nearly constant. Given a similar device configuration, achieving a small spike CBO configuration at the CZTS absorber/buffer layer interface has a great importance to reduce the interface recombination and achieve high CZTS device performance.

To summarize, the most important requirements for a good buffer layer are (Naghavi et al., 2010):

- A sufficiently wide band gap, such that large portion of the incoming radiation can be transmitted to the absorber layer.
- A suitable energy band alignment between the absorber and buffer layer
- A very low defect density at the absorber/buffer interface and/or inversion of the absorber surface with a position of the absorber CB close to the E_F .

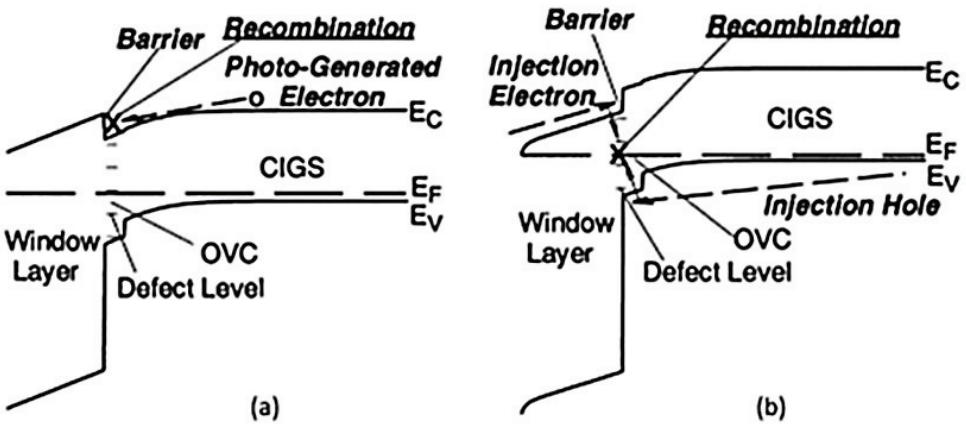

Figure 3.10. Schematics of (a) spike like and (b) cliff like energy band diagram structures. (Source: Minemoto et al., 2001)

In most of the works on CIGS and CZTS based solar cells, the standard device structure includes a very thin CdS buffer layer deposited using chemical bath deposition (CBD) technique since it is the buffer layer that has yielded the best device performances to date. CBD method is regarded as soft due to the low kinetic energy of CdS atoms arrive at the surface. During CBD, the substrate is immersed in a solution containing chemicals

that react with each other and form CdS on the absorber layer. The solution contains ammonia which etch away surface contamination such as organic carbon compounds and oxides. It is believed that this etching is another reason behind the success of CdS (Siebentritt, 2004). In addition, the CBD provides homogenous coatings even for rough surfaces (Naghavi et al., 2010), which allows for a good p-n junction over the entire surface.

However, CdS has a relatively small band gap of 2.4 - 2.5 eV (Dona & Herrero, 1997), which cause undesired absorption of some high energy photons in the 350-550 nm part of the sunlight spectrum. This absorption ultimately limits the short circuit current (Jsc). implementation of a CBD CdS process in a module production line is another drawback from an industrial point of view. CBD solution disposal and waste recycling is a matter of concern as Cd is classified as toxic and carcinogenic (Waalkes, 2000). Several regions in the world have statutory limitations of the usage of Cd in products electrical or electronic equipment which can be a marketing problem for Cd-containing thin film modules. From an industrial and environmental point of view, alternative buffer layers are obviously desirable within CZTS research due to drawbacks of the CdS buffer layer. Many efforts are currently devoted to substitute the CdS buffer layer by other nontoxic low-absorbing buffer layers. The development of Cd-free devices began in 1992 and efficiencies up to 20.9 % has been recently achieved for CIGS solar cell (Frontier, 2014). Out of numerous alternative materials, investigations suggest that the most promising Cd-free materials are In_2S_3, ZnS, ZnMgO and their oxy-hydroxide derivate compositions deposited by various techniques such as atomic layer deposition, magnetron sputtering, chemical bath deposition, evaporation, spray pyrolysis etc. (Naghavi et al., 2010). One approach to replace the CdS in CIGS solar cells is to vary the constituent elements in the semiconductor-alloy buffer layer, i.e. (Zn,Cd)S, (Zn,Mg)O, $(Zn,Sn)O_x$, and Zn(O,S), to get an appropriate conduction band offset between the absorber and buffer. Most of these buffer layers seem to have attained same or even better efficiencies than the CdS references.

So far, some experimental attempts have been made to investigate the performance of CZTS solar cells with Cd-free buffer layers. Conversion efficiencies of the CZTS cells with ZnO buffer have exceeded 5 % (Katagiri, Jimbo, Tahara, Araki, & Oishi, 2009). The effect of ZnS buffer layer thicknesses along with a CZTS absorber layer was investigated and the best solar cell conversion efficiency of 2.11 % was obtained for the ZnS film with a thickness of ~30 nm (Kim et al., 2014). Chen et al,. 2012 developed

a solar cell with structure of fluorine-doped tin oxide (FTO) glass/TiO_2/In_2S_3/CZTS/Carbon, where CZTS absorber layer was prepared by ball milling and screen printing combination processes and In_2S_3 buffer layer was prepared by spray pyrolysis method. conversion efficiency of the best fabricated solar cell was 0.60 % (Chen, Cheng, Zhuang, & Dou, 2012). To the feasibility of the sputtered In_2S_3 buffer layers as a function of their thickness, Combinatorial Reactive built Al/ZnO / In_2S_3 / Cu_2ZnSnS_4 / Mo / SiO_2 structure at optimal processing conditions. Devices with 75 nm In_2S_3 buffer layer deposited at 290 °C showed the performance on par with the CdS/CZTS reference solar cells with ~2% efficiency. Performances of CZTS solar cells with $Zn_{1-x}Sn_xO_y$ (ZTO) buffer layers grown by ALD was investigated by Platzer-Björkman et al., 2015 (Platzer-Björkman et al., 2015). By varying the ALD process temperature, conduction band offset (CBO) value at the CZTS/ZTO interface is tuned and they obtained higher open circuit voltage for the devices with ZTO buffer grown at 95 °C as compared with their CdS reference cells with a top efficiency after 2 min light-soaking of 7.4 %.

Among the different alternatives for CdS, we focused on Zinc oxysulfide Zn(O,S) buffer layers since they are reported as one of the most promising candidates and high efficiency devices have been reported with 21 % efficiency with these layers.

3.5. Zn(O,S) Buffer Layer

Zinc oxysulfide (Zn(O,S)) thin films , which are II–VI compound semiconductors, have been successfully used as phosphor host materials (Sanders & Kitai, 1992) and photo-catalysts (Pandey, Pandey, Pandey, & Mehrotra, 2013) but have recently seen a rapid rise in their usage as buffer layers in solar cells because of their compositional and crystal structure tunability. In addition to its functional tunability, Zn(O,S) buffer layer is also non-toxic and earth abundant. Due to its versatility, Zn(O,S) is an excellent candidate for replacing the traditional CdS as a buffer layer since it is compatible with various absorber layers, such as SnS, CIGS, CIS, and CZTS (Grimm et al., 2010; Grimm et al., 2011; Kieven et al., 2012; Platzer-Björkman et al., 2006; Yousfi et al., 2000).

Zn(O,S) is also denoted as $ZnO_{1-x}S_x$ with $0 < x \leq 1$. The S/(S+O) ratio in $ZnO_{1-x}S_x$ can be easily varied by changing the experimental parameters, for example, changing O_2/Ar gas mixture ratio during sputtering. As their composition is varied, key parameters

such as conduction band offset, bandgap, and conductivity can be precisely tuned (Buffière et al., 2015; Pandey et al., 2014; Platzer-Björkman, Lu, Kessler, & Stolt, 2003; Sinsermsuksakul et al., 2013; Sun et al., 2013).

Zn(O,S) is a mixture of ZnO and ZnS which have large optical band gaps, 3.54 eV (Herve & Vandamme, 1994) and 3.3 eV (Srikant & Clarke, 1998), respectively, whereas the band gap of the Zn(O,S) can exhibit a very strong bowing effect (bowing parameter b of 3 eV) as the S/(S+O) ratio varies (Eicke et al., 2013; Platzer-Björkman et al., 2006), with a minimum energy gap of 2.6 eV for a S/(S + O) ratio of 45 % (Meyer et al., 2004). Figure 3.11. shows bandgap bowing of $ZnO_{1-x}S_x$ thin films deposited by reactive sputtering (Meyer et al., 2004). A large bandgap (2.6 - 3.8 eV) allows a greater collection of high-energy electrons, and thus reducing the photocurrent loss in the short wavelength region. Moreover, recombination at the buffer interface can be minimized by the careful adjustment of the sulfur content (Platzer-Björkman et al., 2006).

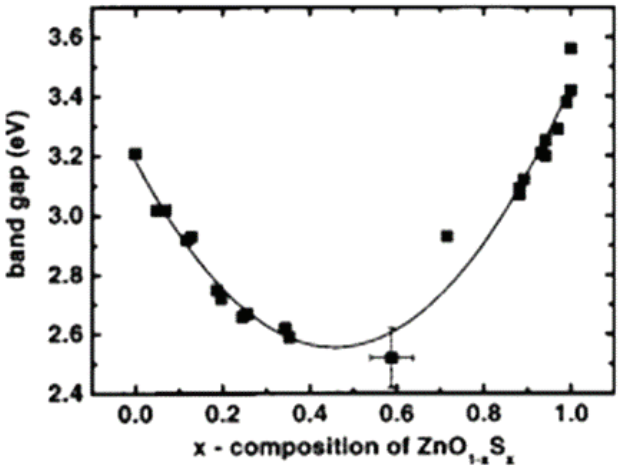

Figure 3.11. Band gap energy of $ZnO_{1-x}S_x$ films as a function of the composition x.

Furthermore, variations of the S and O contents in the Zn(O,S) buffer layer allows the tuning of the conduction band offset (CBO) value at the PN junction interface, giving extra possibility to increase the efficiency. Such tunability of the buffer layer plays an important role in the performance of solar cells, since an optimal moderate spike-like conduction band alignment, which reduce interface recombination without any loss in photo-current collection, at the absorber/buffer heterojunction can be achieved by controlling of the O/S content ratio in the Zn(O,S) buffer layer.

An important issue that limits the performance of CZTS solar cells is the large open circuit voltage deficit (about 0.6 eV), probably due to the non-optimal conduction band alignment between the p-type CZTS absorber and the n-type buffer layer. Since kesterite CZTS was evolved from chalcopyrite CIGS, device structure of CZTS solar cells has inherited from the CIGS solar cell device, where CdS is generally used as standard buffer layer. The conduction band alignment of CdS/CIGS heterojunction is spike-like with an optimal band offset of 0.2 - 0.3 eV, which makes the CIGS solar cell highly efficient. However, in the case of CdS/CZTS based solar cells, the CBO type is still unresolved. While the CBO of CdS/CZTS based cells is theoretically calculated as negative (cliff-like), the reported experimental values vary widely. For example, a cliff-like CBO value of 0.06 eV (Li et al., 2012), 0.33 eV (Bär et al., 2011), 0.34 eV (Santoni et al., 2013) was measured in some studies, whereas Haight et al., 2011 reported a spike-like CBO of 0.41 eV (Haight et al., 2011). Differences in the experimental findings of CBO of CdS/CZTS may be due to the variation in the surface of the CZTS absorber and/or any treatment before the CdS buffer deposition as the band alignment is found to be very sensitive to the CdS/CZTS interface. On the other hand, if the CBO of CdS/CZTS is actually cliff-like, it is necessary to identify alternative buffer layers that ensure an optimal band alignment with CZTS (small spike-like CBO up to 0.5 eV). The optimal conduction band alignment for CZTS should be between the ZnO and the ZnS values as illustrated in Figure 3.12. It has been shown that the pure ZnO buffer layer, which is expected to give a negative conduction band offset with CZTS, works for both CZTS and CZTSSe solar cells (Barkhouse et al., 2012; H. Katagiri et al., 2009). According to the theoretical (Nagoya, Asahi, & Kresse, 2011) and experimental findings, ZnS buffer layer give a high positive conduction band offset with CZTS and cause current blocking due to a high barrier (Barkhouse et al., 2012; Ericson et al., 2014). Zn(O,S) buffer layer can form an optimum CBO with CZTS because its constituent elements can be adjusted to have optimum conduction band alignment between ZnO and ZnS.

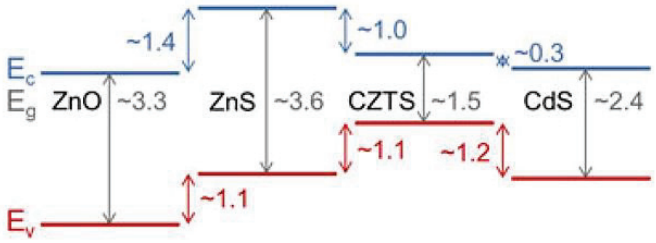

Figure 3.12. Approximate conduction band offsets, valence band offsets and bandgaps for CZTS, ZnS, ZnO, CdS.
(Source: Ericson et al., 2014)

The deposition of Zn(O,S) thin films has been carried out using various deposition methods such as chemical bath deposition (CBD) (Buffière et al., 2011; Kushiya, 2004; Sáez-Araoz et al., 2008; Witte, Abou-Ras, & Hariskos, 2013), atomic layer deposition (ALD) (Platzer-Bjorkman, Kessler, & Stolt, 2003; Platzer-Björkman et al., 2006; Sanders & Kitai, 1992; Zimmermann, Ruth, & Edoff, 2006), ion layer gas reaction (ILGAR) (Muffler et al., 2000), evaporation (Romeo, Gysel, Buzzi, & Abou-Ras, 2004), sputtering (Grimm et al., 2010; Grimm et al., 2011; Klenk et al., 2014; Kobayashi, Kumazawa, Kao, & Nakada, 2013; Nakamura et al., 2013), and pulse laser deposition (PLD) (Deulkar, Huang, & Neumann-Spallart, 2010; Yoo et al., 2002). Despite the differences in the deposition methods used by the various groups, majority of the research groups use a Zn(O,S) buffer of about 50-100 nm.

Doping of S into ZnO was firstly performed by Yoo et al., 2002 using pulsed laser deposition (PLD) technique (Yoo et al., 2002). They showed that the S concentration in the single-phase wurtzite Zn(O,S) thin films deposited on c-plane sapphire at 700 °C was limited to 0.13 and above that $ZnSO_4$ phase appeared in addition to ZnS and ZnO. They also observed that both the band gap and the c-axis lattice constant showed a nonlinear correlation with the variation of S content in the films. Meyer et al., 2004 succeed to synthesize single-phase wurtzite $ZnO_{1-x}S_x$ films almost in the whole composition range on both glass and c-plane sapphire substrates at a relatively low substrate temperature of 340 °C by RF reactive sputtering and using a ZnS ceramic target with Ar/O_2 as reactive gases (Meyer et al., 2004). They observed that the c-axis lattice constant changed linearly as the energy gap changed nonlinearly with the sulfur content in the Zn(O,S) alloys, and an optical bowing parameter was determined as 3.0 eV. Locmelis et al., 2007 found nearly symmetrical solubility of about 5 mol % for $ZnO_{1-x}S_x$ crystals grown by chemical transport reactions at 900 °C (Locmelis et al., 2007). Using a technique similar to Meyer et al., 2004, Pan et al., 2010 deposited the $ZnO_{1-x}S_x$ films on glass substrates at 300 °C

with post-annealing at 500–600 °C (Meyer et al., 2004; Pan et al., 2010). They realized that wurtzite structure with (002) preferred orientation occurred in the O-rich region ($0 \leq x \leq 0.23$) and zinc blende structure with (111) preferred orientation occurred in S-rich region ($0.77 \leq x \leq 1$). Two phases of w- and β- $ZnO_{1-x}S_x$ coexisted in the composition range of $0.23 < x < 0.77$. While these different observations can be explained by different techniques and growth conditions used in different researches, it is clear that more research is needed in this direction.

The highest reported efficiencies for CIGS solar cells have been achieved by the Zn(O,S) buffer layers deposited either by CBD or ALD, 20.9 % (Frontier, 2014) and 21.0 % (Friedlmeier et al., 2015), respectively. When grown by CBD, it is reported that Zn(O,S) layer is a mixture of ZnS, ZnO and $Zn(OH)_2$ (Bhattacharya, Ramanathan, Gedvilas, & Keyes, 2005; Nakada & Mizutani, 2000) and control of the chemical composition of the films is a challenging task. So far, the effect of the sulfur to oxygen ratio on the band structure of Zn(O,S) films grown by ALD has been studied and the importance of this ratio for the operation of the device has been emphasized (Persson, Platzer-Björkman, Malmström, Törndahl, & Edoff, 2006). $ZnO_{1-x}S_x$ films with tunable x can also be grown by sputtering with higher deposition rates. Recently, CIGSe devices with efficiencies exceeding 18 % were also obtained by using a Zn(O,S) buffer layer grown by RF-sputtering from a mixed target with an argon pressure of 5 μbar (Klenk et al., 2014).

So far, very few experimental attempts have been made to investigate the performance of CZTS/$ZnO_{1-x}S_x$ devices (pure sulfide). Tove et al., 2014 evaluated sulfur to oxygen ratios of $ZnO_{1-x}S_x$ films grown by ALD to find an appropriate conduction band offset between the CZTS absorber and the $ZnO_{1-x}S_x$ buffer (Ericson et al., 2014). The best CZTS/$ZnO_{1-x}S_x$ device with an efficiency of 4.6 % was achieved by Zn(O,S) 6:1 buffer, which has the same optimum composition as for CIGS (Zimmermann et al., 2006), and the best reference cell with CdS buffer gave 7.3 % efficiency.Band alignment between CZTS absorber and Zn(O,S) buffer was investigated using X-ray Photoelectron Spectroscopy (XPS) and Near Edge X-ray Absorption Fine Structure (NEXAFS) Measurements (Yan et al., 2014). The CBO value between CZTS and $ZnO_{1-x}S_x$ buffer with sulfur content x = 0.4 - 0.5 was found to be spike-like with CBO_{XPS} = 0.92 ± 0.10 eV and CBO_{NEXAFS} = 0.87 ± 0.10 eV. CZTS/Zn(O,S) heterojunction was tested in full photovoltaic device form. However, no efficiency was measured for the device with a Zn(O,S) buffer due to the high CBO of around 0.9 eV which blocks all of the photo-

generated electrons from CZTS. Ling-Yan Lin, et al. 2016 simulated a CZTS/Zn(O,S) heterojunction solar cell using a one-dimensional solar cell simulation software analysis of microelectronic and photonic structures (AMPS-1D) to optimize the composition in the $ZnO_{1-x}S_x$ buffer layer, which would yield higher conversion efficiency (Lin, Qiu, Zhang, & Zhang, 2016). The simulation results showed that the conduction band offset at CZTS/Zn(O,S) interface depends critically on the S/(S+O) ratio in Zn(O,S) and can range from -0.23 eV to 1.06 eV. They proposed that the optimal CBO of 0.23 eV can obtained be by the $ZnO_{1-x}S_x$ film with sulfur content x = 0.6 and a solar cell efficiency of up to 17.55 % can be achieved by this sulfur content.

3.6. Window Layer: ZnO and Al:ZnO

The most common window layer used in CZTS solar cells consists of two layers. The first layer is a thin Zinc oxide (ZnO) film, which typically has a thickness of about 50 nm. The second layer consists of aluminum doped ZnO (AZO) front contact. Thickness of the AZO layer are determined by a trade-off between transparency and conductivity and it is typically 300-500 nm.

The II-VI semiconductor compound Zinc oxide is an n-type semiconductor with a wide direct band gap of 3.4 eV (Janotti & Van de Walle, 2009) at room temperature, which results in high transparency throughout the visible spectrum (its band gap corresponds to UV light of 365 nm). Undoped ZnO thin film shows n-type conductivity with a very high background electron concentration (Lee et al., 2000). The n-type conductivity of undoped ZnO is attributed to intrinsic donor defects, such as oxygen vacancies (V_O) and interstitial zinc atoms (Zn_i). Zinc oxide typically crystallizes in the hexagonal wurtzite structure as it is most stable at ambient conditions. Pure, ordered ZnO has lattice constants of a = 0.325 nm and c = 0.521nm with a c/a-ratio of about 1.60 at ambient conditions (Reeber, 1970), while the ideal wurtzite structure shows a c/a-ratio of 1.63. ZnO can also exhibit rock-salt structure (Bates, White, & Roy, 1962; Serrano et al., 2004) relatively high pressures about 10 GPa or zinc-blende structure (Ashrafi et al., 2000) upon growth on cubic substrates. The ZnO film usually grow at (001) preferred direction, with the c-axis perpendicular to the substrate surface.

To fabricate ZnO layer, many growth techniques such as pulsed laser deposition, metalorganic chemical vapor deposition, spray pyrolysis, RF magnetron sputtering have

been used. Among them, RF magnetron sputtering is the most commonly used technique since it avoids using toxic gases, reduces losses and provides good adhesion of the grown material and good thin film homogeneity with desired crystallographic orientation [111]. The properties of sputtered ZnO thin films can be controlled by varying the RF power, working pressure and the substrate temperature.

ZnO has been proven to be the most promising transparent conducting oxide for thin film solar cells. Although impact of this layer on the general performance of a CZTS solar cell is not exactly understood, it has been claimed that this layer helps to improve cell performance. This additional buffer layer is usually employed in order to prevent shunting, since the resistance generated by this layer reduce the negative effects of recombination currents at grain boundaries or at shunts (Rau & Schmidt, 2001). Moreover, it helps covering the areas of buffer layer not deposited properly, so preventing short-circuits between the absorber layer and the front contact (Jahagirdar, Kadam, & Dhere, 2006). It also helps prevent the buffer layer interface from being damaged by the energetic ions during sputtering and functions as a seed layer which enhances the grain growth of AZO layer (Lee et al., 2000).

The function of Transparent Conductive Oxide (TCO) layer is to allow all wavelengths beneath cut-off wavelength to be transmitted till the absorber layer and allow electrical conduction to the contact grid (Johnston, 2010). SnO_2:F (FTO), In_2O_3:Sn (ITO), and highly doped ZnO, namely with gallium (GZO), aluminum (AZO), or boron (BZO) are the most commonly used transparent conducting oxide materials in thin film solar cells (Gordon, 2000). However, FTO is not used in chalcopyrite-based devices because it requires deposition temperatures higher than 200 °C and ITO is not commonly used due to its high cost and toxic properties. In this regard, doped ZnO is considered as an alternative due to its lower material cost, high band gap, non-toxic nature, and high transparency (Ellmer, Klein, & Rech, 2008).

AZO is currently most used material for making transparent conducting electrodes. Electron doping in AZO is obtained by substitution of Zn ions in ZnO by Al ions. Since AZO thin films were first reported in 1971 (Wasa, Hayakawa, & Hada, 1971), Al concentration of AZO films have varied from 0.8 % to 5 %. 2 at % of Al in AZO have been considered to have better electrical and optical performance by many researchers.

AZO exhibits an n-type conductivity has band gap of about 3.6 eV. The high band gap of AZO originates from its high carrier concentration. AZO also has the key features of TCO with high electrical conductivity and high optical transparency. Additionally, one

should note that the thickness of AZO layer plays an important role in optimizing transmission and conductivity. Generally, a thicker layer has better conductivity but worse transmission since increased thickness provides an improvement in the surface morphology, so the charge carriers cannot recombine easily; however, there are more atoms to absorb radiation.

Usually, these layers are grown by many different methods, such as, pulsed laser deposition (PLD) (Ou et al., 2011), chemical vapor deposition (Terasako et al., 2007), and sputtering (Paul et al., 2008). A high deposition temperature above 300 $^{\circ}$C is necessary to get a desired TCO property in most of these methods since higher temperature provides an improvement in the crystallinity of the thin films. However, higher temperature generates a large number of defect states due to increased interfacial diffusion and cause high charge carrier recombination rate. Therefore, a room temperature (RT) deposition process is required to avoid inter-diffusion between the layers of a solar cell (Ferekides et al., 2000) and to grow AZO films on flexible substrates (Tsai & Staack, 2011). However, it is still challenging to achieve low resistivity and high transmittance simultaneously at RT for AZO.

CHAPTER 4

EXPERIMENTAL PROCEDURES

4.1. Device Structure

Figure 4.1. shows the schematic cross section of CZTS solar cell fabricated in this work. All thin films in this solar cell structure are deposited entirely using only the magnetron sputtering technique since sputtering offers a wide range of advantages, such as high adhesion of films, excellent coverage, easy adaptation to large-scale and reproducible manufacturing.

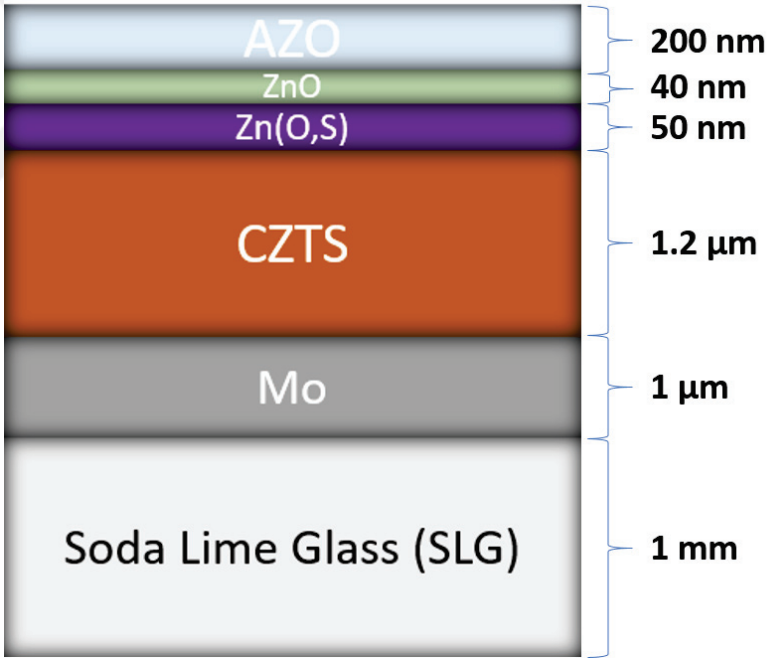

Figure 4.1. Schematic cross section of CZTS solar cell.

Starting from the bottom, the SLG substrate gives support and rigidity to the thin solar cell layers. A molybdenum (Mo) layer with the thickness around 1 µm serves as the low resistance, ohmic back contact, besides it reflects unabsorbed light back into the CZTS absorber. On top of Mo layer, a p-type CZTS absorber layer grown by two-stage process. As the absorber layer thickness increases more photons are absorbed generating

more number of excess carriers. This leads to higher efficiency. However, since more photons are absorbed with increase in absorber layer thickness, recombination increases due to finite carrier diffusion length. Moreover, thick absorber layer increases fabrication cost. Therefore, CZTS absorber layer with the thickness of 1.2 μm was used for the present work. As previously mentioned, an n-type layer is required to complete the p-n junction with CZTS. Historically, this layer consisted of only one material, but then it turned into three separate layers with the collective name window layer stack. The reason for specifying it as a window is that all the materials in the stack are transparent or almost transparent. At the bottom of the window layer stack, a thin n-type Zn(O,S) buffer layer (50 nm) is added right on top of the CZTS absorber. The importance of this layer is to define the quality of the p-n junction and the device performance. The thickness of the buffer layer should be as small as possible to decrease the series resistance of the device. However, very thin buffer layer reduces the space charge width of the junction and thus cause poor photo current collection. It may also result in higher leakage current. On the other hand, thicker buffer layer decreases the quantum efficiency of the device since it absorbs more number of photons which cannot reach the CZTS absorber. An intermediate 40 nm thick layer of unintentionally n-type doped ZnO is deposited above the buffer layer. This layer has a significantly reduced conductivity compared to the top layer, and as such increasing thickness of the device increases R_s, thus a thin layer is useful for FF. The top of the window layer stack is about 200 nm thick layer of the Al doped which collects and conducts electrons out of the device.

The methods used in this thesis for the fabrication of materials as well as devices are briefly presented in the following section.

4.1.1. Substrate Preparation

In this work, Mo coated soda lime glass (SLG) substrates were used to investigate the performance of solar cell stack. Prior to deposition of Mo, SLGs were ultrasonically cleaned in acetone, methanol and deionized water, respectively, for 10 minutes, and then exposed to N_2 plasma for 10 minutes at 100 W RF bias.

4.1.2. Molybdenum Back Contact

DC magnetron sputtering was used to deposit Mo onto the SLG substrate. Deposition parameters of sputtering process determine the quality of the Mo thin films. The working pressure has an important influence on the properties of the Mo thin films, determining the resistivity and adhesion of the Mo film to SLG substrate. Mo films produced at lower working pressure has higher density, lower resistivity, and smoother surface, but adhesion problems arise due to compressive stresses. In addition, high sputtering power and low sputtering voltage decrease resistance and increase the adhesion of the Mo film to SLG substrate (Karthikeyan, Zhang, & Campbell, 2014; Scofield, Duda, Albin, Ballard, & Predecki, 1995). Bi-layer deposition process is used to ensure good adhesion to SLG and good electrical properties. The deposition of Mo is started at a higher working pressure (12.5 mTorr) and then decreased to lower working pressure (2.5 mTorr).

Figure 4.2. shows the magnetron sputtering system used for the deposition of Mo, Zn(O,S), ZnO and AZO layers in our experiments. This system has 3 guns with a water cooling channel, gas entrance and power connections. A rough pump and a turbo molecular pump (TMP) are used to reach high vacuum region (3.0 10^{-6} Torr). A gate valve with a stepper motor is connected to the system in front of TMP. To measure base pressure of the system, a thermocouple and a cold cathode gauge is used. After reached to base pressure, Argon gas (purity 99.99 %) is flowed to the chamber using a mass flow controller. The DC or RF bias are exploited to produce and to sustain plasma inside the chamber. Baratron is used to measure pressure of the vacuum chamber during the deposition.

Mo and AZO layers were deposited by DC sputtering. As schematically illustrated in Figure 4.3., during deposition of Mo and AZO, sample holders were rotated around the center of chamber by rotational feedthrough to obtain better surface homogeneity of the layers. Zn(O,S) and ZnO layers were deposited by RF sputtering with fixed sample holders (Figure 4.4.).

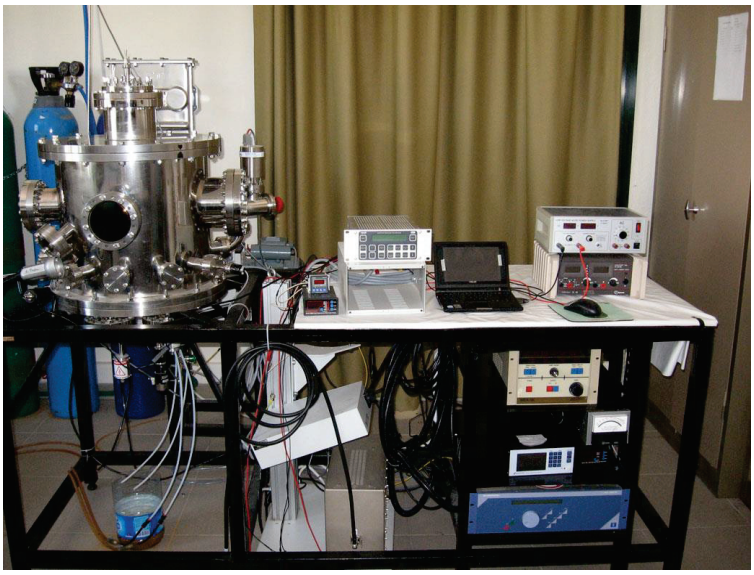

Figure 4.2. Picture of our magnetron sputtering system used for the deposition of Mo, Zn(O,S), ZnO and AZO layers.

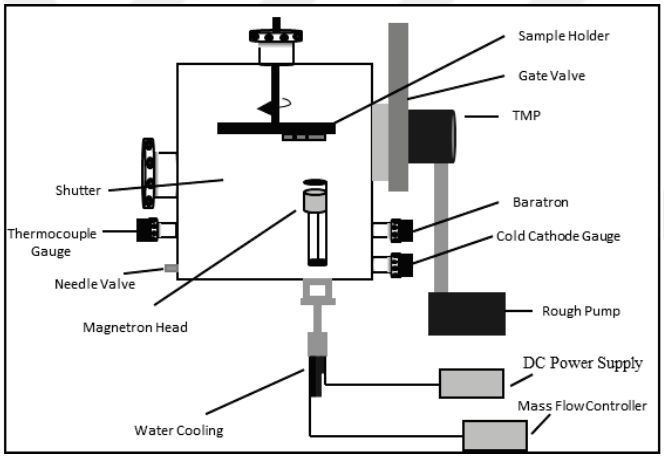

Figure 4.3. Schematic illustration of magnetron sputtering system with rotating sample holder.

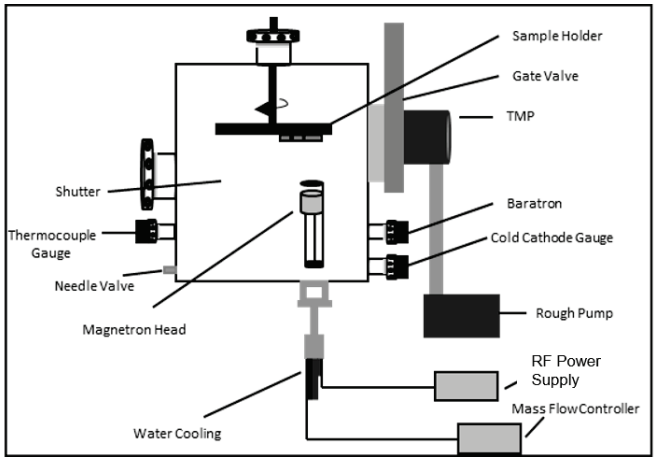

Figure 4.4. Schematic illustration of magnetron sputtering system with fixed sample holder.

Mo films were deposited by DC magnetron sputtering on soda-lime glass substrates from 2-inch-targets of Mo with a purity of 99.95 %. The SLGs was loaded in the system and the chamber was evacuated to a base pressure of 2.0 10^{-6} Torr. After the chamber was backfilled with 30 sccm (cubic centimeters per minute at standard temperature and pressure) argon, pre-sputtering was performed for 5 minutes to remove the contamination of the surfaces of the target, then shutter was opened. The deposition of Mo was started at a higher working pressure (12.5 mTorr) and then decreased to lower working pressure (2.5 mTorr) for the Mo layers with a bi-layer structure. Working pressure was adjusted by changing the valve position. Sample holder was rotated around the center of chamber by rotational feedthrough to obtain better surface homogeneity. Substrate distance from the target surface was fixed at 9 cm. The deposition parameters are listed in Table 4.1. The total thickness of Mo layers with a bi-layer structure is around 1μm.

During the sulfurization process of CZTS absorber, an intermediate MoS_2 layer would be produced as a result of the reaction of Mo with S, and it forms an ohmic contact at Mo/CZTS interface. If this MoS_2 is thin enough, it has no detrimental effect on device performance, but if the MoS_2 is too thick, it will reduce the performance of the device and even cause the CZTS films to peel off from the substrates.

Table 4.1. Deposition parameters for the Mo layers with a bi-layer structure.

	Mo Layer 1	**Mo Layer 2**
DC Power	75 W	75 W
Gas Flow	30 sccm Ar	30 sccm Ar
Working pressure	12.5 mTorr	2.5 mTorr
Valve Position	50 % Open	100 % Open
Deposition Time	140 min	70 min

4.1.3. CZTS absorber layer

In this study, fabrication of CZTS thin films was performed by a two-stage process: firstly, a stack of Cu/Zn/Sn metal precursors were deposited by magnetron sputtering, then this stack was annealed under sulfur atmosphere. Two-stage processes are suitable for large-scale module production (as for CIGS) (Luque & Hegedus, 2011) and have high potential to achieve high cell efficiency.

4.1.3.1. Metallic Precursor Deposition

In the first stage of the process, Copper, Zinc, and Tin metallic precursors were deposited sequentially on 1 μm Mo coated soda-lime glass substrates by multi target DC magnetron sputtering from 2-inch-targets of Cu (99.999%), Zn (99.99%) and Sn (99.999%) at room temperature.

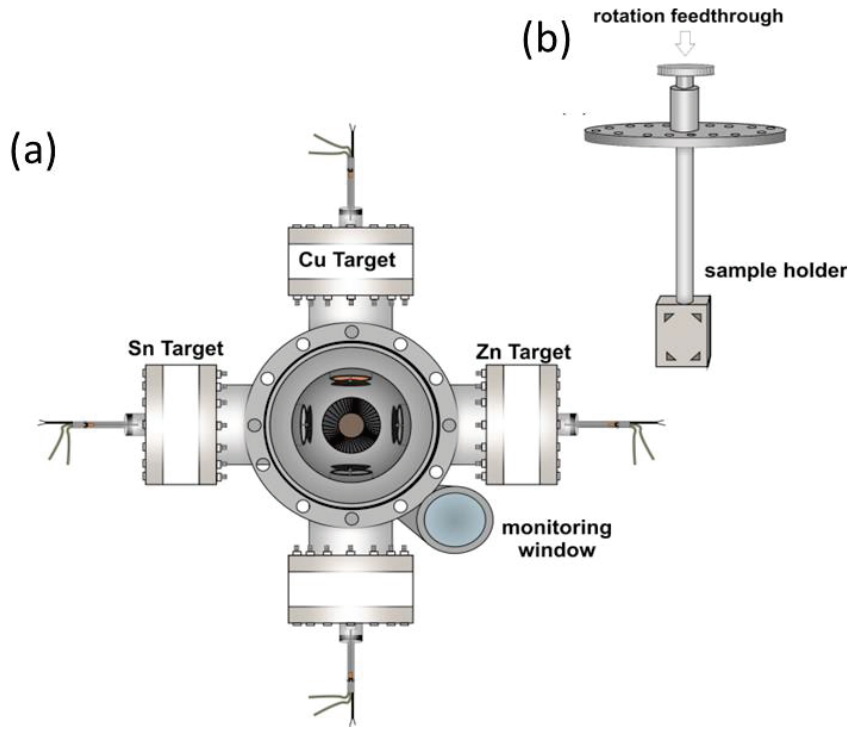

Figure 4.5. (a) Schematic top view of multi target DC magnetron sputtering system (b) Illustration of rotating sample holder.

The Figure 4.5. represents schematic of multi target DC magnetron sputtering system that is used for Copper, Zinc, and Tin metallic precursors deposition. This system has 4 guns with a water cooling channel, gas entrance and power connections. A rough pump and a TMP are used to reach high vacuum region (8.0 10^{-6} Torr). To measure base pressure of the system, a thermocouple and a cold cathode gauge is used. After reached to base pressure, Argon gas (purity 99.99 %) is flowed to the chamber using a mass flow controller. The DC voltage is exploited for all the targets to produce and to sustain plasma inside the chamber. Rotational sample holder is used to deposit metallic precursors sequentially on Mo coated SLG substrates. To measure pressure of the vacuum chamber during the deposition, baratron is used.

The Mo coated SLGs were loaded in the system and the chamber was evacuated to a base pressure of 8.0 10^{-6} Torr. After the chamber was backfilled with argon to a pressure of 5.0 10^{-3} Torr, pre-sputtering was performed for 5 minutes to remove the contamination of the surfaces of the targets. In order to grow sequentially layered metallic precursors in the Cu/Sn/Zn/Cu layer ordering, DC bias applied to the Cu, Zn, Sn and Cu targets, respectively. The deposition parameters and thicknesses of metal precursors are shown in Table 4.2. Substrate distance from the target surface was fixed at 8 cm for all experiments. After deposition steps, the pressure of the chamber was reached to atmosphere pressure to remove the substrate holder from the chamber.

Table 4.2. The deposition parameters and thicknesses of metal precursors.

	Cu (120 nm)	**Sn (290 nm)**	**Zn (165 nm)**	**Cu (55 nm)**
Power Supply	41 W	40 W	20 W	41 W
Gas Flow	30 sccm	30 sccm	30 sccm	30 sccm
Deposition Time	4 min	6 min+9 s	55 s	1 min+50 s

To obtain precursors with the desired composition and good adhesion properties, the deposition process was optimized by selecting the appropriate Ar pressure and the sputtering power of each target. Sputtering power and deposition time were adjusted to obtain a 630 nm thick precursor to have Cu, Sn and Zn layers with the thickness of 175, 165 and 290 nm, respectively. These metal ratios were chosen by considering the stoichiometry reported in the literature for most efficient CZTS based solar cells which have Zn-rich and Cu-poor nominal composition, close to Cu:Zn:Sn:S= 1.80:1.20:1.00:4. (Wang et al., 2010).

The thickness of the CZTS film must be in a certain range to optimize the light absorption. Too thin absorber layer doesn't absorb all the incident radiation, thus generation of electron-hole pairs is reduced in the active area of the CZTS solar cell. On the other hand, thick absorber layers lead to waste of materials in usage. A film thickness between 1 and 3 μm is sufficient to absorb most of the incident radiation for CZTS absorber layer with an absorption coefficient greater than 10^4 cm^{-1}. Precursor thicknesses of 630 nm is sufficient to have CZTS films having thickness higher than 1 μm when incorporation of sulphur during sulfurization is considered.

These metal ratios were calculated by considering the stoichiometry reported in the literature for most efficient CZTS based solar cells which have Zn-rich and Cu-poor

nominal composition, close to Cu:Zn:Sn:S= 1.80:1.20:1.00:4. The molar mass of the metallic precursors were determined using the density and atomic weight of the metals listed in Table 4.3. as follows:

$$M_{Cu} = 1.8 \text{ mol} * 63.55 \text{ g/mol} = 114.39 \text{ g}$$
$$M_{Zn} = 1.2 \text{ mol} * 65.38 \text{ g/mol} = 78.456 \text{ g}$$
$$M_{Sn} = 1.0 \text{ mol} * 118.7 \text{ g/mol} = 118.70 \text{ g}$$

The volumes of each element were calculated as follows:

$$V_{Cu} = 114.39 \text{ g} / 8.96 \text{ g.cm}^{-3} = 12.766 \text{ cm}^3$$
$$V_{Zn} = 78.456 \text{ g} / 7.14 \text{ g.cm}^{-3} = 10.988 \text{ cm}^3$$
$$V_{Sn} = 118.7 \text{ g} / 7.31 \text{ g.cm}^{-3} = 16.240 \text{ cm}^3$$

The thickness percentage of Cu, Zn, and Sn were calculated as 31.92 %, 27.47 %, and 40.61 %, respectively. For a 630 nm thick precursor, the thickness of Cu, Zn, and Sn layers should be about 201, 173, and 255 nm, respectively. However, since we observed high amount of Sn loss in the final CZTS thin films in our preliminary works, we set the thickness of Cu, Zn, and Sn layers as 175, 165, and 290 nm, respectively. Table 4.4. shows the chemical composition of stacked metal precursor deposited on Mo-coated SLG with Cu-poor and Zn-rich composition.

Table 4.3. Density and atomic weight of Cu, Zn, and Sn.

Element	Density (g/cm3)	Atomic Weight (g/mol)
Cu	8.96	63.55
Zn	7.14	65.38
Sn	7.31	118.7

Table 4.4. Chemical composition of stacked metal precursor deposited on Mo-coated SLG.

Cu (at %)	Zn (at %)	Sn (at %)	Zn/Sn	Cu/(Zn+Sn)
42.5	30.65	26.85	1.14	0.74

Furthermore, Copper, Tin, and Zinc metallic precursor stacks were deposited onto the substrates in a specially designed sequence. Layer ordering of precursors was

chosen as Cu/Sn/Zn/Cu to minimize tin loss during the sulfurization process, to prevent the ZnS formation over the surface CZTS and to prevent vacancies caused by Cu diffusion. Using the same stacking order, we fabricate two types of precursors having different thicknesses of Cu. The structure of Type 1 is SLG/Mo/Cu(55nm)/Sn(290nm)/Zn(165nm)/Cu(120nm) and Type 2 is SLG/Mo/Cu(120nm)/Sn(290nm)/Zn(165nm)/Cu(55nm) (Figure 4.6.).

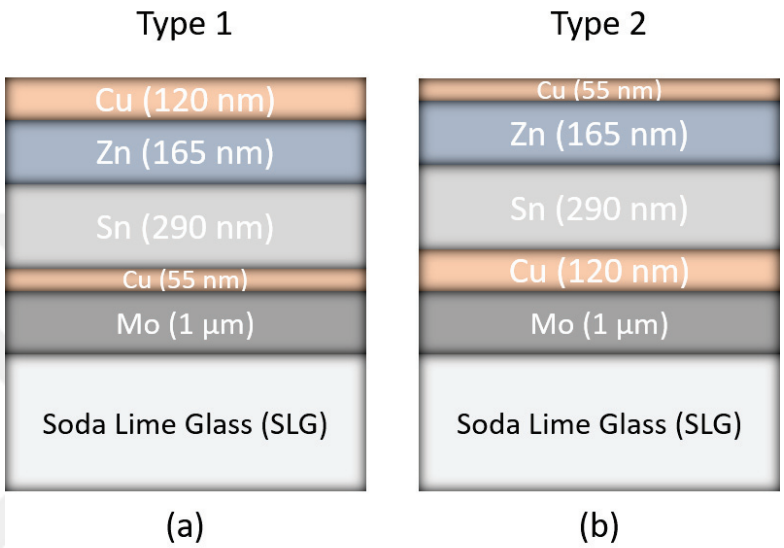

Figure 4.6. Schematic illustration of metallic precursors on the substrate for (a) Type 1 and (b) Type 2.

4.1.3.2. Sulfurization of the metallic precursor

Sulfurization of the metallic precursor to synthesize CZTS absorber layer was performed in a Lindberg/Blue M tube furnace under Ar atmosphere. Schematic of the sulfurization setup is shown in Figure 4.7. The precursor stack was positioned on the middle of the quartz tube on a graphite support which has a good thermal conductivity and was used to provide a low temperature gradient throughout the thickness of the sample. 600 mg sulfur powder (Scharlau, synthesis grade, 99 % purity) in a graphite box was weighted and placed 18 cm away from the precursor stack into the quartz tube. 70 sccm Ar was flowed into the quartz tube by a MKS 647C mass flow controller as a carrier gas during the sulfurization process. Schematic illustration of sulfurization of metallic precursors can be seen in Figure 4.8. The pressure of the quartz tube was maintained at atmospheric level. Ramping and dwell time at a certain temperature could be programmed

using this oven. Specific temperature profile was fallowed during sulfurization (Figure 4.9.): ramp of 10 °C per minutes is used and firstly stopped at 270 °C for three minutes to provide formation of binaries like CuS, SnS, ZnS and then raised to 550 °C, a temperature was maintained at 550 °C for 30, 45 and 60 min to investigate the effect of sulfurization time on the properties of CZTS films. Afterwards, the films were cooled naturally (about 1 hour). Table 4.5. shows the parameters for the sulfurization process of CZTS films used in this study.

Effect of sulfurization temperature, amount of sulfur powder and Ar gas flow were investigated during the preliminary experiments to improve the material quality in terms of both morphology and PV performances. Based on the results of our preliminary studies, CZTS thin films were produced at 550 °C with a sulfur amount fixed at 600 mg and 70 sccm Ar flow. Moreover, the effect of sulfurization time will be discussed in Chapter 5.

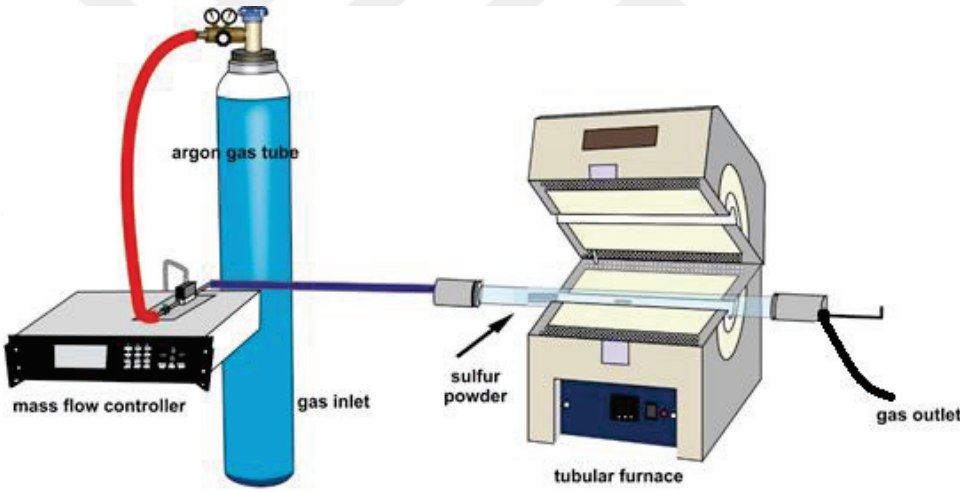

Figure 4.7. Schematic view of sulfurization set up.

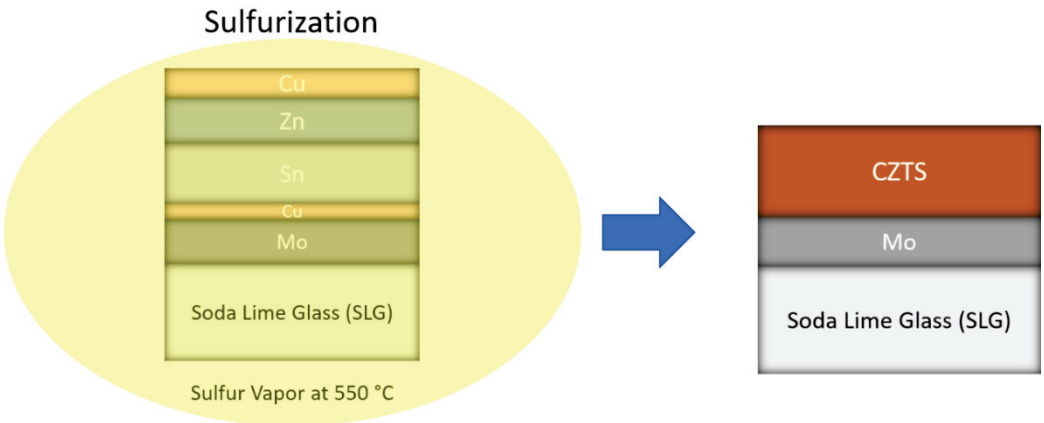

Figure 4.8. Schematic illustration of sulfurization of metallic precursors.

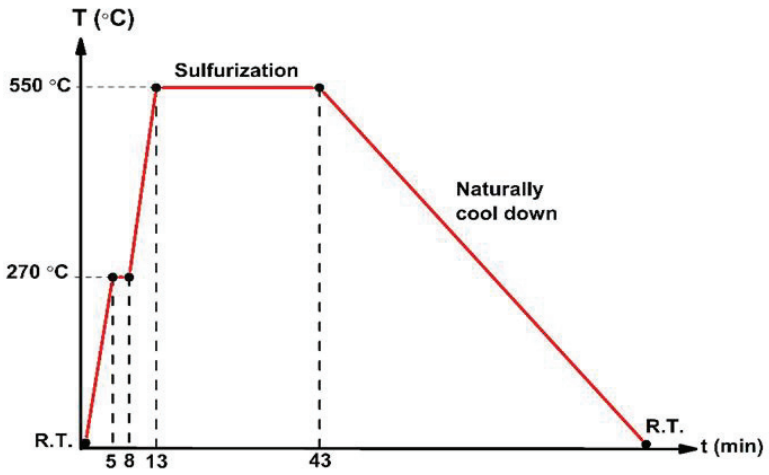

Figure 4.9. Temperature profile of sulfurization.

Table 4.5. Sample growth parameters.

		Layer Ordering	Cu Thickness (nm)		Sulfurization Temperature (°C)	Sulfurization Duration (min.)
			bottom	top		
Type 1	Sample A	Cu/Sn/Zn/Cu	55	120	550	30
	Sample B	Cu/Sn/Zn/Cu	55	120	550	45
	Sample C	Cu/Sn/Zn/Cu	55	120	550	60
Type 2	Sample D	Cu/Sn/Zn/Cu	120	55	550	30
	Sample E	Cu/Sn/Zn/Cu	120	55	550	45
	Sample F	Cu/Sn/Zn/Cu	120	55	550	60

4.1.4. Fabrication of Zn(O,S) Buffer Layer

Zn(O,S) ($ZnO_{1-x}S_x$) buffer layers with a thickness of 50 nm were deposited on fabricated CZTS absorber layers by reactive RF magnetron sputtering (Figure 4.2.) from a ceramic ZnS target with 2-inch diameter. Zn(O,S) films with a thickness of 50-150 nm were also deposited on SLG substrates to characterize Zn(O,S) as isolated film. Before the deposition, pre-sputtering was performed for 5 minutes. Typical deposition parameters were a base pressure of 2.0 10^{-6} Torr, an RF power of 40 W and target to substrate distance was 8 cm. During deposition, substrate temperature was fixed at 200 °C to improve the crystalline quality and the adhesion of the films. Ar and O_2 gases were used as working and reactive gases, respectively. Ar was fixed at 50 sccm and oxygen was varied from 0 % to 2% such that the percentage of O/(Ar + O) during the deposition was 0.66-2.91 %, which resulted in Zn(O,S) layers with different compositions. While the sulfur concentrations of $X_s = 0.8$, $X_s = 0.66$, $X_s = 0.57$ and $X_s = 0.53$ were determined

by XPS, sulfur concentrations of $X_s = 0.21$ and $X_s = 0.03$ were estimated using Vegard's law as discussed in Chapter 5. S/(S+O) ratio of Zn(O,S) can be easily controlled by O/(Ar + O) ratio. S/(S + O) ratio with respect to O/(Ar + O) ratio is given in Table 4.6. The working pressure was in the range of 5.0-10.0 mTorr. Since the deposition rate was varying significantly with the oxygen partial pressure and the desired thickness was obtained by adjusting the deposition time, i.e. typical film thickness was 50 nm for 20 minutes of sputtering at O/(Ar + O)= 1 %.

Table 4.6. S/(S+O) ratio with respect to O/(Ar+O) ratio of the Zn(O,S) thin films.

Xs (S/S+O)	O/(Ar+O) %	O (sccm)	Ar (sccm)
0.8	0.66	0.5	75
0.66	0.83	0.5	60
0.57	0.99	0.5	50
0.53	0.99	0.5	50
0.21 (estimated)	1.48	0.75	50
0.03 (estimated)	2.91	1.5	50

4.1.5 ZnO Layer Deposition

The ZnO layers with a thickness of 40 nm were deposited on Zn(O,S) buffer layers by using a RF magnetron sputtering system shown in Figure 4.4. at room temperature. 2-inch diameter ZnO (99.99%) target was employed to fabricate ZnO layers. The n-type ZnO layer was deposited in pure argon ambient with 80 sccm gas flow. Pre-sputtering was performed for 5 minutes before the deposition, then shutter was opened. Typical deposition parameters were a base pressure of $3\ 10^{-6}$ Torr, a working pressure of $8.4\ 10^{-3}$ Torr, an RF power of 50 W and target to substrate distance was 9 cm.

4.1.6 ZnO:Al Layer Deposition

Transparent conductive AZO layer was deposited onto ZnO layer by DC magnetron sputtering (Figure 4.3.) from 2-inch- ceramic targets of $ZnO:Al_2O_3$ ((98 wt.% ZnO and 2 wt.% Al_2O_3)) at room temperature.. The target was pre-sputtered for 5 minutes. Deposition was performed with an DC power of 50 W and 50 sccm argon gas flow for 120 minutes. During the deposition, the working pressure was in the range from 3-5 mTorr.

For AZO thin films, achieving low resistivity and high transmittance simultaneously at room temperature is still challenging. We demonstrate that the crystallinity and resistivity of AZO films fabricated at room temperature can be improved by off-center deposition with rotating the sample holder (Figure 4.10.). Sample holder was rotated around the center of chamber by rotational feedthrough during the deposition AZO to enhance film uniformity. The vertical distance between the target and the substrate holder was 9 cm. The oxygen atoms at the surface of the AZO target is ionized during the sputtering which can reach the substrate with sufficient energy to get implanted and can cause stress on the films. In order to avoid the direct bombardment of high-energy negative ions on the surface, samples were located to the rotating sample holder in off-center con figuration (position 1) during the deposition of AZO layer on ZnO layer and rotation speed of holder was 6.3 rpm (see Table 4.7.). Moreover, we investigate the effect of rotation speed and the location of the samples on the sample holder on the properties of AZO films deposited on SLG. For this aim, SLG are located onto the rotating sample holder both just above the target (position 0) and in off-center configurations (position 1 and 2).

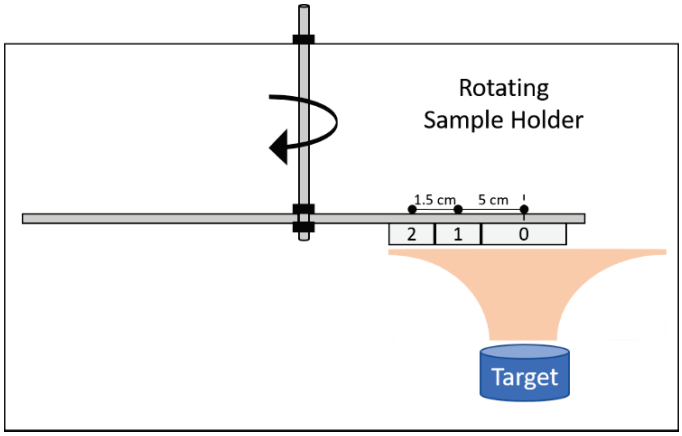

Figure 4.10. Sample positions on rotating sample holder.

Table 4.7. Deposition parameters of AZO thin films.

Substrate Position	Distance from the target center (cm)	Rotation Speed (rpm)	Thickness (nm)
0	0.0	0.0	600
1	5.0	0.0	450
2	6.5	0.0	250
0	0.0	3.3	230
1	5.0	3.3	182
2	6.5	3.3	142
0	0.0	6.3	190
1	5.0	6.3	165
2	6.5	6.3	135
0	0.0	12.0	218
1	5.0	12.0	172
2	6.5	12.0	123

4.1.6 Defining solar cell area

After the deposition of AZO layer, the cell active area is defined out of a large area of the CZTS solar cell stack by removing the layers on top of the Mo outside the cell area. Individual cells with an area of 0.05 - 0.5 cm^2 were scribed by the help of a razor blade (Figure 4.11.). No anti-reflection coatings were deposited to cells in this thesis, whereas a relative gain of 4-8 % in current can be achieved by using anti-reflection coatings (Contreras et al., 1996). Finally, the cells were directly contacted with silver epoxy via the window layer for electronic characterization. These contacts extract the photo-generated electrons from the cell and deliver them to the external load.

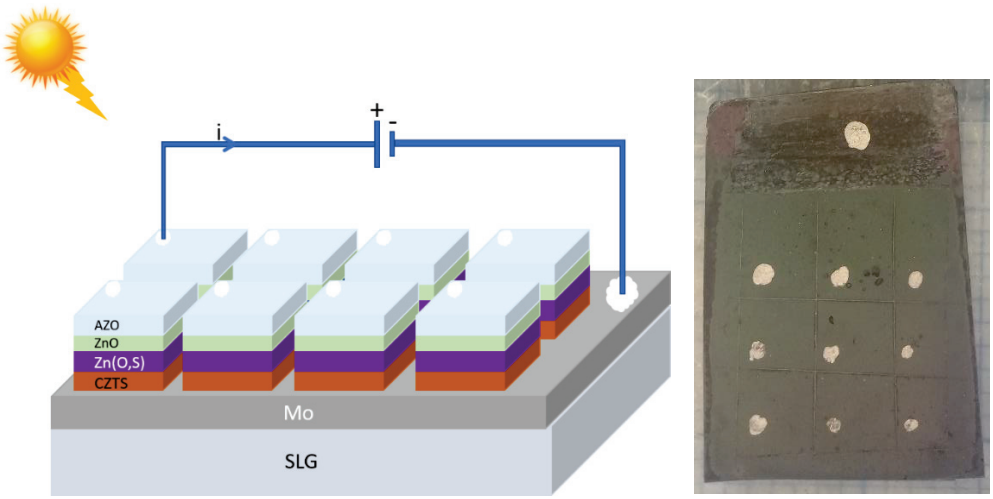

Figure 4.11. Schematic of device structure and image of the fabricated CZTS solar cell.

4.2. Characterization Techniques

In the spirit of understanding the properties of CZTS solar cell it is essential to characterize both devices and materials used in the device fabrication. The basic methods used in this thesis for the characterization of materials as well as devices are briefly presented in the following section.

4.2.1. Profilometry

A profilometer is a tool that uses a stylus to detect the surface. As the stylus is moved, it measures small surface variations in vertical movements as a function of position. A Veeco DEKTAK 150 profilometer was used to determine the thickness of all thin films used in the device fabrication CZTS solar cells. It is capable of measuring thickness ranging in height from 131 microns to less than 100 Angstroms on a wide variety of substrate surfaces.

4.2.2. Scanning Electron Microscopy (SEM)

Scanning Electron Microscopy (SEM) is a powerful technique to image the morphology of thin films and the interfaces between thin film layers. The operation principle of SEM is similar to optical microscope, but the instead of using light, focused beam of electrons are used to produce images of a sample. Usage of electrons offers an advantage over optical microscopes: since electron wavelength is much smaller than photon wavelength, much larger magnifications (> 100 000 X) are possible. A topography image of the sample surface is produced by scanning the sample with the focused electron beam while the number of secondary and/or back scattered electrons emitted from the sample is detected.

In the present work, FEI-QuantaFEG 250 SEM with operating voltage of 20 kV was employed to characterize CZTS absorber and to have an idea about the morphology of the material, average grain size and the presence of undesired phases leaning on its surface.

4.2.3. Energy Dispersive X-Ray Spectroscopy (EDS)

Energy Dispersive X-Ray Spectroscopy (EDS) analyses enables to investigate the atomic composition of the sample. The working principle of the EDS is based on the bombardment of the sample with focused beam of electrons and excitation of an electron in an inner shell, ejecting it from the shell while creating an electron hole. These vacant shell is then filled up by an electron from an outer, higher-energy shell. specific energies in the form of an X-ray may be released due to energy difference between the higher-energy shell and the lower energy shell. energy-dispersive spectrometer measures the number and energy of the X-rays emitted from a sample. Consequently, elemental composition of the sample can be determined since the energies of the X-rays are characteristics of energy difference between the higher-energy shell and the lower energy shell and of the atomic structure of the emitting element.

EDS analysis of the CZTS films was performed by FEI-QuantaFEG 250 SEM equipped with Oxford X-act EDS to have an idea about the stoichiometry of the films.

4.2.4. X-Ray Diffraction (XRD)

X-Ray Diffraction (XRD) is a powerful technique to identify atomic and molecular structure of a crystal. in a crystalline material, a beam of incident X-rays diffract into many specific directions, and constructive interference occurs when Bragg's Law is satisfied (Bragg & Bragg, 1913). Atomic and molecular structure of the material along with unit cell dimensions can be identified by measuring the angles and intensities of these diffracted beams.

For all thin films used in the device fabrication, XRD was carried out to obtain information about crystal structures of the films. The XRD was operated in the Bragg-Brentano focusing geometry on a Phillips X'Pert Pro X-Ray diffractometry, with Cu Kα radiation (λ=1.5406 Å). XRD patterns were recorded from 2θ = 20-80° with step size of 0.016° and a time step of 31 second for all samples.

4.2.5. Raman Spectroscopy

Raman spectroscopy is an effective spectroscopic technique to investigate vibrational modes of materials. Its operational principle relies on Raman scattering (inelastic scattering) of monochromatic light, generally from a laser source in the visible (390-700 nm), near infrared (700nm-1400nm) or near ultraviolet (300-400nm) range. The frequency of the monochromatic light absorbed by the material changes after its interaction with the sample. The energy difference between the incident photons and those reemitted by the sample corresponds to the vibrational energy levels of the molecule diffusing. The analysis of the shift of the spectral lines can provide information about the chemical composition, molecular structure, and intermolecular interactions of the sample.

Raman studies were performed, using High-resolution Raman spectroscopy (Princeton Instruments, Acton SP2750 0.750 mm Imaging Triple Grating Monochrometer) in the back-scattering mode with spectral resolution of 1 cm^{-1} at room temperature. A wavelength of 514.5 nm Ion-Ar^{+} and 633 nm HeNe laser were used with a 25 mW power for CZTS thin films. For all other thin films used in the device fabrication, wavelength of 488 nm Ion-Ar^{+} laser was used. Measurements were performed with 600 grating and 100X objective. The spot size was > 30 μm in diameter. The probing depth of the Raman spectroscopy is determined by the absorption coefficient (α) of the material for the respective wavelength of the excitation source. In the case of backscattering con figuration, it is roughly given by $d \approx 1/(2\alpha)$. This results in penetration depth of scattered light of around 100 nm for CZTS with an absorption coefficient $>10^{4}$ cm^{-1}.

4.2.6. X-ray Photoelectron Spectroscopy (XPS)

XPS is an analysis technique based on the photoelectric effect. Incoming X-Rays excite the surface of a sample, causing photoelectrons to be emitted from the sample surface. Then, the binding energy calculated from an electron energy analyzer is used to evaluate the kinetic energy and the number of photoelectrons emitted. Binding energy and intensity of a photoelectron peak enable to determine the element identity, chemical state and amount of a detected element.

The XPS spectra of Zn(O,S) films were analyzed so as to identify the surface composition distribution and chemical bonding states of the constituent elements.

Measurements were performed on SPECS Phoibos 150 3D-DLD system with using Mg Kα radiation (hν=1254 eV) operated at 200 W and 1.5 kV. The analyzer pass energy and the step size were 30 eV and 0.1 eV, respectively. The high-resolution spectra of C1s, S2p Zn2p and O1s valence regions were measured in detail and calibrated with respect to C1s peak at 284.6 eV (Yazici et al., 2015). In order to identify the atomic multivalency of each element in Zn(O,S), high resolution spectra were deconvoluted.

In addition, to calculation the atomic concentration of constituent elements, the area of peaks and sensitivity factors of each elements provided by the CASAXPS software were used. Before the de-convolution, the Shirley type background was subtracted to the high-resolution spectra of each elements and Gaussian-Lorentzian product GL(p) function was used by considering the theoretical assumptions. The Zn and S2p peaks occur as doublets of 2p3/2, 2p1/2. The 2p spectra was fitted using I(2p3/2):I(2p1/2) intensity ratio of 2:1 (Yazici et al., 2015). During the fitting process, spin-orbital splitting values and FWHM value of each couple elements were constrained. The constrains on the peak positions were not applied.

Zn 2p spectra were fitted using GL(68) line shape and consist of 2p1/2 and 2p3/2 with a doublet separation of 23.1 eV. The S2p spectra was observed in the range of 160 to 164 eV which assign to the S in metal sulfides. All S2p valence regions were fitted using GL(75) line shapes. The peak fitting result of all S 2p spectra showed 2p3/2 and 2p1/2 doublets with spin-orbit splitting value at around 1.2 eV. For the peak fitting of O1s valence region, GL(30) line shape was used.

4.2.7. Spectrophotometry

Spectrophotometry is commonly used for the quantitative measurements of the reflection or transmission properties of a materials as a function of wavelength. Optical properties of all thin films used in the device fabrication were investigated by transmittance measurements in the 200–2600 nm wavelength range, using a PerkinElmer Lambda 950 UV/VIS/NIR spectrophotometer.

4.2.8. Electrical Characterization of the thin films

In this work, electrical characteristics of AZO thin films were investigated to determine sheet resistance of the films by four-point probe technique using Keithley 2224 source meter.

4.2.9. Device Characterization

The performance of CZTS thin-film solar cell devices, such as V_{oc}, I_{sc}, FF and cell conversion efficiency, was analyzed by current voltage (I-V) characterization. The current-voltage measurement was performed by an IV sweep, which is to scan an applied voltage across the solar cell while the voltage and current at the cell terminals are recorded.

In this thesis, homemade solar simulator was used (Figure 4.12.). Some of the devices was tested in Middle East Technical University Laboratory (METU) using Newport 91192 model 300 W solar simulator under standard test conditions (25 °C, 1000 W/m^2, AM 1.5G illumination) to test the accuracy of our measurements. The data of our in-house measurements have been verified to be very close to those measured at METU, differences in cell efficiencies were less than 0.5 %.

Figure 4.12. shows I-V experimental setup interfaced with a computer. To obtain the I-V curve of a CZTS cell a function generator was used to generate the sweeping voltage. Amplitude and frequency of saw wave was set at 2-2.5 Vp-p and 0.005 Hz, respectively. One probe from the function generator was placed on a resistor with 10 Ω resistance while the other probe was placed on the CZTS cell. Two Keithley 2182A nanovoltmeter are interfaced with a computer and controlled by Labview program that contains serial instrument control, data analysis and data storage. Probes of one of the nanovoltmeter were connected to the front contact and the back contact of the CZTS solar cell to measure the voltage across the device, while the probes of other nanovoltmeter were placed on the ends of the resistor to measure the current flowing out of the device. This four-probe arrangement helps to eliminate the contact resistance between the probe and contact interfaces. We used a halogen lamp as a light source, calibrated to provide the same short circuit current as that obtained from I-V measurements performed at METU. The intensity of input light was 1 kW/m^2 and the devices were measured at room

temperature, around 25 °C. Graphical programming tool of Labview program provides to see I-V curve, in which the current of the solar cell is plotted on y-axis against the applied voltage on x-axis. Light I-V measurements were used to determine the values of V_{oc}, I_{sc}, V_m, I_m, FF and cell conversion efficiency, while dark I-V measurements are employed to determine loss parameters of solar cells such as R_s and R_{sh}. Figure 4.13. shows dark I-V and light I-V curve showing how the information about the device was determined.

Figure 4.12. I-V experimental setup interfaced with a computer.

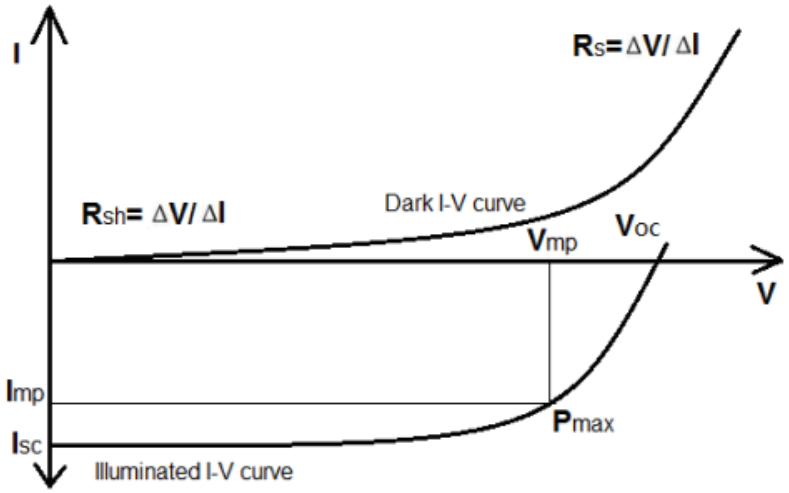

Figure 4.13. Dark I-V and light I-V curve showing how the information about the device was determined.

CHAPTER 5

RESULTS AND DISCUSION

5.1. AZO Thin Films

For AZO thin films, achieving low resistivity and high transmittance simultaneously at room temperature is still challenging. A high deposition temperature above 300 °C is necessary to get a desired TCO property in most of the fabrication methods since the higher temperature provides an improvement in the crystallinity of the thin films. However, higher temperature generates many defect states due to increased interfacial diffusion and cause high charge carrier recombination rate. Therefore, a room temperature deposition process is required to avoid inter-diffusion between the layers of a solar cell. Here, we demonstrate that the crystallinity and resistivity of the AZO films fabricated at room temperature can be improved by off-center deposition and rotating the sample holder during sputtering. We investigate the effect of rotation speed and the location of the samples on the sample holder on the properties of the AZO films deposited on SLG. For this aim, SLGs are located onto the rotating sample holder both above the target (position 0) and in off-center configurations (position 1 and 2) (see Figure 5.1.).

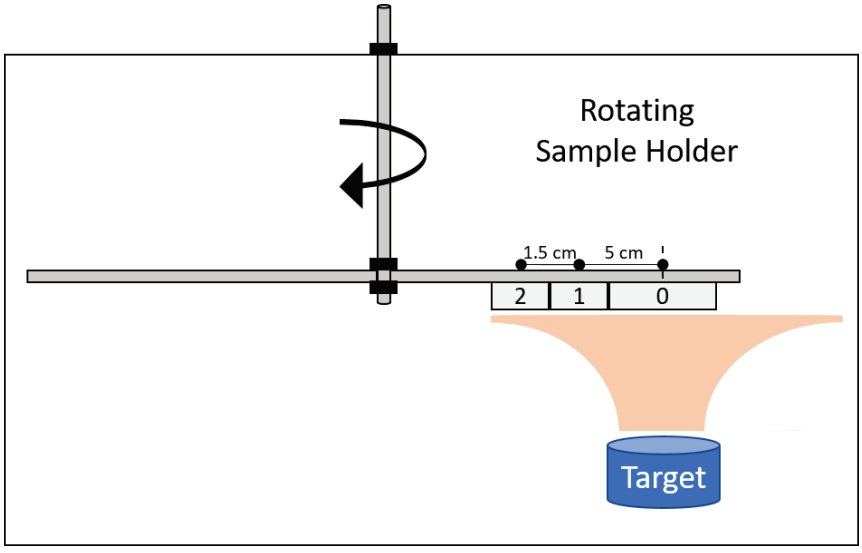

Figure 5.1. Sample positions on the rotating sample holder.

5.1.1 XRD Analyses

Crystallinity is known to play an important role in determining the optical and electrical properties of a thin film. Figure 5.2. shows the X-ray diffraction patterns of AZO films deposited with different rotating speeds at different distances from the target axis. At all rotational speeds, diffraction peak of AZO thin films appears at approximately 34.3 degrees which belongs to (002) reflection of the hexagonal wurzite structure. This shows the formation of highly oriented grains along the c-axis due to self-texturing. We observed lower 2θ values for the AZO films with respect to bulk ZnO which has a diffraction line at 34.51. While there is small shift in 2θ values for the AZO films placed in positions 1 and 2, for the AZO films placed on the 0 position the crystallinity deteriorates and 2θ shifts to more lower values.

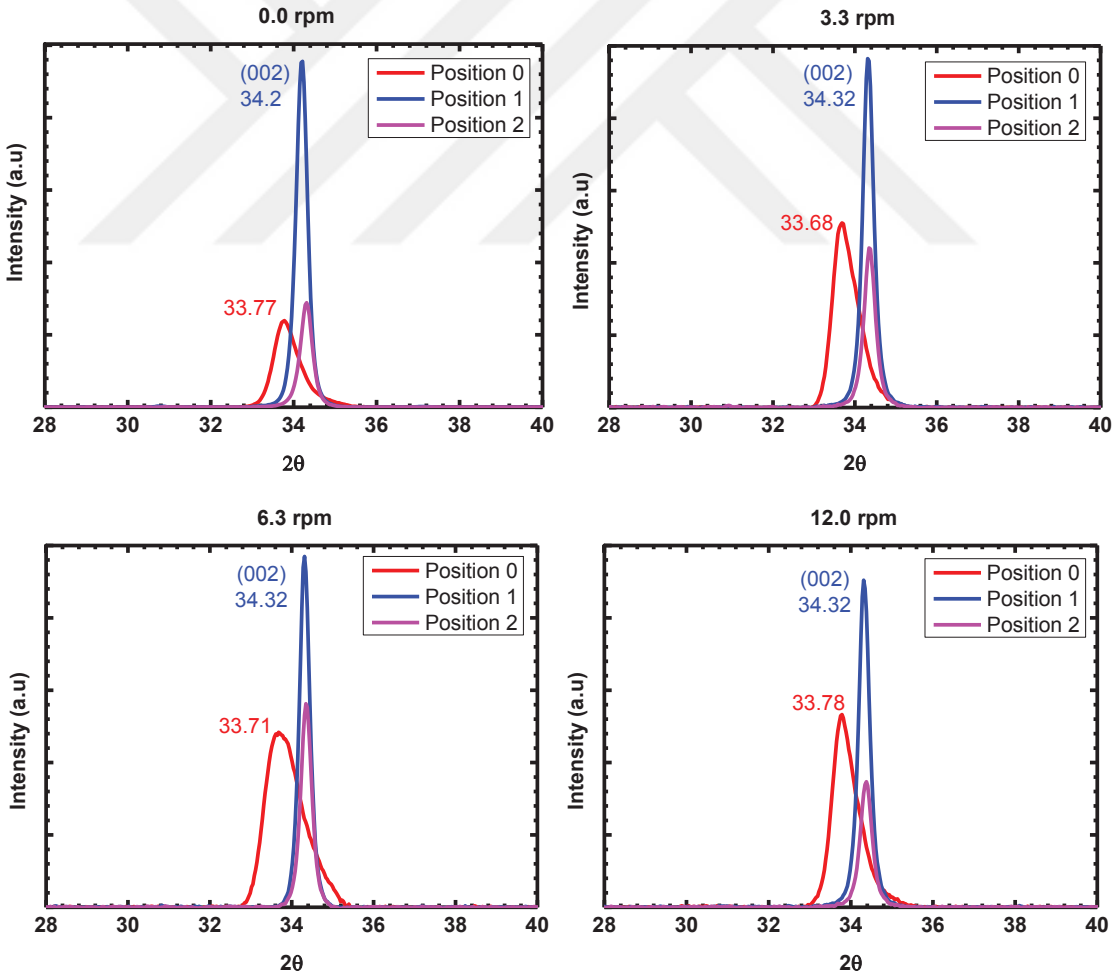

Figure 5.2. X-ray diffraction patterns of AZO films deposited with different rotating speeds at different distances from the target axis.

It is known that the XRD peak of AZO thin films shift towards a lower or higher 2θ value with respect to bulk ZnO (Nagiri, Yambem, Lin, Burn, & Meredith, 2015). Al is an effective donor, it substitutes at the Zn sites or creates oxygen vacancies after sitting as an interstitial atom. When Al is incorporated into ZnO lattice, AZO lattice is distorted due to the difference in ion radius between Al^{3+} (0.039 nm) and Zn^{2+} (0.06 nm) (Nguyen et al., 2011). If the Al^{3+} ions substitute at the Zn^{2+} sites, AZO crystal lattice constants are reduced. This leads to smaller interplanar spacing (d_s) and 2θ shifts to higher values according to Bragg's law. Moreover, Al can easily interstitial solubilized in ZnO octahedral site since the ratio of the atomic radius of Al to the atomic radius of ZnO ((r_{Al}/r_{ZnO}) = 1.18 Å /1.625 Å = 0.726) is lower than the maximum value for interstitial solubilization (0.732) (Nguyen et al., 2011). Since the AZO films grown at room temperature do not have sufficient activation energy for the Al to substitute at the Zn sites, many of Al^{3+} ions cations sit in the films as an interstitial ion which leads to higher interplanar spacing (Nguyen et al., 2011; Wang, Xu, Ren, & Yang, 2008). The variation of the 2θ values and interplanar spacing derived from the (002) peak position can be seen in Table 5. 1. For all films d_s values are larger than that of bulk ZnO which is equal to 0.2603 nm which indicates that all the films exhibit compressive stresses and the stress is caused predominantly by the interstitial Al^{3+}. Moreover, as the distance between the substrate and the target axis increased, shift in 2θ values decreases.

When we look at the magnified view of (002) peak for the films in position 0 (Figure 5.3.), it can be clearly seen that distortion of the lattice parameters under compressive stress leads to a broad single peak in the XRD spectra. In order to get more insight about the structure of the films, a peak deconvolution of the XRD patterns was performed (Figure 5.3.). From these results, we observed peak overlapping of the (002) peak of AZO and (004) peak of the Al_2O_3 (JCPDF#00-052-0803) at 2θ values 33.75 ° and 34.2°, respectively. The oxygen atoms at the surface of the AZO target is ionized and accelerate towards the substrate during the sputtering. These negative oxygen ions are neutralized during their transits. However, they can reach the substrate with sufficient energy to be implanted. When the sample placed away from the target, sputtered particles and argon ions collide frequently, their energy is reduced while traveling to the substrate. Therefore, direct bombardment of high energetic negative ions is significantly reduced with the off-center configuration. When the sample placed in front of the target, the energetic sputtered particles arrive at the substrate with high kinetic energy since sputtered particles and argon ions collide less frequently (Nguyen et al., 2011).

Consequently, direct bombardment of high energetic O atoms on the surface may combine with Al atoms to form aluminum oxides and limit the doping effect (Horwat & Billard, 2007). Non-conducting Al_2O_3 clusters in the films can cause disordered structure and produce defects (Manouni et al., 2006). Formation of these defects and phases leads to more compressive stress in the film (Horwat & Billard, 2007). Moreover, bombardment by negative ions can lead to re-sputtering of Zn atoms since the sputtering threshold energy (E_{thr}) of Zn atoms is very low during the deposition (Cai et al., 2010). We think that when the sample placed in front of the of the target, the energetic negative ions with high kinetic energy can lead to more re-sputtering of Zn atoms, thus providing an increase of the Al/Zn and oxygen/metal ratio (Cai et al., 2010). Therefore, increasing amount of Al can enhance Al_i defects and trigger the formation of the Al_2O_3 which has lower formation energy than that of ZnO (Cai et al., 2010). The amount of re-sputtered Zn atoms decreases with the off-center configuration since the energy of negative ions is reduced. This leads to a decrease of the Al/Zn and oxygen/metal ratio.

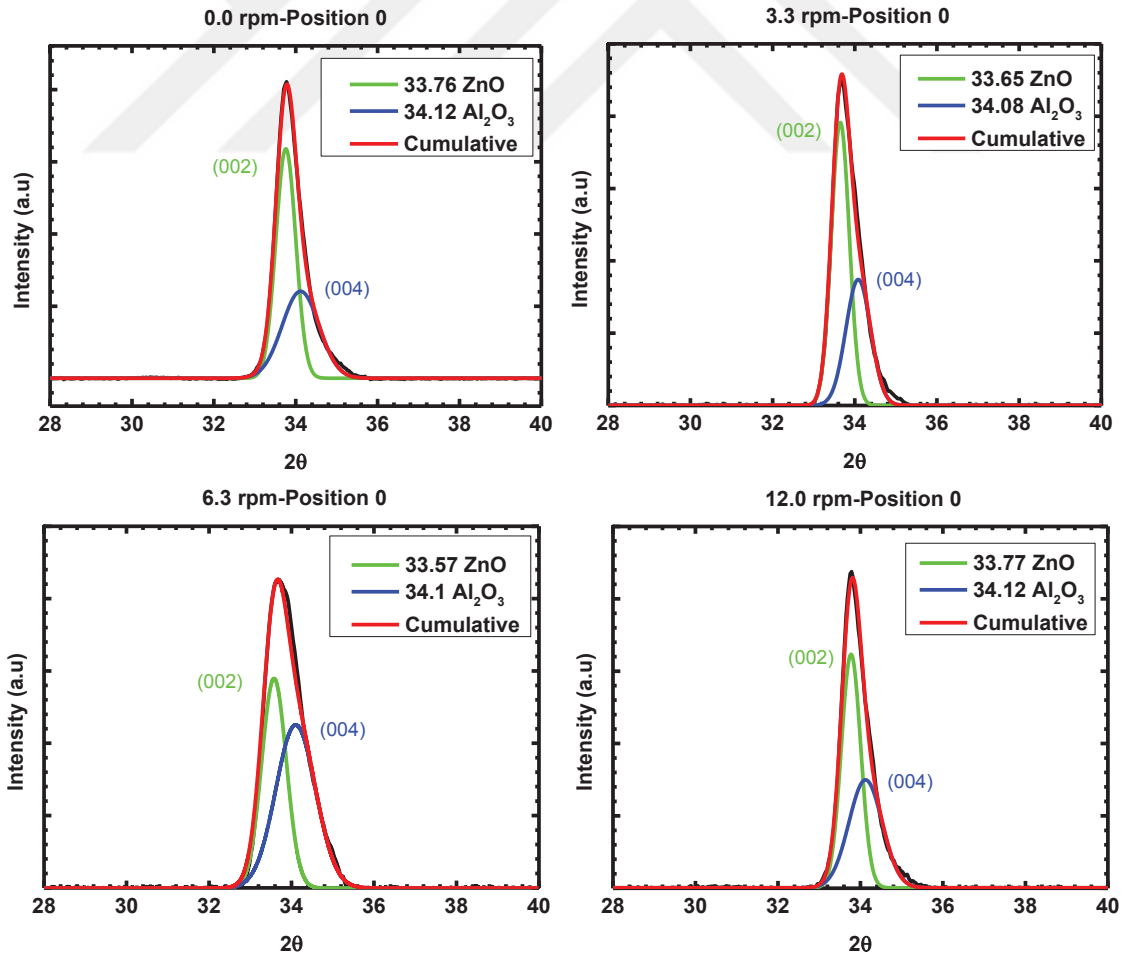

Figure 5.3. The magnified view of (002) peak for the films in position 0.

The total residual stress in the thin films consist of the intrinsic stress induced by the doping and defects during the fabrication process and, the extrinsic stress induced by different lattice constants and thermal expansion coefficients of the thin film and its substrate (Kim, Yim, Son, & Leem, 2012). Since no heat treatment applied to the films, the differences in the residual stress of the AZO films is mainly intrinsic stress resulting from growth conditions.

The stress in the films can be estimated using the following formula, which is valid for a hexagonal lattice

$$\sigma_{film}^{XRD} = \frac{2c_{13}^2 - c_{33}(c_{11}+c_{12})}{2c_{13}} * \frac{c_{film}-c_{bulk}}{c_{bulk}} \quad (5.\ 1)$$

where the c_{ij} is the elastic stiffness constant of single crystalline ZnO (c_{11}=208.8, c_{33}=213.8, c_{12}=119.7, c_{13} =104.2 GPa) (Cebulla, Wendt, & Ellmer, 1998). c_{film} and c_{bulk} are the lattice constants of the AZO films and bulk ZnO thin films, respectively. This yields the numerical relation between in-plane stress and out-plane strain, σ_{film}=223*ε (GPa). The strains in the films were derived using the relation $((d_s-d_0)/d_0)$, where d_0 is the inter-planar spacing of bulk ZnO. The estimated strain and stress values of the AZO films shown in Table 5.1. Positive values of strains indicate the tensile strain and negative values of stresses indicate the compressive stress in our AZO films. Figure 5.4. shows how the position of the substrate and rotation speeds affect the stress in the films. According to this figure, stress in the films decreases when the substrate position with respect to the target axis increases. Moreover, we observed small reduction of the stress in the films with increasing rotation speed. As given in Table 5.1., deposition rate for non-rotating samples is much larger than the deposition rate for rotating samples. According to deposition rates, when the substrate is rotated, the duration of substrate residence in front of the target decreases. Therefore, sputtered particles and argon ions collide frequently with high rotation speed, energy of sputtered species is reduced while traveling to the substrate. Non-rotating samples more exposed to direct bombardment of high energetic negative ions due to high energy of sputtered species. From these findings, it can be concluded that bombardment of high energetic negative ions on the surface and so stress in the films can be significantly reduced by off-center deposition and rotating the sample holder during deposition.

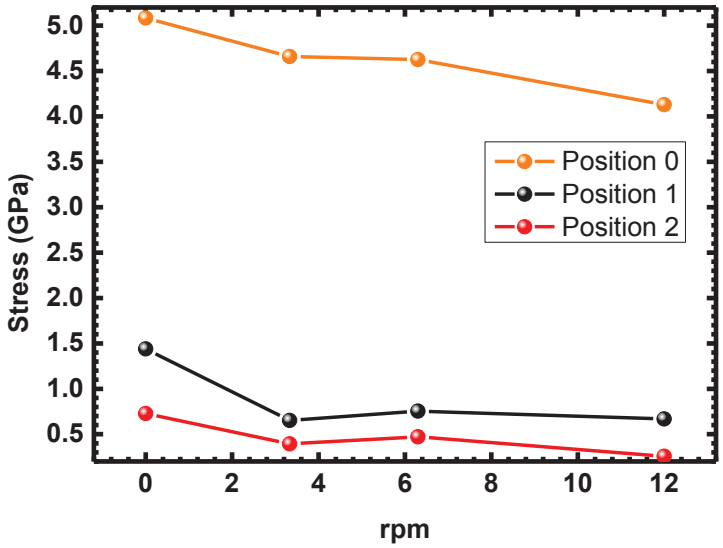

Figure 5.4. Effect of position of the substrate and rotation speed on the stress in the films.

Table 5.1. Variation of the thickness, deposition rate, (002) peak positions, d spacing, FWHM, c lattice constant, Strain and Stress of AZO thin films with different positions on sample holder and rotation speed.

Rotation Speed (rpm)	Sample Position	Thickness (nm)	Deposition Rate (nm/min)	2θ	d spacing (Å)	FWHM	c Lattice Constant (nm)	Strain	Stress (GPa)
0.0	0	600	6.67	33.76	2.66	0.69	5.37	0.0191	4.27
0.0	1	450	5.00	34.20	2.62	0.33	5.24	0.0065	1.44
0.0	2	250	2.78	34.31	2.61	0.34	5.22	0.0033	0.73
3.3	0	230	2.56	33.70	2.66	0.71	5.31	0.0209	4.66
3.3	1	182	2.02	34.32	2.61	0.31	5.22	0.0029	0.65
3.3	2	142	1.58	34.36	2.61	0.33	5.22	0.0018	0.39
6.3	0	190	1.58	33.71	2.66	1.04	5.31	0.0207	4.63
6.3	1	165	1.38	34.31	2.61	0.30	5.22	0.0034	0.75
6.3	2	135	1.13	34.36	2.61	0.31	5.22	0.00210	0.47
12.0	0	218	2.42	33.78	2.65	0.70	5.30	0.0185	4.13
12.0	1	172	1.91	34.32	2.61	0.31	5.22	0.0030	0.67
12.0	2	123	1.37	34.38	2.61	0.33	5.21	0.0012	0.26

5.1.2 Raman Analyses

Since Raman scattering by the phonons is determined by the electrons that remote the scatter phenomenon, Raman spectra contain information not only about phonons but also about electrons and electron-phonon interactions (Russo, Ghidelli, Gondoni, Casari, & Bassi, 2014). Therefore, Raman measurements were performed to better understand

the correlation between the structural and electrical properties of the samples. The Raman modes of AZO can be understood by considering the crystal symmetry of the wurtzite structure of ZnO.

The ZnO compound crystallizes in the in the wurtzite structure with C_{6v} symmetry. Wurtzite structure implies a basic unit of 4 atoms in the ZnO unit cell. Since N different types of atoms in the primitive cell results in 3N vibrational modes, 4 atoms in the ZnO unit cell yields twelve phonons at the center of the Brillouin zone with N=3 acoustic phonons and 3N-3=9 optical phonons (3xLO, 6xTO). Based on group theory, the optical modes at the at the Γ point is represented as fallows (Damen, Porto, & Tell, 1966);

$$\Gamma = A_1 + 2B_1 + E_1 + 2E_2 \tag{5.1}$$

Among these modes, the A_1, E_1 and E_2 modes are Raman active. The B_1 modes are IR and Raman inactive (silent modes). For the lattice vibrations with E_2 symmetry, the atoms move perpendicular to the c-axis. The low-frequency E_2 (low) mode at 99 cm^{-1} predominantly involves the vibration of the heavy Zn sublattice while the high-frequency E_2 (high) mode at 437 cm^{-1} involves the vibration of the lighter O sublattice. these two modes are defined as nonpolar modes since the neighboring ions move opposite to each other and the displacements of the ions results in no net induced polarization in each sublattice. On the contrary, the oxygen-dominated A_1 and E_1 modes are polar. The atoms move parallel to the c-axis for the lattice vibrations with A_1 symmetry and perpendicular to the c-axis for the lattice vibrations with E_1 symmetry in such a way that the displacement of the Zn sublattice relative to the oxygen sublattice results in a net oscillating polarization. The polar A_1 and E_1 modes are each split into LO and TO modes with different frequencies due to the macroscopic electric fields of the LO phonons. Because of this LO-TO splitting and the small frequency difference between the A_1 and the E_1 modes is that mode mixing can only occur between A_1 (LO) and E_1 (LO) or between A_1 (TO) and E_1 (TO) (Bergman et al., 1999). If the incident light is exactly normal to the surface, only A_1 (LO) and E_2 modes are observed in highly oriented ZnO films, and the other modes do not appear since they are forbidden according to the Raman selection rules. The A_1 (LO) and the E_1 (LO) modes have different polarization selection rules in backscattering geometry, while A_1 (LO) mode is allowed from the c face, the E_1 (LO) mode is forbidden from both the a and the c faces. In disordered materials, the

polarization selection rules are relaxed and the two modes are often merged in a single band, called the LO band. Table 5.2. gives reference values of six detectable peaks (Russo et al., 2014).

Table 5.2. Raman shifts for wurtzite ZnO.
(Source: Russo et al., 2014)

Symmetry	**Raman shifts (cm^{-1})**
A_1– TO	378 – 380
E_1 – TO	407 – 413
A_1 – LO	574 – 579
E_1 – LO	583 – 591
E_2 – low	98 – 102
E_2 – high	437 – 444

Figure 5.5. shows the Raman spectra of AZO films excited at 488 nm. Raman spectra consist of two Raman active modes around 446 and 582 cm^{-1}. The Raman modes at 800 cm^{-1} is due to the SLG substrate. The observed Raman modes are assigned as follows. The peak at 446 cm^{-1} is the E_2 (High) mode of ZnO associated with the wurtzite structure and is related to vibration of only oxygen atoms (Özgür et al., 2005). It is worth noting that E_2 (High) mode shifts higher frequencies (blue shift) for all samples. E_2 (High) phonon frequency is affected by stresses in the wurtzite structure or laser induce heating (Alim, Fonoberov, Shamsa, & Balandin, 2005; Yahia, Znaidi, Kanaev, & Petitet, 2008). The blue shift in the E_2 (High) is attributed to compressive stress, whereas the red shift in the E_2 (High) is attributed to tensile stress. However, the peak position of the E_2 (high) mode remains the same for all AZO films even for the samples in position 0. Thus, we attributed observed blue shift to local heating induced by UV laser. The vibration line around 582 cm^{-1} corresponds to the E_1 (LO) mode of ZnO, which is very sensitive to the oxygen deficiency, interstitial Zn and free carrier (Srinatha et al., 2016; Xu, Lau, Chen, Chen, & Tay, 2001; Zeng, Low, Ren, Liew, & Lu, 2002). Strong coupling of free carrier with E_1 (LO) mode would cause red shift (Zeng et al., 2002). We observed that position of the E_1 (LO) mode strongly depends on position of the sample and rotation speed as it can be seen from Table 5.3. For distant samples, this peak shift to lower values regardless of rotation speed and as the distance between substrate and target axis increased, amount of shift increases. Also, as it can be seen when the substrate is rotated during deposition, amount of shift is higher with respect to non-rotating substrates. Increase in red shift of

the E_1 (LO) vibration line indicates the enhancement in oxygen vacancies in our samples as the distance between substrate and target axis is increased and/or substrate is rotated. We may also attribute this shift to increasing carrier concentration of the films since the sheet resistance of AZO thin films fabricated at room temperature strongly related to the amount of oxygen vacancies (Xu et al., 2001). The oxygen vacancies create maximum two free electrons per vacancy to the donor level through ionization, leading to an increase in conductivity. A quantitative comparison of the peak intensities may not be meaningful due to different thickness of the films.

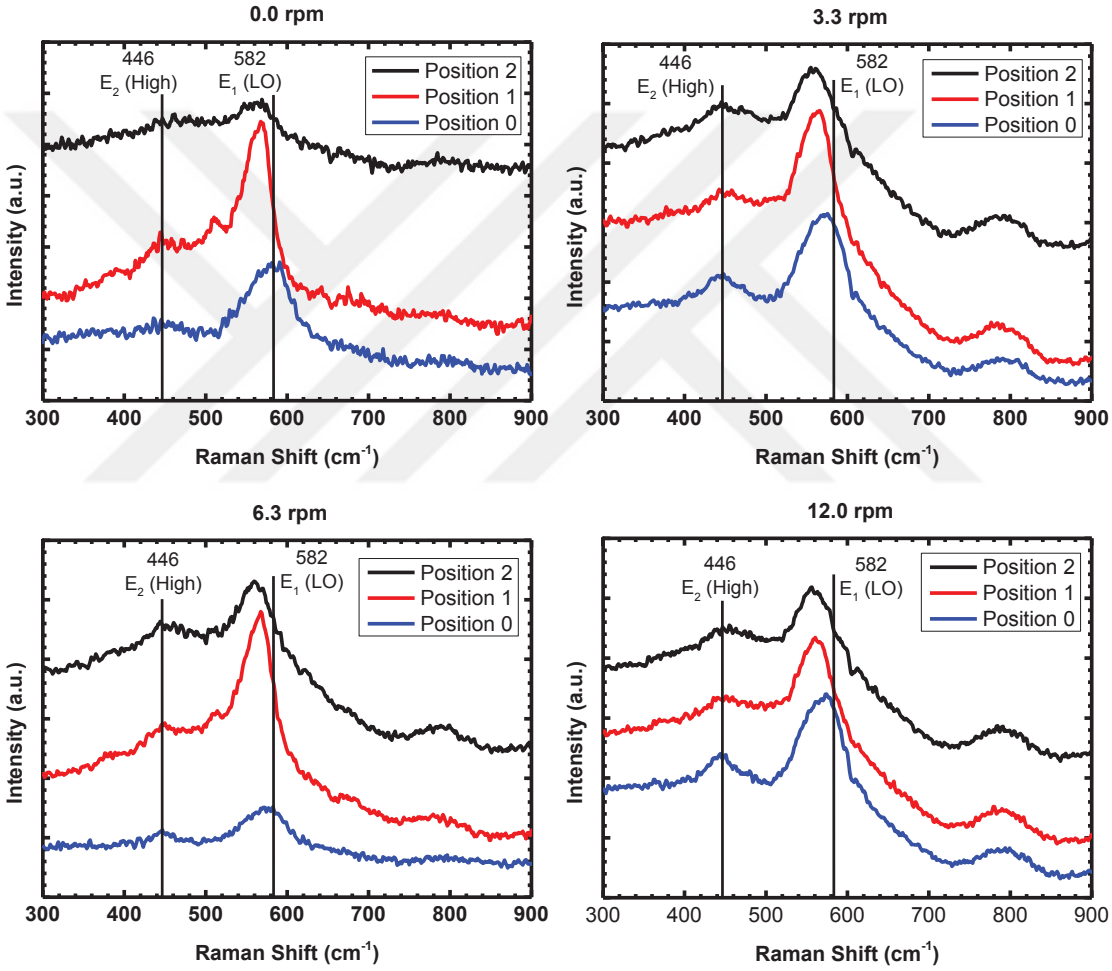

Figure 5.5. Raman spectra of AZO films deposited at different rpms.

Table 5.3. List of E_1 (LO) peak position (cm^{-1}) wrt rpm and sample position

	Sample Position	**E_1 (LO) peak position (cm^{-1})**
0.0 rpm	0	582
0.0 rpm	1	568
0.0 rpm	2	562
3.3 rpm	0	573
3.3 rpm	1	565
3.3 rpm	2	558
6.3 rpm	0	575
6.3 rpm	1	568
6.3 rpm	2	560
12.0 rpm	0	570
12.0 rpm	1	561
12.0 rpm	2	558

5.1.3 Transmission Analysis

Figure 5.6. illustrates the transmittance spectra of our AZO films. As can be seen, the average transmittance of all AZO films in the visible region (400–800 nm range) exceeds 85 % which is important for the applications in the field of solar cell. The absorption edge of the samples (sharp decrease in transmittivity) was observed in the range from 300 to 400 nm. We observed that absorption edge shifts to shorter wave lengths as distance between substrate and target axis increased. This blue shift can be attributed to an increase in the band gap energy resulting from the Burstein-Moss effect (Burstein, 1954; Moss, 1954) which is related to the carrier concentration. That is, with increasing distance between substrate and target axis, the optical band gap of the films grows due to increased carrier concentration and causes the absorption edge to shift to short wave lengths. Moreover, we observed that transmission of the samples located in off-center configurations (position 1 and 2) is lower than the samples located above the target (position 0) in infrared region. The concentration of free carriers is important for the optical transmission of AZO films in the near infrared region. High free carrier concentration causes high reflection or lower transmission of the infrared region (Koseoglu et al., 2015).

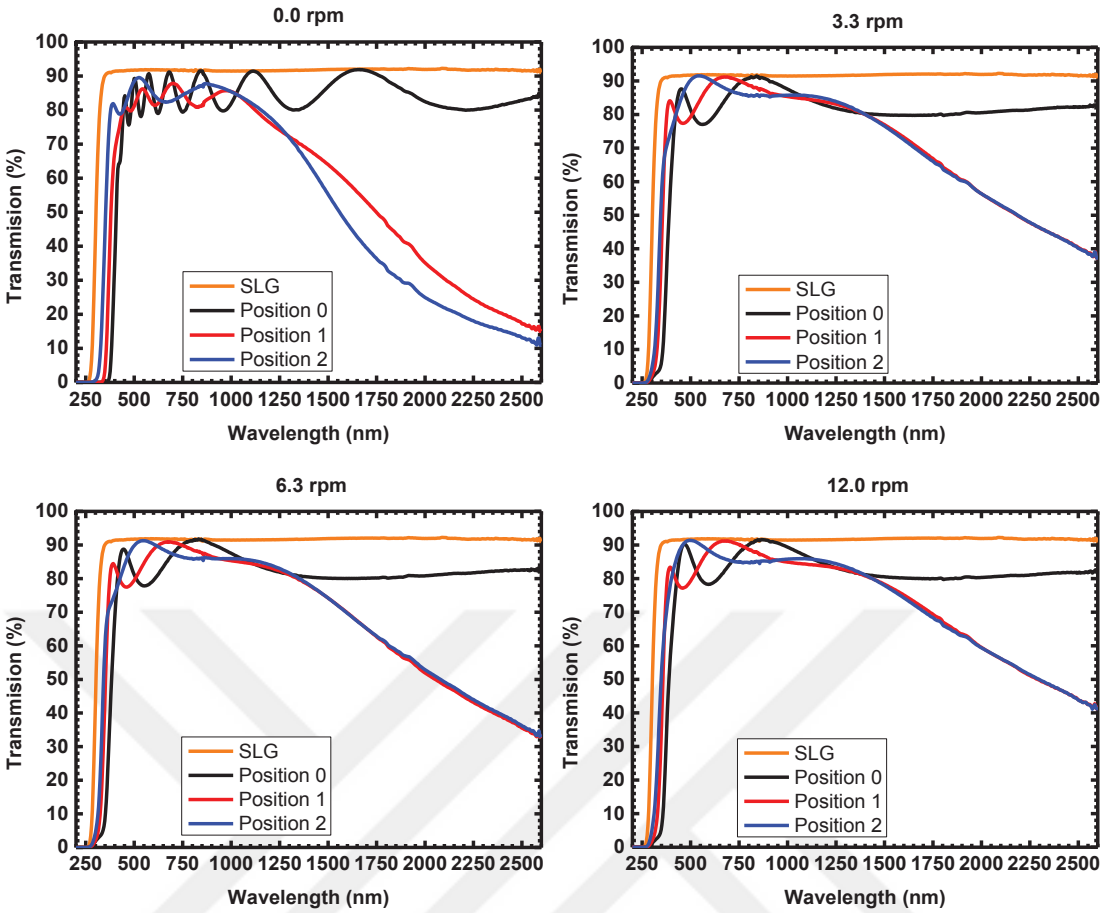

Figure 5.6. Transmittance spectra of AZO films deposited at different rpms.

Tauc method was used to calculate the energy gap of the samples to better understand the blue shift of the absorption edge. In the present study, the absorption coefficient, α^2 versus photon energy ($h\nu$) plot was used to estimate the bandgap energy of the AZO thin films (Figure 5.7.). Absorption was calculated by the following equation;

$$T - R = e^{-\alpha t} \tag{5.2}$$

where T and R denote the transmittance and reflectance, respectively, and t is the thickness of the film. The reflectance of the films was neglected due to its relatively low value (Koseoglu et al., 2015), and then the absorption coefficient was simplified as;

$$\alpha^2 = \frac{(InT)^2}{t^2} \tag{5.3}$$

Since aluminum doped zinc oxide has a direct transition, i.e. $\alpha h\nu = A(h\nu - E_g)^{1/2}$, the bandgaps of the films are deduced from the extrapolation of the linear plots of α^2 versus $h\nu$.

Figure 5.7. shows the α^2 vs photon energy graph of AZO films coated at different rpm and at different distances from the target axis. The change in the energy band gap of AZO films deposited at different rpm and at different distances from the target axis is clearly visible in Figure 5.8. We observed that the optical energy gap shifts towards higher energies for the samples deposited at larger distances from the target axis (in a position sequence 0–2) regardless of rotating speed. As mentioned before, increase in the energy band gap can be interpreted by the Burstein-Moss effect results from the Pauli Exclusion Principle. Al is an effective donor, it substitutes at the Zn sites or creates oxygen vacancies after sitting as an interstitial atom. Donor electrons due to Al or oxygen vacancies normally occupy the higher energy levels in the conduction band. As a result, the effective band gap (E_g) of an AZO film should be relatively higher when compared to the separation in energy between the top of the valence band and the unoccupied energy states in the conduction band of this direct band gap semiconductor. Consequently, band gap moves to higher energy. The widening in the band gap (Burstein–Moss shift) is dependent on the carrier concentration, n, according to $n^{2/3}$. The reason of the low band gap of the samples in position 0 is to have low carrier concentrations due to high compressive stress, as the stress relaxes for the samples in position 1 and 2 carrier concentrations and so band gap of the samples increases. Moreover, as the sample holder rotational speed increases band gap increases regardless of sample position indicating increase in carrier concentrations. On the other hand, it is further observed a small decrease in band gap occurs for high rotation speed (12.0 rpm). Such a red-shift of the optical band gap of AZO thin films has been explained in terms of relaxation of in-plane stress by Mohanty, et al. 2009 (Mohanty, Jo, Yeon, Choi, & Cho, 2009). According to their observation, the positive shift in E_g is well predicted by the BM effect for moderate values of carrier concentrations up to the Mott critical density. For higher carrier concentrations above the Mott critical density, BM effect is compensated by band gap shrinkage. Shallow level donor and shallow level acceptor impurities create energy levels in the band gap near the conduction band edge and the valence band edge, respectively. At high carrier concentrations, the density of states of these dopants increase and forms a continuum of

states like in the bands and the effective band gap of AZO is narrowed.

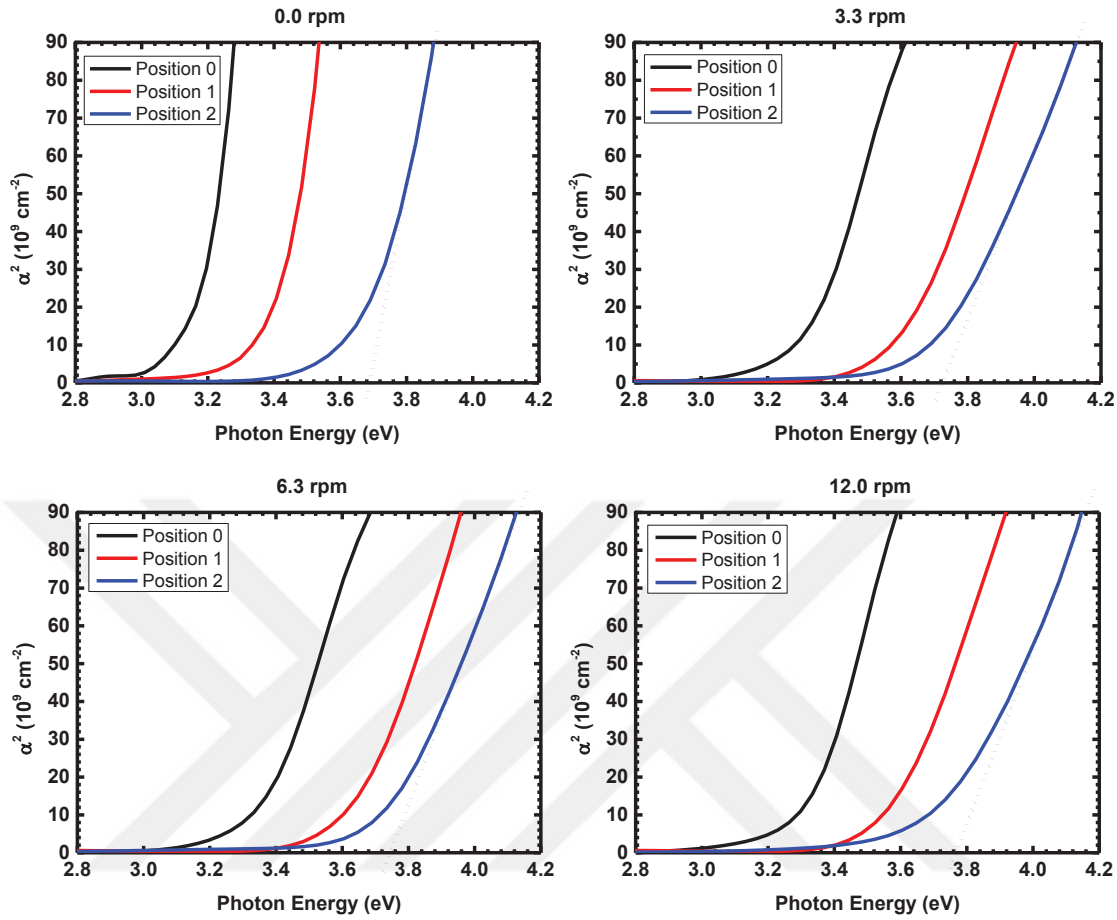

Figure 5.7. Tauc plots of AZO films deposited at different rpms.

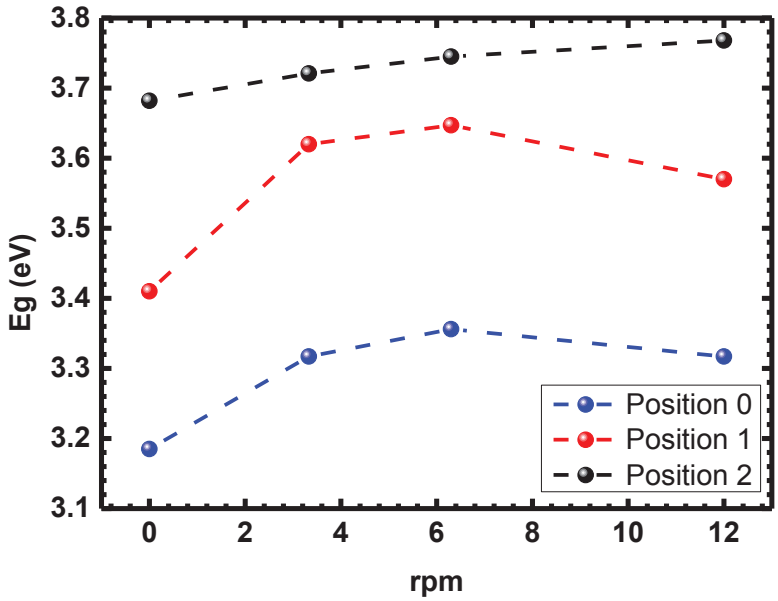

Figure 5.8. Energy gap values versus the sample holder rotation speed for AZO thin films at different positions on the sample holder.

From these observations, we conclude that carrier concentration of the films increases for off-center configurations and rotating samples during deposition since defects induced by the bombardment of high energetic negative ions is significantly reduced for these samples.

5.1.4 Electrical Properties of AZO Thin Films

The electrical property of AZO films is also an important factor for its performance in devices. Figure 5.9. shows the resistivity values measured by the four-point method versus the sample holder rotation speed for AZO thin films coated at positions 1 and 2. The films in position 0 have not been investigated because their resistivity values are very high. According to the XRD, strong enhancement of the resistivity for the substrate position facing the target may be due to excess of Al and O atoms which form non-conducting Al_2O_3 clusters in the films, acting as carrier traps rather than electron donors (Aktaruzzaman, Sharma, & Malhotra, 1991; Hu & Gordon, 1992). Raman spectroscopy and Transmission measurements also indicate the low carrier concentrations for the films in position 0. For the off-axis configurations, lower resistivity of AZO thin films can be correlated to the amount of donors, mainly oxygen vacancies and Al interstitial atoms which supply conduction electrons from donor sites. It has been observed that the resistivity of the films in position 2 are lower than those in position 1 regardless of rotation speed. This behavior attributed to higher carrier concentrations for the films in position 2, this attribution seems consistent with the XRD, Raman and Transmission data. In addition, we further observed that as the sample holder rotational speed increases resistivity decreases regardless of sample position. On the other hand, a small increase in resistance at 12.0 rpm may be attributed to likelihood of higher carrier concentration. The lowest resistivity value was found to be $2\ 10^{-3}$ Ω.cm for the AZO film in position 2 rotating at 6.3 rpm. As seen in Figure 5.8., the change observed in the band gap of the AZO films is in a perfect agreement with the charge carrier properties, as the band gap of the samples increases, resistivity values of the films decreases due to increment of carrier density in films.

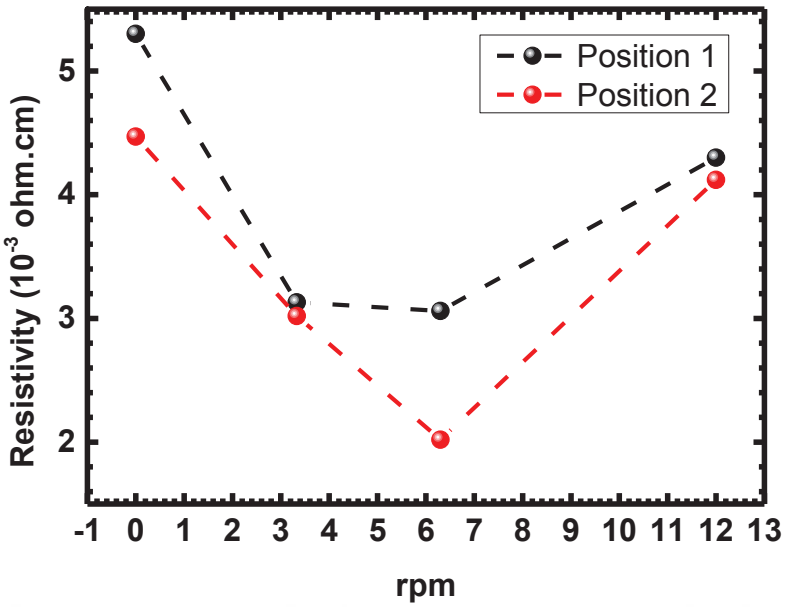

Figure 5.9. Resistivity values measured by the four-point method versus the sample holder rotation speed for AZO thin films coated at positions 1 and 2.

Table 5.4. Energy gap values measured by the four-point method versus the sample holder rotation speed for AZO thin films coated at positions 0, 1 and 2.

Rotation Speed (rpm)	Sample Position	Thickness (nm)	Rs (ohm/sq)	Resistivity (10^{-3} ohm.cm)	%T (av.)	%T (max.)	Eg (eV)
0.0	0	600	4.53E+06	272	80.718	91.19	3.185
0.0	1	450	117.78	5.30	82.054	87.85	3.410
0.0	2	250	58.89	4.47	84.326	89.56	3.682
3.3	0	230	9060	208	80.666	87.64	3.317
3.3	1	182	172.14	3.13	84.689	91.21	3.620
3.3	2	142	212.91	3.02	87.810	91.54	3.721
6.3	0	190	2944.5	55.90	82.028	88.76	3.356
6.3	1	165	185.73	3.06	84.647	91.00	3.647
6.3	2	135	149.5	2.02	87.598	91.28	3.745
12.0	0	218	9060	198	81.399	90.29	3.317
12.0	1	172	217.44	4.30	84.615	91.25	3.570
12.0	2	123	335.22	4.12	88.099	91.40	3.768

5.2. Zn(O,S) Thin Films

5.2.1. XRD Analysis

Figure 5.10. shows the normalized XRD patterns of the $ZnO_{1-x}S_x$ films with different sulfur concentrations ($0 \leq x \leq 1$). While the sulfur concentrations of $X_s = 0.8$, $X_s = 0.66$, $X_s = 0.57$ and $X_s = 0.53$ were determined by XPS, sulfur concentrations of $X_s =$

0.21 and X_s = 0.03 were estimated using Vegard's law as discussed later. High background noises in XRD patterns result from the small thicknesses of the films due to the higher x-ray irradiated length in comparison with the thicknesses of the films.

At room temperature, the thermal-equilibrium stable phases of ZnS and ZnO are the Zincblende (ZB) and Wurtzite (WZ) structures, respectively (Brafman & Mitra, 1968; Cheng et al., 2009; Özgür & Morkoç, 2007). At high temperatures, ZB ZnS transforms to WZ structure around 1023 °C (Yoo et al., 2001). This structure has nearly identical lattice spacing of the $(111)_{cub}$ and $(002)_{hex}$ planes, which make it difficult to distinguish diffraction peaks of ZB and WZ in the XRD spectra (He et al., 2012). We expect WZ structure for ZnO deposited at room temperature and ZB structure for ZnS deposited at 200 °C.

Peaks appear at 28.54 and 33.89 ° were attributed to cubic Zincblende ZnS (111) and hexagonal Wurtzite ZnO (002) planes, respectively. This shows the formation of highly oriented grains along the c-axis. With increasing S content in the films, (002) peak shift towards lower angles and approach pure ZnS. Considering that the ionic radius of S_2 (1.84 Å) is larger than that of O_2 (1.40 Å) (Mei et al., 2012) and that the calculated bond length of Zn–O bond (1.98 Å) is larger than that of Zn–S bond 2.34 Å (Persson et al., 2006), lattice constants of c-axis would increase when S substitutes for O sublattice of Zn(O,S), leading to decrease in diffraction angle of the (002) peak.

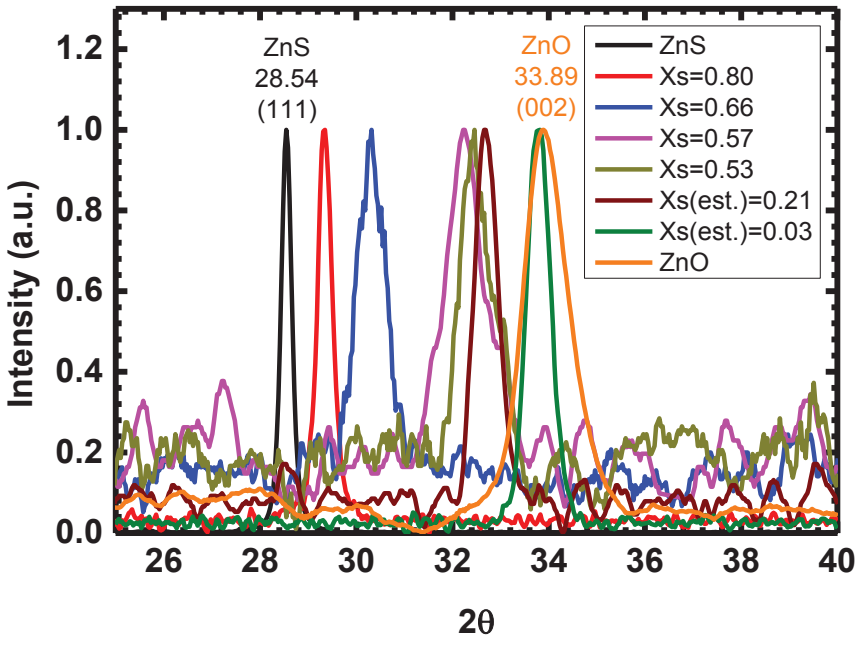

Figure 5.10. Normalized XRD patterns of the Zn(O,S) films with different sulfur concentrations.

According to our Raman analysis and works reported by Meyer, et al. 2004 (Meyer et al., 2004), where the $ZnO_{1-x}S_x$ alloy consists of a single phase with wurtzite structure, c lattice constants were calculated from the (002) peak using equation 1 and 2 for wurtzite $ZnO_{1-x}S_x$ alloy and ZnO;

$$2d\ sin\theta\ = \lambda \tag{5.4}$$

$$\frac{1}{d_{hkl}^2} = \frac{4(h^2+hk+k^2)}{3a^2} + \frac{l^2}{c^2} \tag{5.5}$$

where h, k and l are the Miller indices of the plane, a and c are lattice constants, λ is the wavelength of Cu-K α line (λ = 0.15406 nm) and θ is the Bragg angle in degrees. The calculated c lattice constants with respect to the sulfur content (X_s) in the films are shown in Figure 5.11. The variation of the lattice constants of Zn(O,S) films shows linear variation, following the Vegard's law. With the shift of the (002) peak from 33.89° to 28.54°, the lattice constant c increases from 5.2856 to 6.0938 Å, resulting in 15.2 % expansion of the Zn(O,S) lattice along the c-axis.

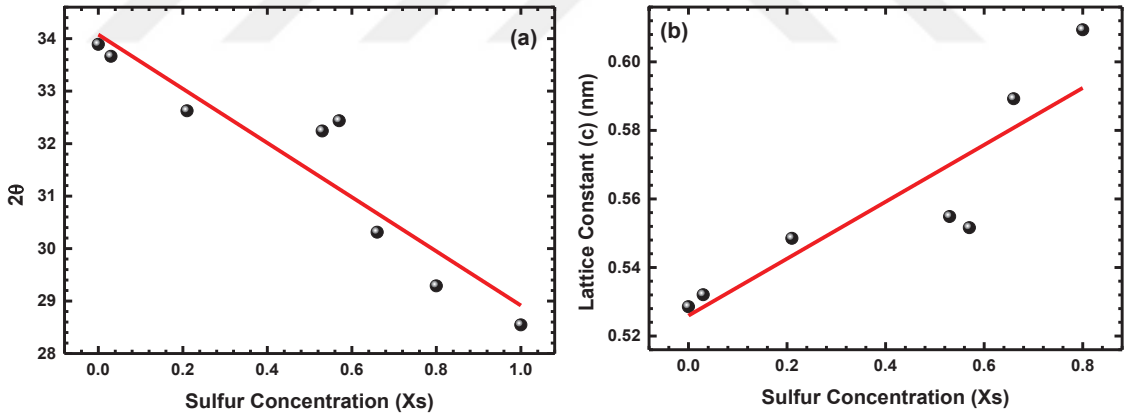

Figure 5.11. (a) 2θ and (b) calculated c lattice constants with respect to the sulfur concentration (Xs) in the films.

5.2.2 Raman Analyses

Raman measurements were performed at 488 nm excitation wavelengths for Zn(O,S) films. Due to the high optical band gaps of ZnS and ZnO, 325 nm excitation wavelength would be needed for resonant Raman scattering analysis of pure ZnO (Insignares-Cuello et al., 2015) and ZnS (Fairbrother, Izquierdo-Roca, et al., 2014) thin

films. On the other hand, there is a need for higher excitation wavelengths due to the strong bowing of the bandgap of the Zn(O,S) (Guc et al., 2016).

The Raman modes of Zn(O,S) can be understood by considering both the crystal symmetry of the ZnS and ZnO structures. The Raman modes of WZ ZnO was discussed in previous part. Zincblende ZnS have two atoms per primitive unit cell and belong to the space group $F\bar{4}3m$. It can be visualized most easily as two face-centered cubic lattices spaced apart from one another by one-quarter of a body diagonal. One lattice consists of sulfur atoms and the other of zinc atoms and thus has three optical and three acoustic phonons. The optical modes at the Γ point is represented as the following irreducible representation;

$$\Gamma = A_1 + E + T_2 \tag{5.6}$$

According to group theory analysis, only T_2 mode is Raman active for ZB. The optical modes of cubic ZnS crystals, which may be easily observed by first-order Raman scattering, are doubly degenerate transverse optical (TO) and single longitudinal optical (LO) zone center phonons at 276 and 351 cm^{-1}, respectively (Brafman & Mitra, 1968).

Wurtzite ZnS belongs to the space group $P6_3mc$ (Guc et al., 2016) with two Zn and two S atoms per unit cell. The optical modes at the Γ point is represented as the following irreducible representation (Cheng et al., 2009);

$$\Gamma = =A_1 + E_1 + 2E_2 + 2B_1 \tag{5.7}$$

Among these modes, the A_1 and E_1 modes are polar modes and are both Raman and infrared active, and E_2 modes are nonpolar and Raman active only. The B_1 modes are IR and Raman inactive (silent modes). First order Raman frequencies of zincblende and wurtzite ZnS are listed in Table 5.5.

Table 5.5. First order Raman frequencies of zincblende and wurtzite ZnS. (Source: Cheng et al., 2009)

Zincblende		**Wurtzite Zns**	
T_2 (TO)	278	E_2^1	72
T_2 (LO)	351	A (TO)	275
		E_1 (TO)	279
		E_2^2	285
		E_1 (LO)	353
		A_1 (LO)	353

Figure 5.12. shows the Raman spectra of $ZnO_{1-x}S_x$ films with different sulfur concentration ($0 \leq Xs \leq 1$). Spectrum involves ZnS and ZnO for comparison. As can be seen, The ZnS spectrum shows peaks located around 212, 262 and 348 cm^{-1}. Peak at 560 cm^{-1} is from the underlying SLG substrate which is due to high penetration depth of scattered photons in the samples (typically higher than one micrometer for 488 nm excitation). Since the deposition was performed at a low temperature, the peak located at 348 cm^{-1} was assigned to T_2 (LO) mode of ZB ZnS. The vibration line at 212 and 262 cm^{-1} are the second order Raman modes of ZB ZnS and can be attributed to the two-acoustic phonon combination at W (Cheng et al., 2009). The broad band at 262 cm^{-1} mentioned above can also include T_2 (TO) mode of ZB ZnS at 278 cm^{-1}. In the case of WZ ZnS, the peaks of 212 and 348 cm^{-1} can be attributed to LA overtones along M-K and A_1 (LO) + E_1 (LO) vibrational modes, respectively (see Table 5.5.). However, we could not attribute 262 cm^{-1} band to any of the first and second order Raman modes of WZ ZnS. We observed that when the S content in the layers decreases, T_2 (LO) mode at 348 cm^{-1} broadens and eventually vanishes which may be originated from formation of local point defects (He et al., 2012). Broadened LO mode seems to include E_2^2 mode of wurtzite type. Moreover, we observed small shift of LO band to higher frequencies. Peaks at 262 cm^{-1} disappears when small amount of O is introduced into ZnS. Shift and broadening of TO mode, and disappearance of second order peak unique to ZB ZnS may indicate the phase transition in the samples from the cubic to the hexagonal crystalline structure.

For WZ ZnO, the vibration lines at 443 and 571 cm^{-1} corresponds to E_2 (high) and A_1 (LO) modes, respectively. E_2 (High) mode of ZnO is related to vibration of oxygen atoms, it is extremely sensitive to the amount of S that substitutes O. Therefore, it

broadens immediately and eventually vanishes by introducing sulfur into ZnO. The A_1 (LO) mode of ZnO is very sensitive to the concentration of the doping impurity attributing point defects and it shows a significant shift towards lower frequencies with increasing S content in the Zn(O,S) films (Figure 5.13.). The red-shift of the A_1 (LO) mode with increasing S content is consistent with the XRD results. This behavior can be explained by the large difference between the radius of S^{2-} (1.84 Å) and O^{2-} (1.40 Å) (Mei et al., 2012). When more S substitutes in the O sublattice of Zn(O,S), respective bonds elongate by the expansion of the unit cell (Wang et al., 2005; Wang et al., 2007). Increase of the bond length tends to reduce the force constant and thus soften phonons mode to lower vibration frequency. By considering the double mode behavior of ZnS-like and ZnO-like peaks, we think that both wurtzite O-rich and S-rich Zn(O,S) ternary alloys coexist in the Zn(O,S) films, and solid solutions are achievable only for very high O or S concentrations.

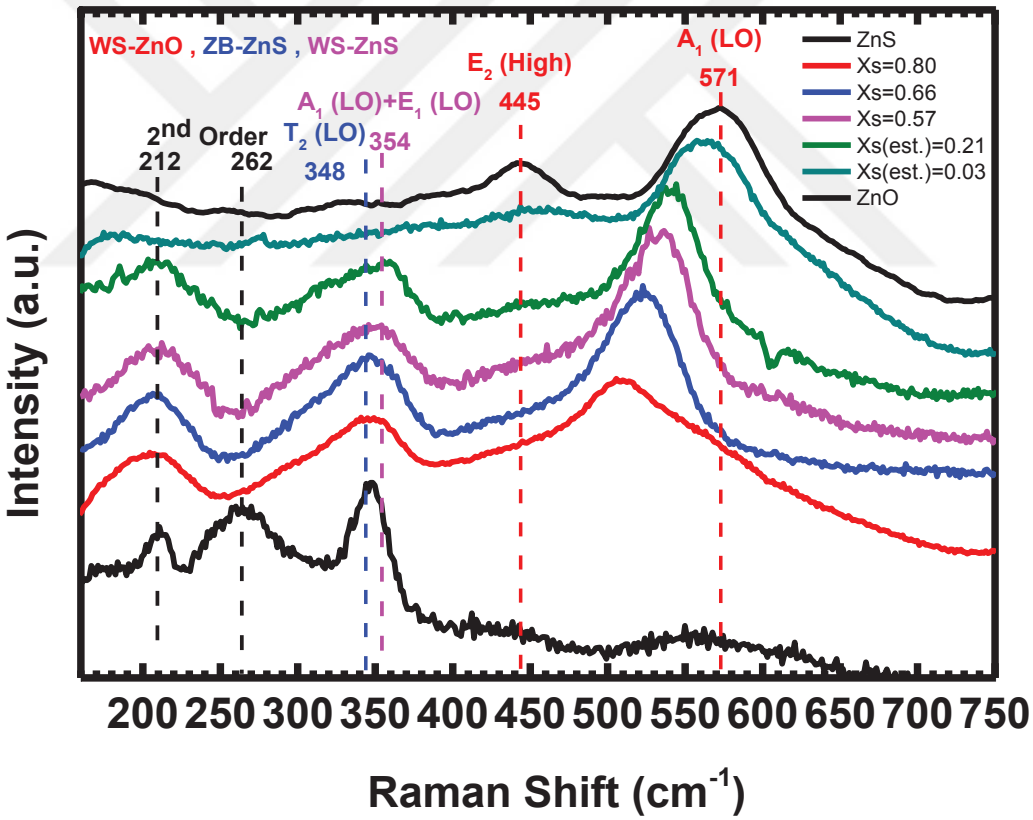

Figure 5.12. Raman spectra of Zn(O,S) films with different sulfur concentrations.

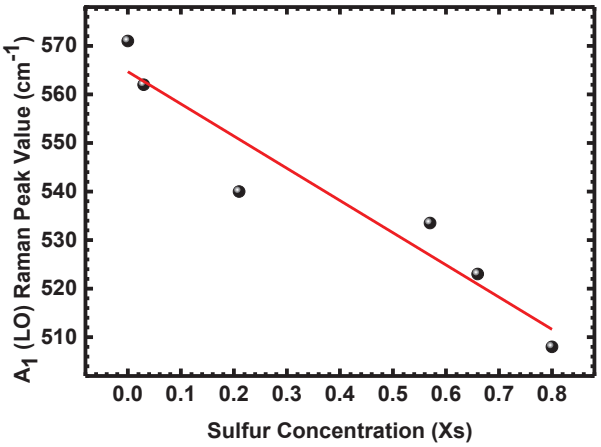

Figure 5.13. A_1 (LO) Raman peak position vs. sulfur concentration of Zn(O,S) films.

5.2.3 Transmission Analysis

Optical transmittance graphs of $ZnO_{1-x}S_x$ films with different sulfur concentration ($0 \leq x \leq 1$) are shown in Figure 5.14. As can be seen, the average transmittance of all films in the visible region (400–800 nm range) ranges from 75 % to 85%. The absorption edge of the samples (sharp decrease in transmittivity) was observed in the range from 270 to 400 nm. For sulfur concentration greater than 0.53, absorption edge shifts to shorter wave lengths, indicating increase in the band gap of the films. For lower sulfur concentrations, absorption edge shows an inverse trend, shifting to shorter wave lengths.

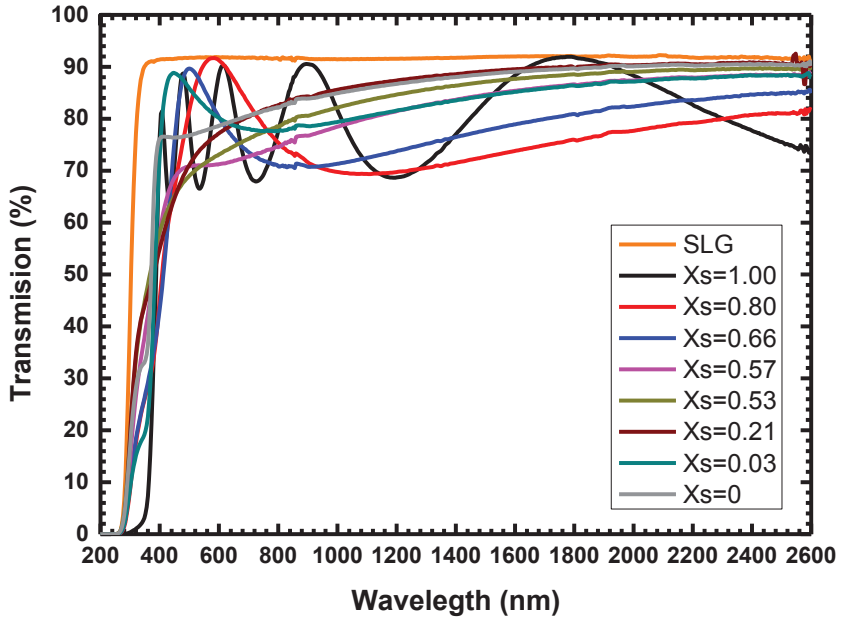

Figure 5.14. Transmittance graphs of Zn(O,S) films with different sulfur concentrations.

The band gap values for all layers Zn(O,S) films were determined based on the transmittance measurements. Tauc method was used to calculate the energy gap of the samples. Assuming an allowed direct transition of the Zn(O,S) films, absorption coefficient was calculated using fallowing equations;

$$T - R = e^{-\alpha t} \tag{5.8}$$

$$\alpha^2 = \frac{(In(T-R))^2}{t^2} \tag{5.9}$$

where T and R denote the transmittance and reflectance, respectively, and t is the thickness of the film. The bandgaps of the films are deduced from the extrapolation of the linear portion of the α^2 curve to the axis of hv.

Figure 5.15. shows α^2 vs photon energy graph for (a) Xs > 0.53 and pure ZnS (b) Xs < 0.53 and pure ZnO. As can be seen in the graphs, the band gap of the films decreases with the increasing amount of sulfur in the films up to Xs = 0.53 and it starts to increase for higher S content. This behavior shows that the band gap energy of the Zn(O,S) films can be tuned from 3.27 to 2.92 eV and the desired band alignment can be adjusted by O_2 gas flow control during deposition (Figure 5.16).

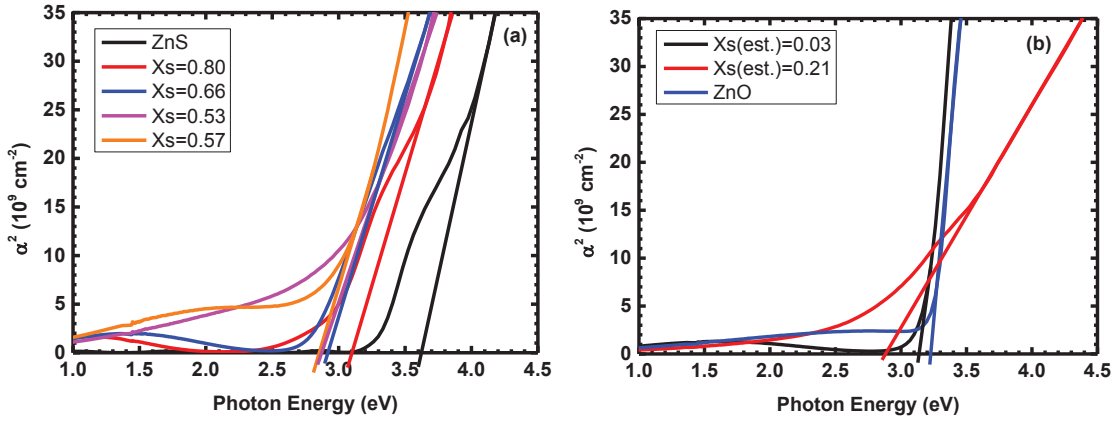

Figure 5.15. α^2 vs photon energy graph for a) Xs > 0.53, and pure ZnS and b) Xs < 0.53, and pure ZnO.

Figure 5.16. shows band gap values for films with sulfur content determined by XPS measurement. The band gap of a ternary compound semiconductor such as Zn(O,S) is expressed using Vegard's law;

$$E_{Zn(O,S)}(x) = x\,E_{ZnS} + (1-x)\,E_{ZnO} - b(1-x)x \quad (5.10)$$

here E_{ZnS} (3.6 eV) and E_{ZnO} (3.2 eV) are the band gap energies of binary compounds ZnS and ZnO at 300 K, X is the sulfur concentration in the films and b is the optical bowing parameter. When our data for known sulfur concentrations is fitted to this equation (Figure 5.16.), b is calculated to be approximately 2.41 eV, which is nearly consistent with the results from Meyer et al., 2004 (3.0 eV) (Meyer et al., 2004) and Pan et al., 2010 (2.9 eV) (Pan et al., 2010). After evaluating b, we estimated unknown concentrations using Vegard's law.

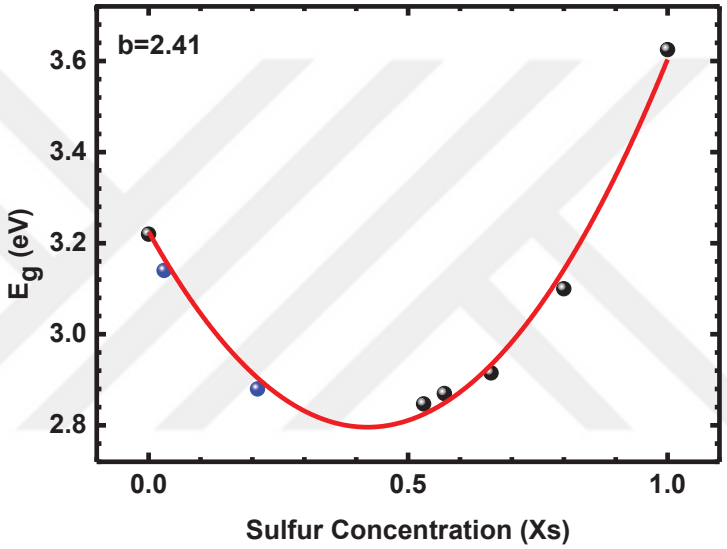

Figure 5.16. Energy gap vs sulfur concentration of Zn(O,S) films.

Table 5.6. Variation of the thickness, (002) peak positions, d spacing, c lattice constant and Energy Gap of Zn(O,S) thin films with different sulfur concentrations.

Sulfur concentration (X_S)	2θ	d spacing (nm)	c lattice constant (nm)	Eg (eV)	A_1 (LO) Raman peak value (cm^{-1})
1	28.55	0.31	0.62	3.63	-
0.8	29.29	0.30	0.61	3.10	508
0.66	30.31	0.29	0.59	2.92	523
0.53	32.24	0.28	0.55	2.87	533.5
0.57	32.44	0.28	0.55	2.85	NM
0.232	32.63	0.27	0.55	2.68	540
0.05	33.66	0.27	0.53	3.15	562
0	33.89	0.26	0.53	3.22	571

5.3. CZTS Thin Films

5.3.1. Effect of Sulfurization Time on the Properties of CZTS Thin Films

Sulfurization temperature and duration are the most important parameters for the formation of the CZTS absorber material with desired stoichiometry and optimal crystalline quality which play important roles in solar cell performance. In the beginning of the research, sputtering parameters (DC power, deposition time and gas flow) and sulfurization parameters (sulfurization temperature, amount of sulfur powder and gas flow) for metallic precursors were optimized according to Raman, XRD and EDX measurements.

After calibration processes of both stages, we investigate the effect of sulfurization time on the properties of CZTS thin films having different types of precursors. These precursors have the same stacking order (Cu/Sn/Zn/Cu), but have different thicknesses of Cu shared between top and bottom of the precursor stack. Growth parameters and structures of the samples discussed in this thesis are given in Table 4.5. For both Type 1 and Type 2 structures, Cu layer deposited on the top of the stack since Cu is non-volatile (low vapor pressure at 2.3 10^{-11} mbar) and it protects the loss of volatile Sn and Zn. Therefore, capping with Cu minimize tin loss during the sulfurization process and prevent the ZnS formation over the surface CZTS. Moreover, Cu layer at the bottom of the precursor stack prevent the adhesion problem of the Zn and Sn to the Mo surface according to our preliminary works.

5.3.1.1. Compositional and Morphological Analysis

SEM images of the Type 1 and Type 2 CZTS films sulfurized for different periods are shown in Figure 5.17. and Figure 5.18., respectively. All CZTS films shows homogeneous surface morphology with apparent grain structures. For both Type 1 and Type 2 samples, there are no significant changes in the microstructure with respect to sulfurization duration since the increase in grain diameter is a very slow process relative to the rate of sulfur incorporation and phase formation. SEM images all samples indicate that CZTS films contains large grains with a size around 800 nm. The large grains

decrease the recombination of photo-generated carriers at grain boundaries, so they can provide increase in the V_{oc} of a device.

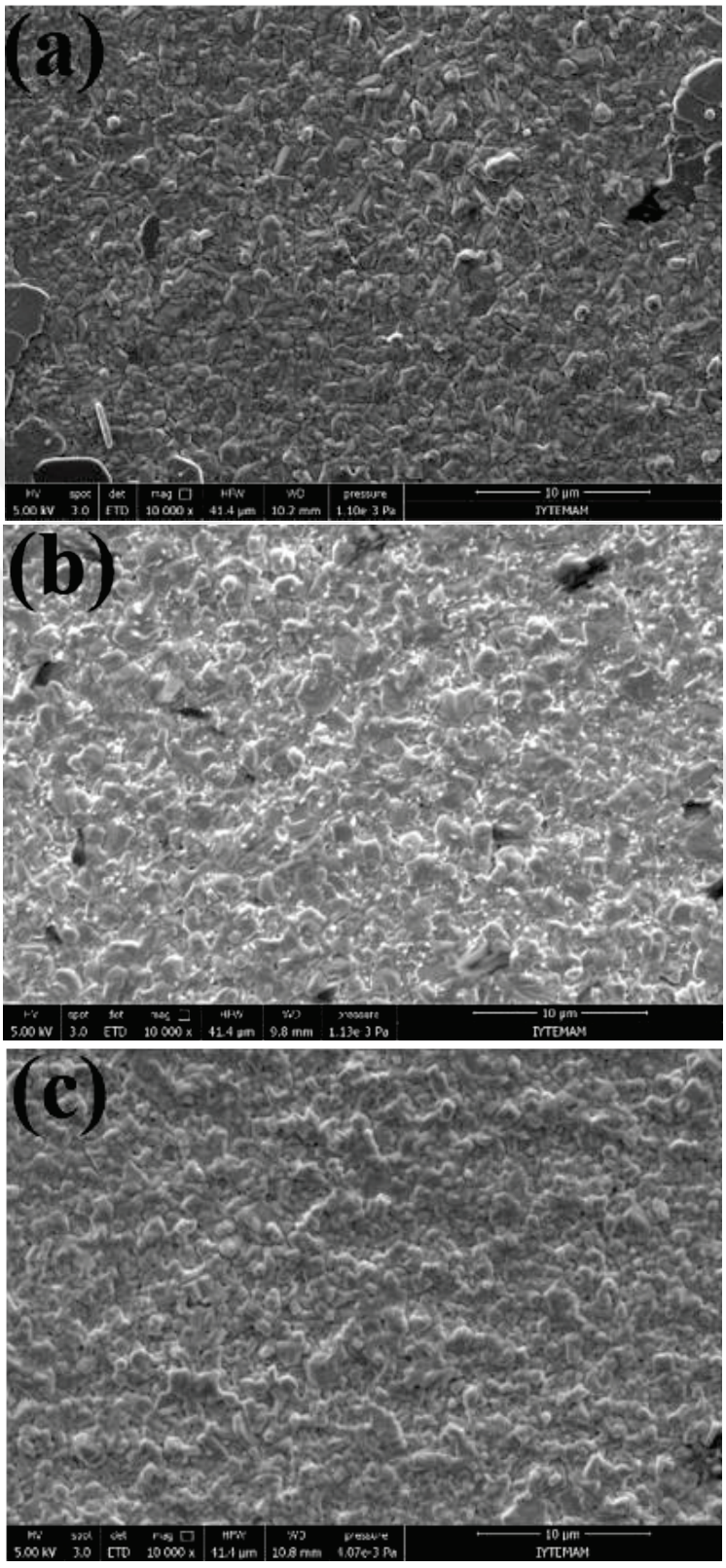

Figure 5.17. SEM images of Type 1 samples (a) Sample A (b) Sample B and (c) Sample C.

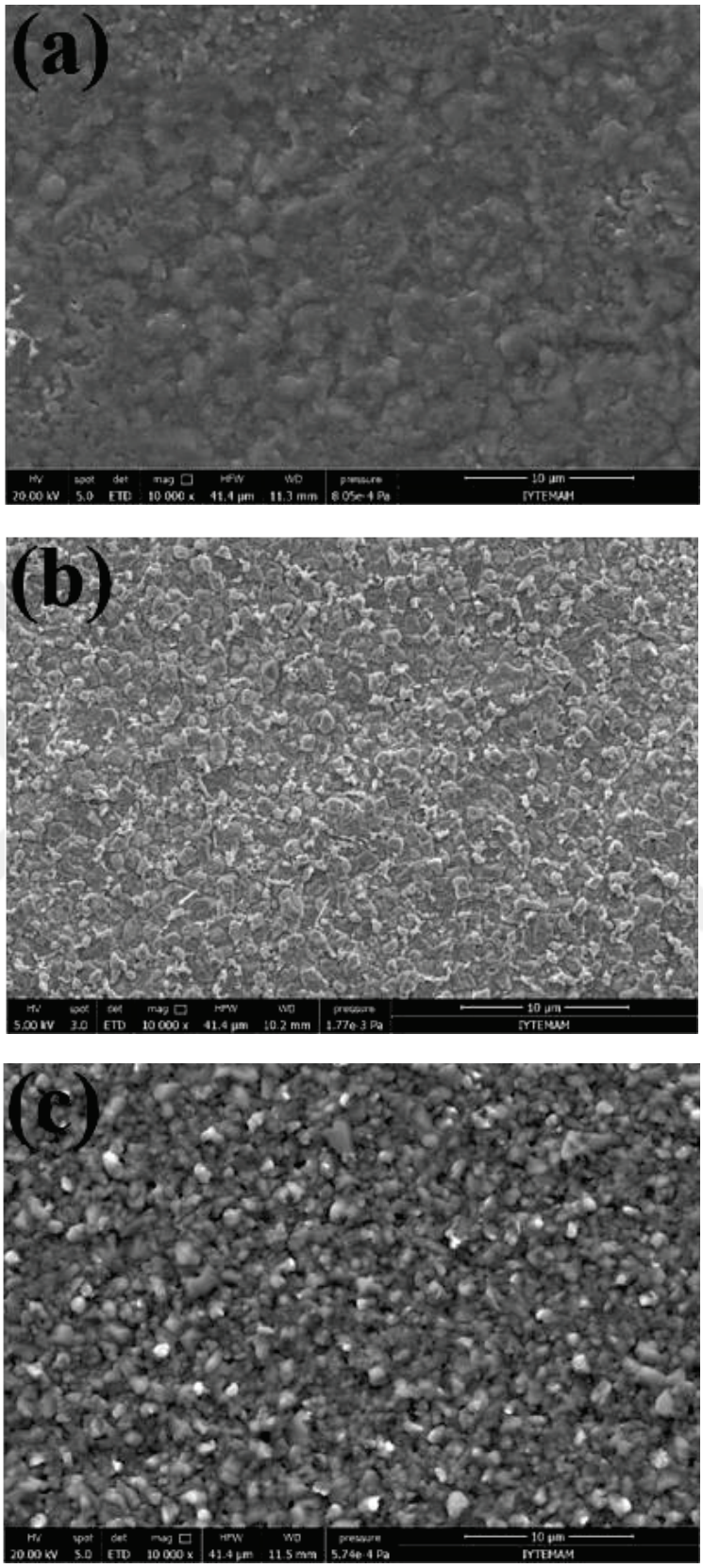

Figure 5.18. SEM images of Type 2 samples (a) Sample D (b) Sample E and (c) Sample F.

For Type 1 CZTS thin films, sample A and B shows large flat crystals over the entire sample surface as can be seen in Figure 5.19. (a) and (b). According to our preliminary works on the morphology of the CZTS films, we attributed this crystals to SnS_2. The crystals are mainly composed of Sn and S, detection of Cu and Zn is due to penetration of electrons through the sample.

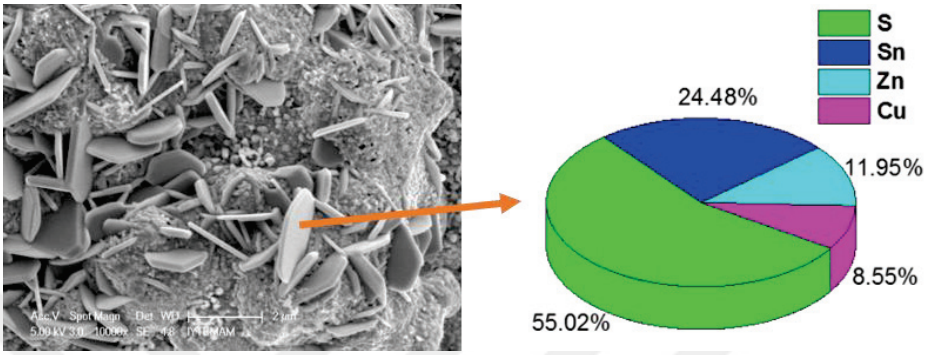

Figure 5.19. SEM image of SnS_2 crystals on CZTS.

The formation of SnS_2 phase over the entire sample surface is evidence of leaving of Sn from the film. This instability of the Sn during sulfurization of CZTS limits the sulfurization time due to Sn losses. For short sulfurization duration, there are many SnS_2 crystals on the surface which indicates Sn-rich composition of the film. Increasing the sulfurization time leads to decrease in the amount of SnS_2 phase over the surface. Finally, it disappears for long sulfurization duration due to Sn losses as can be seen in reaction 1;

$$2SnS_2\ (s) \rightarrow 2SnS\ (g) + S_2\ (g) \qquad \text{(reaction 1)}$$

EDX spectroscopy was performed to investigate the effect of sulfurization time on the chemical composition of synthesized CZTS thin films. Large area EDX scans were performed (approximately 150 μm^2) to include several grains. Table 5.8. shows the average elemental compositions and elemental ratios of the CZTS thin films. In fact, thicknesses of the Cu, Zn, and Sn films were adjusted to get Cu-poor and Zn-rich composition of the CZTS films by considering the molar fractions of Cu, Zn, and Sn ions. However, we get different compositions due to the loss of Sn by the evaporation of SnS binary compound and evaporation of Zn. For Type 1 samples, variation in Sn and S content as a function of sulfurization time can be seen in Figure 5.20. We observed that Sn and S content decreases with increasing sulfurization time. For short sulfurization

duration, high amount of SnS_2 phase over the surface results in S and Sn-rich composition of the film. When the sulfurization time increased, Sn composition of the film decreases due to Sn losses.

By investigating the rates of Sn loss for the CZTS films and multilayers of binary sulfides, Weber, et al 2009 concluded that in addition to direct evaporation of SnS (Weber et al., 2009), there is a decomposition pathway of CZTS;

$$Cu_2ZnSnS_4\ (s) \rightarrow Cu_2S\ (s) + ZnS\ (s) + SnS\ (g) + 1/2S_2\ (g) \qquad \text{(reaction 2)}$$

According to the decomposition pathway of CZTS SnS and S_2 are assumed to evaporate from the surface of the sample. Both reaction 1 and 2 explain why amount of S reduces by decreasing amount of Sn in our samples.

For Type 2 samples, we observed nearly same Sn and S content independent of sulfurization time. We attributed this behavior to higher Cu thickness at the bottom of precursor stack. To form CZTS, the last stage is through;

$$Cu_2SnS_3 + ZnS \rightarrow Cu_2ZnSnS_4 \qquad \text{(reaction 3)}$$

During the sulfurization Cu an Sn react with S easily and Cu_2SnS_3 forms by the reaction of $Cu_{2-x}S$ with SnS_2. We think that when Cu thickness at the bottom of the stack is high, more $Cu_{2-x}S$ and SnS_2 react and form Cu_2SnS_3 easily. Since Sn is bounded by the formation of Cu_2SnS_3, Sn loss decreases. When Cu thickness at the bottom of the stack is low, less Sn is bounded and Sn loss increases.

Table 5.7. The average elemental compositions and elemental ratios of the Type 1 and Type 2 CZTS thin films.

	Sample	**Cu (at %)**	**Zn (at %)**	**Sn (at %)**	**S (at %)**	$\frac{Zn}{(Sn)}$	$\frac{Cu}{(Zn+Sn)}$	$\frac{Sn}{(Cu+Zn+Sn)}$
Type 1	Sample A	20.15	11.27	14.09	54.49	0.8	0.79	1.20
	Sample B	26.58	14.7	12.32	46.4	1.19	0.98	0.87
	Sample C	27.74	14.88	11.89	45.49	1.25	1.04	0.83
Type 2	Sample D	21.50	11.94	12.13	54.43	0.98	0.89	1.19
	Sample E	21.35	12.03	11.86	54.76	1.01	0.89	1.21
	Sample F	20.87	12.27	12.17	54.69	1.01	0.85	1.20

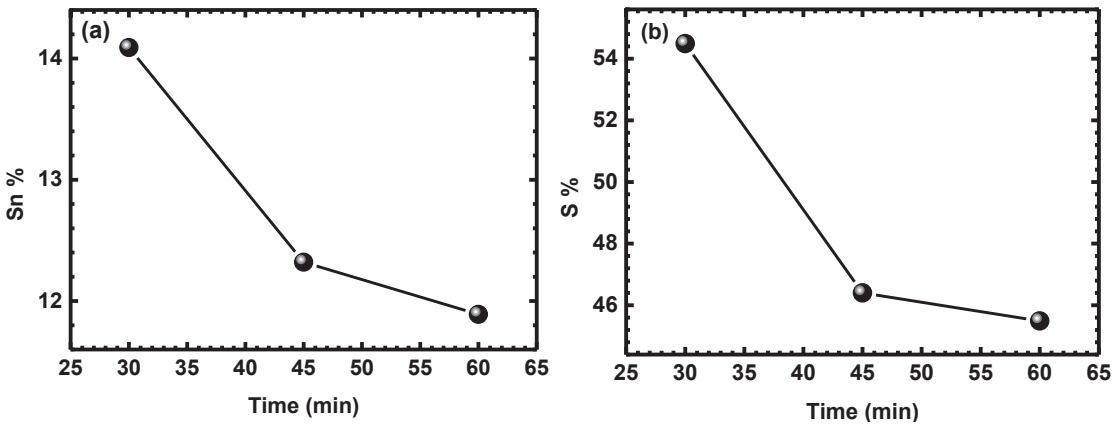

Figure 5.20. The variation in (a) Sn and (b) S content as a function of sulfurization time.

Figure 5.21. shows how elemental ratios of the Type 1 and Type 2 samples change with different sulfurization durations. While the relative ratios of Cu/(Zn + Sn), Zn/Sn, and S/(Cu + Zn + Sn) show different trends according to the sulfurization time due to formation of SnS_2 phases and the loss of Sn for Type 1 samples, these ratios show similar trend according to the sulfurization time for Type 2 samples. As mentioned previously, Cu-poor and Zinc-rich composition, which is generally accepted in the literature for the realization of high efficiency CZTS devices, may be desirable to suppress the formation of Cu-S phases, harmful defects and defect clusters such as Cu_{Zn}, Cu_{Sn},(Cu_{Sn} + Sn_{Cu}) and (Cu_{Zn} + Sn_{Zn}). However, due to volatility of Zn and Sn, we couldn't succeed both Cu-poor and Zinc-rich composition for any of the samples. While we get Cu-stochiometric and Zn-rich composition for Type 1 samples except for Sample A, we get Cu- poor and Zn-stochiometric composition for Type 2 samples. For Type 2 samples, Zn/Sn ratio close to 1 may eliminate the formation of ZnS phase which cause detrimental effect on CZTS devices. Cu-poor and Zn-poor composition with high S and Sn content for Sample A may indicate the higher amount of SnS_2 phase. For sample B and C, we observed low S content below %50 with S/(Cu+Zn+Sn)<1 due to loss of S resulting from decomposition reactions discussed above. It is believed that low S content in the CZTS films may cause the change of conduction from p-type to n-type and reduction of hole concentration due to high concentration of sulfur vacancy (V_s) (Yeh, Lei, Lin, & Yang, 2016). For all Type 2 samples, S content above 50 % with S/(Cu+Zn+Sn)>1 was obtained which is important to reduce V_s and get higher p-type conductivity.

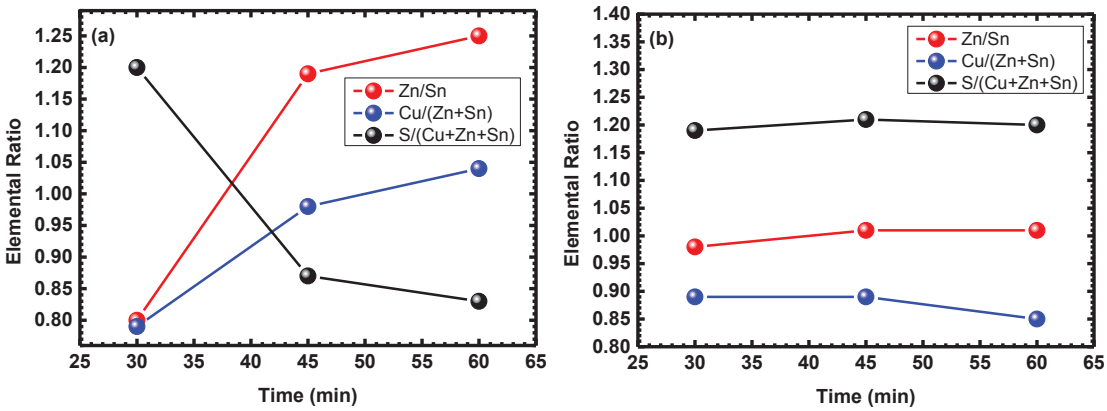

Figure 5.21. Change of elemental ratios of the (a) Type 1 and (b) Type 2 samples with different sulfurization durations.

5.3.2 XRD analysis

Figure 5.22. shows the X-ray diffraction patterns of the sulfurized Cu_2ZnSnS_4 (CZTS) with Type 1 and Type 2 structure. It can be seen that all of the films have a polycrystalline structure and exhibit characteristics peaks of CZTS along (110), (112), (103), (200), (202), (211), (105), (220), (312), (224), (008) and (332) crystallographic directions at 2θ values 23.18, 28.53, 29.74, 33.04, 37.02, 37.96, 45.01, 47.40, 56.15, 58.93, 69.31 and 76.49 °, respectively. Although XRD patterns match well with the standard XRD pattern of CZTS (JCPDS 26-0575) and those of the previously reported by other groups, peaks along (112), (200), (220), (312) and (224) directions at 2θ values 28.53, 33.04, 47.40, 56.15 and 58.93°, respectively, may indicate the presence of ZnS (JCPDS 05-0566) and Cu_2SnS_3 (JCPDS 027-0198) phases. It is clear from the XRD patterns that all the samples have good crystallinity and show preferential orientation along (112) direction with approximately same peak intensity. Extra peaks for Type 1 structure are attributed to the presence of SnO_2 at 26.6 ° (110) and 33.85 ° (101), which are the preferential orientation for SnO_2 (JCPDS 041-1445). For Type 2 structure, extra peaks are attributed to the presence of ZnO (JCPDS 00-036-1451) at 34.5 (002) and 36.1 ° (101) and MoO_2 (JCPDS 00-032-0671) at 25.7 ° ($\bar{1}11$). Additional peak at 42.58 couldn't be assigned any phases despite of detail investigation for Type 2 samples. A signal from the Mo back contact can be seen at 40.5 ° (110) (JCPDS 042-1120). Moreover, this peak also includes MoS_2 peak at 40.99 ° (JCPDS 024-0515). The peaks correspond to SnS_2 phase couldn't be detected by XRD (JCPDS 023-0677), it may be due to XRD detection limits or since this phase does not spread over the entire film surface.

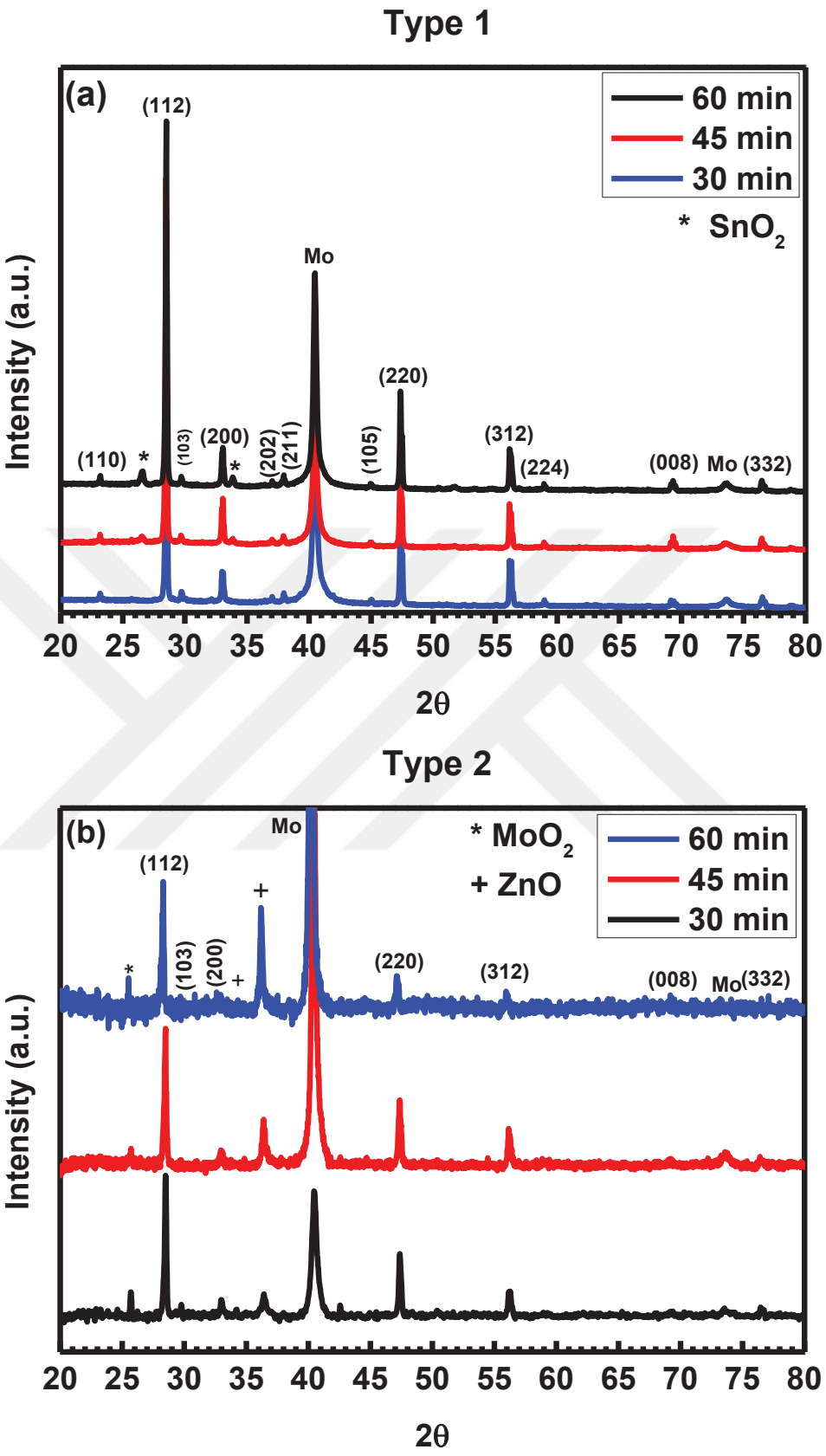

Figure 5.22. X-ray diffraction patterns of Cu_2ZnSnS_4 (CZTS) with (a) Type 1 and (b) Type 2 structure with different sulfurization durations.

Using the Scherrer's formula, we estimated the mean crystallite size in the samples;

$$D = \frac{0.9\lambda}{cos\theta} \tag{5.11}$$

where D is the average crystallite size (diameter), 0.9 is the particle shape factor, λ is the wavelength of Cu-K α line (λ = 0.15406 nm), B is the full width at half-maximum (FWHM) in radians, and θ is the Bragg angle in degrees. Since the FWHM of (112) plane approximately same for all samples, the estimated crystallite sizes around 60 nm regardless of sulfurization time.

Using the following relation, lattice parameters of the samples were calculated

$$\frac{4Sin^2\theta}{\lambda^2} = \frac{h^2+k^2}{a^2} + \frac{l^2}{c^2} \tag{5.12}$$

where h, k and l are the Miller indices of the plane, a and c are lattice constants, λ is the wavelength of Cu-K α line (λ = 0.15406 nm) and θ is the Bragg angle in degrees. 28.45 ° corresponding to (112) plane and 47.36 ° corresponding to (220) plane were chosen as the 2θ values. For both Type 1 and Type 2 samples, calculated lattice constants, a=0.5418 nm and c=1.0800 nm, are in good agreement with the reported single crystal data (a=0.5427 nm and c=1.0848 nm).

ZnO, SO_2 and SnO_2 are thermodynamically favorable native oxides on CZTS relative to CuO since they have high enthalpy of formation (Sardashti et al., 2015). However, SO_2 can easily evaporate due to its high vapor pressure. Figure 5.23. (a) shows the magnified view of SnO_2 peaks detected for Type 1 samples. Evolution of SnO_2 interfacial phase over the sulfurization time can be clearly seen in the XRD graphs. While the films sulfurized for 30 min does not show any sign of SnO_2 phase, the films sulfurized for 45 min and 60 min show SnO_2 peaks along (200), and (332) crystallographic directions. Moreover, the intensity of the SnO_2 peak increases as the sulfurization time increases. These results indicate that sulfurization at high temperature (550 °C) for longer durations trigger the formation of SnO_2 which results from oxygen exposure during the sulfurization in an open atmosphere. The formation of SnO_2 results from removing the Sn from the CZTS thin film and evidence of loss of Sn in CZTS. Moreover, formation of SnO_2 indicates that if the thick Cu layer is not adjacent to Sn layer, Cu cannot bound Sn

by the formation of Cu_2SnS_3 and Sn loss increases. By considering SnO_2 as an indicator for Sn loss, we concluded that the formation of SnO_2 cause the severe loss of Sn in CZTS and Sn loss increases for long sulfurization times due to more oxygen exposure. This tendency is in good agreement with the EDX results.

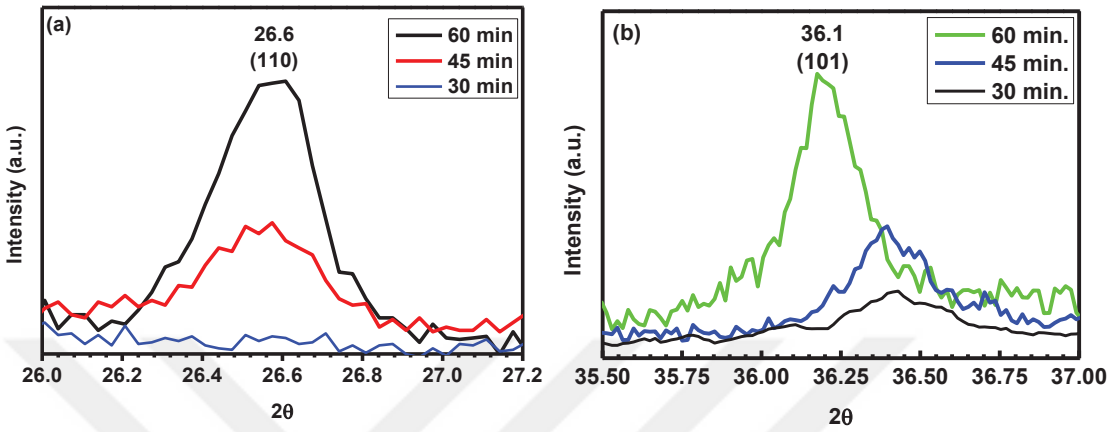

Figure 5.23. The magnified view of (a) SnO_2 peak for Type 1 samples, (b) ZnO peak for Type 2 samples.

For Type 2 samples, Figure 5.23. (b) shows the magnified view of ZnO peaks. Evolution of ZnO interfacial phase over the sulfurization time can be clearly seen in the XRD graphs. The intensity of the ZnO peak increases as the sulfurization time increases which indicates that sulfurization for longer durations trigger the formation of ZnO at high temperature (550 °C) for the precursors having thin Cu cap layer. We think that this thin Cu cap layer cannot prevent the diffusion of Zn to the surface and formation of ZnO, while the formation of SnO_2 is prevented by thick Cu layer at the bottom of the stack since $Cu_{2-x}S$ and SnS_2 react and form Cu_2SnS_3 easily and Sn is bounded by the formation of Cu_2SnS_3.

It is difficult to distinguish the ZnS and Cu_2SnS_3 secondary phases from CZTS by XRD since they exhibit similar crystal structure with CZTS. However, when we look at the magnified view of (220), (312) and (224) peaks (Figure 5.24.) for Type 1 and Type 2 films, we observed peak splitting, most probably indicating a formation of the ZnS and/or Cu_2SnS_3 secondary phases, but a unique attribution is not possible. The peaks appear at 37.0 and 37.9 ° associated with only CZTS, this suggest that our films mainly composed of CZTS.

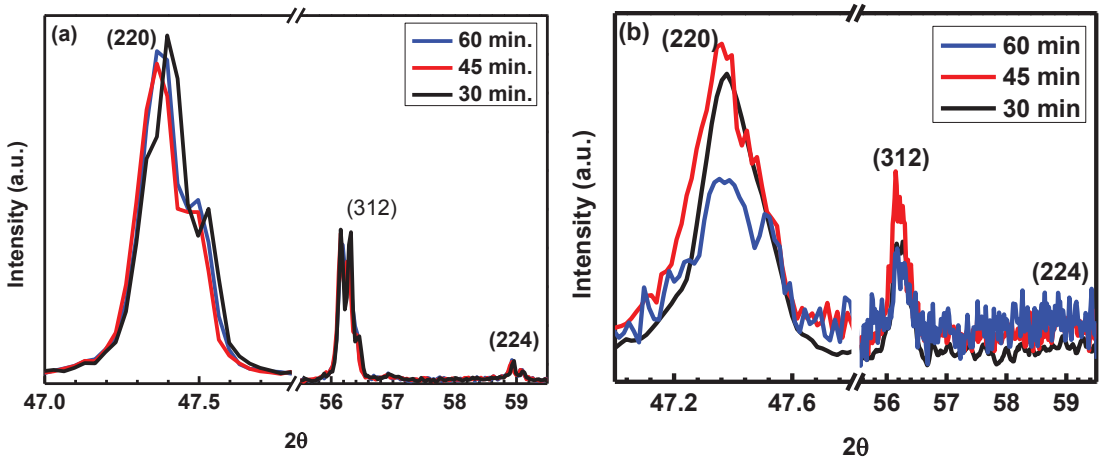

Figure 5.24 The magnified view of (220), (312) and (224) peaks for (a) Type 1 and (b) Type 2 films.

5.3.3. Raman scattering analysis

As mentioned earlier, the most probable ZnS cubic phase and both cubic and tetragonal Cu_2SnS_3 phases exhibit a crystal structure very similar to CZTS, so it is quite difficult to distinguish phases from CZTS phase by XRD (see chapter 3). Therefore, these absorbers were further examined by the Raman spectra. Raman studies were performed using High-resolution Raman spectroscopy in the back-scattering mode at room temperature. Excitations in the visible regime (514.5 nm and 633 nm) were used to analyze the samples. The probing depth of the Raman spectroscopy can be determined by the absorption coefficient (α) of the material for the respective wavelength of the excitation source. In the case of backscattering configuration, it is roughly given by $d \approx 1/(2\alpha)$. This results in penetration depth of scattered light of around 100 nm for CZTS with an absorption coefficient > 10^4 cm^{-1}.

The optical modes at the at the center of the Brillouin zone, Γ point, can be calculated using group theory and the crystal's symmetry (Rousseau, Bauman, & Porto, 1981). The CZTS compound crystallizes in the kesterite type lattice structure (KS) and this structure is assigned to space group I4. Kesterite structure implies a basic unit of 8 atoms in the CZTS unit cell. Since N different types of atoms in the primitive cell results in 3N vibrational modes, 8 atoms in the CZTS unit cell yields twenty-four phonons at the center of the Brillouin zone with N=3 acoustic phonons and 3N - 3 = 21 optical phonons. Using Mulliken notation, the optical modes at the at the Γ point is represented as fallows;

$$\Gamma = 3A + 7B + 7E \quad (5.13)$$

Among these modes, 15 modes are Raman active (3A + 6B + 6E), from them 12 modes are also IR-active (6B + 6E), which leads to their LO-TO splitting, and E modes are double degenerated. The rest two modes are acoustic (B + E). The strongest peak observed in the experimental Raman spectra of CZTS is A mode which results from symmetrical vibrations of only anion lattice and do not involve any cation motion. B mode results from vibrations of cations along z-axis. The phonon states are mainly composed of vibrations of the Zn, Cu and Sn cations with some contribution from the S anions for 50–160 cm^{-1}, vibrations of the Zn cations and S anions with some contribution from the Cu cations for 250–300 cm^{-1}, vibrations of S anions for 310-340 cm^{-1} and vibrations of Sn cations and S anions for 340-370 cm^{-1} are composed of the vibrations of Sn cations and S anions (Khare et al., 2012). Calculated Γ-point phonon frequencies (in cm^{-1}) of the CZTS are given in Table 5.8. Moreover, Raman peaks' position of the chalcogenide compounds used to identify the phases present in CZTS are listed in Table 3.4.

Table 5.8. Calculated Γ-point phonon frequencies (in cm^{-1}) of the CZTS. (Source: Khare et al., 2012)

	Symmetry	**Raman scattering peak (cm^{-1})**	
Kesterite CZTS	A	340.04	
		284.3	
		272.82	
	B (TO LO)	355.8	374.05
		309.56	313.19
		238.48	254.73
		166.65	168.21
		98.82	98.83
		86.7	87.51
	E (TO LO)	351.55	366.35
		281.07	293.44
		250.26	257.85
		150.53	151.05
		105.93	106
		83.64	83.65

Figure 5.25. (a) and (b) shows the Raman spectra of CZTS thin films with Type 1 and Type 2 structure, respectively. Excitation in 514.5 nm wavelength with 150 nm penetration depth for Type 1 samples was used, whereas excitation in 633 nm wavelength with 170 nm penetration depth for Type 2 samples was used to analyze the samples.

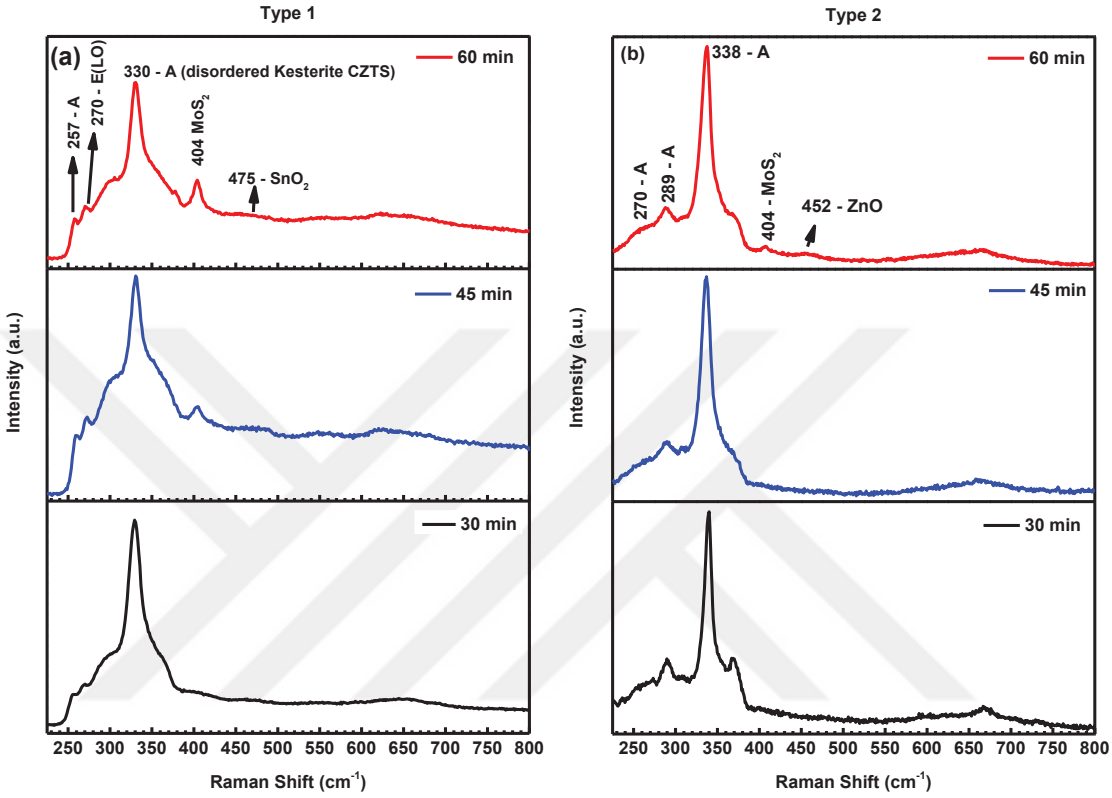

Figure 5.25. Raman spectra of CZTS thin films with (a) Type 1 and (b) Type 2 structure.

We observed that the most intense peak in the Raman spectra of Type 1 samples lies between 330 - 332 cm^{-1} (Figure 5.25. (a)) and they are attributed to A mode of KS. In fact, A mode of kesterite structure has been observed between 331 and 338 cm^{-1} and varies with the synthesis method although reports of 337-338 cm^{-1} are the most common. Shifting of the A mode of KS towards lower frequencies are attributed to the existence of disorder effects caused by the high concentration of intrinsic structural defects in the CZTS films. Even in stoichiometric compounds, the existence of Cu_{Zn} and Zn_{Cu} antisite defects has been demonstrated using neutron powder diffraction method. It is now generally believed that CZTS crystallizes in the kesterite type structure with the same amount of disordered kesterite phase. Presence of this disordered kesterite phase is characterized by a random distribution of Cu and Zn cations in the Cu-Zn planes (Figure 5.26.) and the leads to changes space symmetry from kesterite type I4 to a disordered

kesterite phase I42m symmetry. For Cu-poor samples, it was shown that all Zn atoms and half of the Cu atoms are distributed on both 2c and 2d Wyckoff position in the planes at z = ¼ and ¾ and the other Cu atoms in the planes at z = ¼ (Wyckoff position 2a) is not influenced. Due to the remaining Cu in the planes at z = ¼, it does not correct to attribute this cation distribution to the stannite-type structure. The binding energy difference between KS and ST structures is about 3 meV/atom, thus, it may be supposed that the difference in binding energy between the KS and disordered KS structures may be less than 3 meV/atom (Valakh et al., 2013). The formation of CZTS was confirmed by the presence of an intense peak located at about 331 cm^{-1} belongs A mode of the disordered KS structure and weak peaks around 257 cm^{-1} (A mode) and 270 cm^{-1} E(LO). Moreover, broad shoulders at the right and the left of the main CZTS peak can be explained by CZTS modes at 289 cm^{-1} (A mode), 309 cm^{-1} (B (TO) mode) and 370 cm^{-1} (B (LO) mode). These broad shoulders may possibly include peaks at 297 and 337 cm^{-1} for tetragonal CTS, 303 cm^{-1} and 355 cm^{-1} for cubic CTS, 318 cm^{-1} for orthorhombic CTS, 277 and 350 cm^{-1} for cubic ZnS and 314 cm^{-1} for SnS_2 (Fernandes et al., 2011). The peak at 404 cm^{-1} corresponds to MoS_2 phase. Presence of this phase implies that part of CZTS absorber is not continuous which may lead to serious shunting. In addition, Raman measurements confirm the presence of SnO_2 phase by the broad peaks located at 475 cm^{-1}.

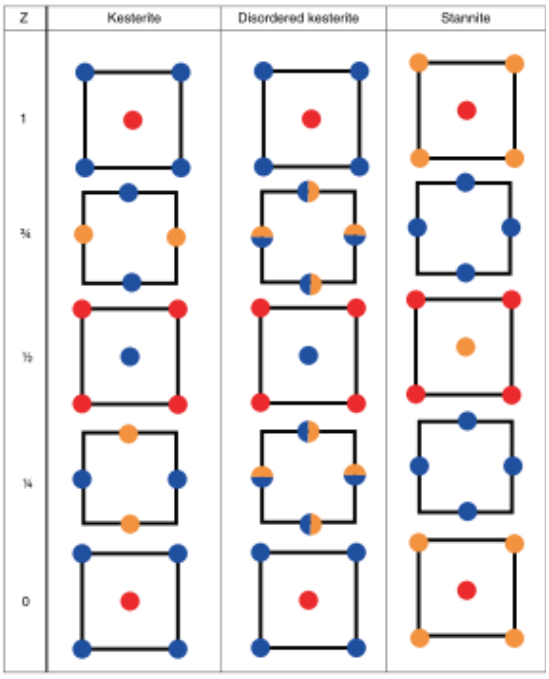

Figure 5.26. Distribution of Cu and Zn cations in the Cu-Zn planes for the kesterite, disordered kesterite and stannite structures.

Since Raman spectra of Type 1 samples give a general broadening due to the reduction in phonon correlation length caused by disorder (defects), a special attention was given for the range 250-450 nm since main Raman modes of CZTS and many secondary phases lies in this range. In order to clarify the presence of the peaks was not experimentally resolved in our spectra, we fitted the experimental spectra with Lorentzian curves using Origin program (Figure 5.25. (a)). First, we assumed that the film contains only the KS CZTS structure, the peak positions were settled according to mostly reported Raman modes of KS CZTS with disordered KS peak at about 331cm^{-1} and allowed to vary to get the best fit to the experimental spectra. We observed significant deviations between the fixed peak positions before deconvolution and the varied peak positions after deconvolution. Then, we took into account the presence of KS CZTS peak at about 338 cm^{-1} deconvolutions improved significantly. This indicates that both kesterite and disordered kesterite structures coexists in the real structure of our CZTS thin films with the dominance of disordered kesterite structure as can be seen in Figure 5.27. (a). To determine the goodness of fit, we employed reduced chi-square and adjusted r square value. During an iterative procedure, reduced chi-square value decreases and r-square value closes to 1 as the goodness of the fit increases. Peak positions obtained after deconvolution are listed in Table 5.9.

A mode results from vibrations of only anion lattice and its vibrational frequency w is given by $w = \sqrt{k/M_s}$, where k is the lattice vibration force constant and M_S is the atomic mass of sulfur. In the case of Cu-poor and Zn-rich condition, respective bonds elongate by the expansion of the unit cell due to higher atomic weight of Zn (65.38 g/mol) than atomic weight of Cu (63.55 g/mol). Increase of the bond length tends to reduce the force constant and thus soften phonons mode to lower vibration frequency than A symmetry mode of KS at 338cm^{-1}. Moreover, defects result from Cu-poor and Zn-rich condition such as Zn_{Cu} and V_{Cu} may promote additional non-center phonon scattering to the Raman line and results in Raman bandwidth broadening (Rudigier, Luck, & Scheer, 2003). Tetragonal-CTS, Cubic-CTS and Cubic-ZnS are the possible secondary phases may present in the CZTS films according to the deconvolution results (Table 5.9). In fact, such broad shoulders at the right and the left of the main CZTS peak indicates the presence of CTS and ZnS phases even without deconvolution. Both disordered structure and remaining CTS and ZnS phases implies incomplete formation of CZTS. As in SEM,

EDX and XRD analyzes, Raman results also confirms that formation of CZTS is restricted when the thick Cu layer is not adjacent Sn layer.

Presence of at least one of these phases in the films also explain the peak splitting observed in XRD analysis. Since the cations Cu^{+} and Zn^{2+} have the same number of electrons, both cations are not distinguishable by X-ray diffraction method (Schorr, 2007). It explains why we couldn't distinguish disordered kesterite structure by X-ray measurements.

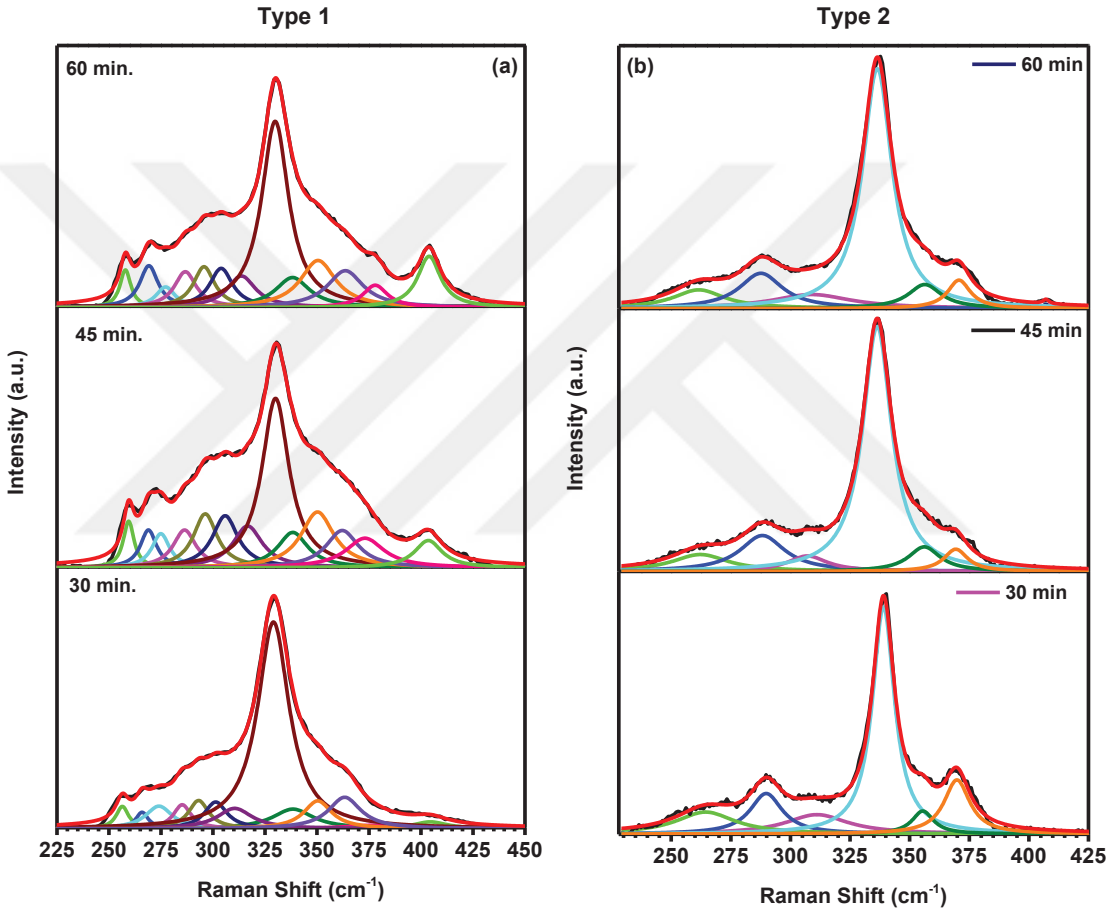

Figure 5.27. Deconvoluted Raman spectra of CZTS thin films with (a) Type 1 and (b) Type 2 structure.

Table 5.9. Positions of the peaks observed in fitted Raman spectra of the Type 1 films sulfurized at different times.

	30 min	45 min	60 min	Possible CZTS modes	Possible Secondary Phases
Peak1(D)	256.43	259.47	257.91	B (LO)	
Peak2(D)	265.89	268.97	269.20	A	
Peak3(D)	274.03	274.93	277.20	-	ZnS
Peak4(D)	285.19	286.35	286.70	A	
Peak5(D)	293.08	296.29	295.70	E (LO)	Tetragonal-CTS
Peak6(D)	301.30	305.87	303.94	-	Cubic-CTS
Peak7(D)	310.44	316.67	313.67	B (TO)	SnS2
Peak8(D)	329.08	330.08	329.90	Disordered KS	
Peak9(D)	338.43	338.37	338.25	A	
Peak10(D)	350.37	350.25	350.51	B (TO)	ZnS
Peak11(D)	363.31	362.16	363.63	E (LO)	
Peak12(D)	377.37	373.08	378.01	B (LO)	
Peak13(D)	404.49	403.52	403.91	-	MoS_2

In the Raman spectra of Type 2 samples, we observed that the most intense peaks lie between 337- 339 cm^{-1} (Figure 5.25. (b)) and they are attributed to A mode of KS with ordered structure. This indicates the reduced number of defects compared to Type 1 samples. Since formation of CZTS restricted for Type 1 samples, it is more probable to formation of defects and secondary phases. Weak peaks around 270, 289 and 370 cm^{-1} attributed to A, A and B (LO) modes, respectively. For the sample F sulfurized during 60 min, we observed extra peaks at 407 cm^{-1} and at 551 cm^{-1}. Peak at 407 cm^{-1} belongs to MoS_2 phase. Peak at 551 cm^{-1} may be assigned to E_2 (High) mode of ZnO. However, direct attribution is not possible since this mode generally appears between 437 - 444 cm^{-1} (Russo et al., 2014). In fact, due to the high optical band gaps of ZnS (~3.6 eV) and ZnO (~3.2 eV), 325 nm excitation wavelength would be needed for resonant Raman scattering analysis of pure ZnO (Insignares-Cuello et al., 2015) and ZnS (Fairbrother, Fourdrinier, et al., 2014). MoO_2 observed in XRD analyses couldn't be detected due to the low penetration depth (170 nm) of laser. The broad band at 668 cm^{-1} can be attributed to second order of the main Raman band of CZTS at 338 cm^{-1}. Presence of this band indicates the improved crystalline quality of the material (Pal, Mathews, Gonzalez, & Mathew, 2013).

As it can be seen from Figure 5.27. (b), Raman curve shows less broadening in the range of 250-450 nm for Type 2 samples. Peak positions obtained after deconvolution

of the Raman spectra of Type 2 samples are listed in Table 5.10. Among all samples, the highest degree of ordering in CZTS was obtained for Sample D with 30 minutes sulfurization. Cubic-ZnS is the only possible secondary phase may present in the CZTS films according to the deconvolution results. Both XRD and Raman analysis indicate that Type 2 structure with thicker bottom Cu layer in precursors and 30 min sulfurization of precursors is the best to get the highest degree of ordering and complete CZTS formation.

Table 5.10. Positions of the peaks observed in fitted Raman spectra of the Type 2 films sulfurized at different times.

	30 min	**45 min**	**60 min**	**Possible CZTS modes**	**Possible Secondary Phases**
Peak1(D)	264.42	262.20	261.56	A	
Peak2(D)	289.81	288.22	287.59	A	
Peak3(D)	311.10	307.11	308.90	B (TO)	
Peak4(D)	339.03	336.38	336.44	A	
Peak5(D)	353.50	354.14	354.36	B (TO)	ZnS
Peak6(D)	369.83	369.35	370.69	B (LO)	
Peak7(D)	-	-	407.17	-	MoS_2

CHAPTER 6

CZTS SOLAR CELL CHARACTERIZATION

6.1. Distortion of the J-V curves

Figure 6.1. illustrates the dark and illuminated J-V characteristics of one of our devices in which Zn(O,S) buffer has sulfur concentration of Xs= 0.53. Dark J-V characteristics indicates the formation of high quality junction between the CZTS absorber and Zn(O,S) buffer. Illuminated J-V characteristics shows photo response at the fourth quadrant. Strong distortion of the J-V curve under light can be seen, the curve shows a kink-like shape in the forward bias direction. CZTS solar cell devices fabricated in this work suffer from low fill factor (FF) and short circuit current density (J_{sc}) essentially due to this distortion. Open circuit voltage (V_{oc}) values are comparable to that of the best CZTS devices reported up to now.

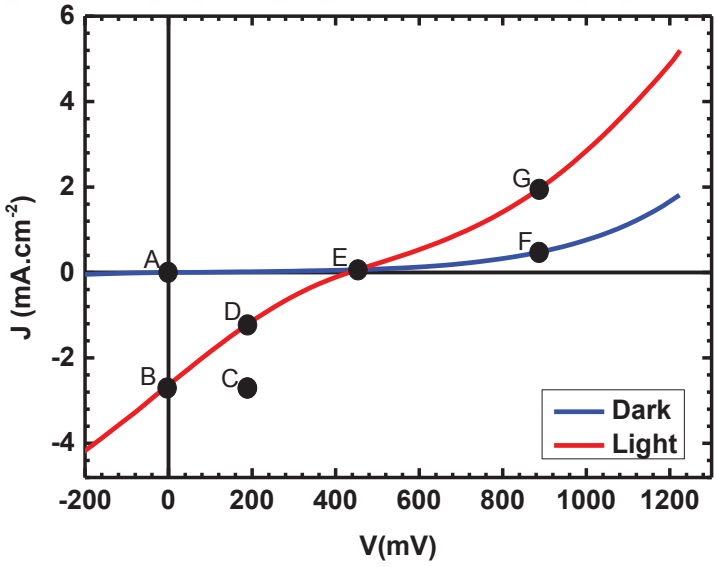

Figure 6.1. Typical J-V distortion observed in Zn(O,S) buffered CZTS cells.

J-V distortion, the reduced current density and the reduced fill factors can be explained by the barriers at the hetero-junctions (Pudov, Kanevce, Al-Thani, Sites, & Hasoon, 2005). The barrier height (Φ) is defined as the distance between the Zn(O,S)

conduction band at the Zn(O,S)/CZTS interface and the electron Fermi level (E_F) at the ZnO/Zn(O,S) interface. Spike like conformation between buffer and absorber layer forms a secondary barrier. If the barrier height is high, it may restrict electron transport and thus leads to the J–V distortion. The conduction band offset between CZTS and Zn(O,S), electron doping density the Zn(O,S) and band gap of Zn(O,S) are the main factors that affect the barrier height (Figure 6.2.). The barrier height increases as the conduction band offset between CZTS and Zn(O,S) increases which results in reduced electron current flowing across the interface (Figure 6.2. (a)). The low the electron density in Zn(O,S) also results in higher barrier height across the interface (Figure 6.2. (b)). When the electron density in Zn(O,S) is higher, E_F become closer to the conduction band, the amount of the positively charged fixed donors increases and this leads to downward band bending in the Zn(O,S) and thus reduction of the barrier height for electrons. In comparison with CdS, Zn(O,S) result in a higher ΔE_c barrier with the same absorber due to its wider bandgap (Figure 6.2. (c)). In order to understand the effect of Zn(O,S) band gap, firstly we should consider the change in Zn(O,S) effective doping density under the dark and light illumination (Figure 6.3.). There are acceptor-like deep defects in the mid-gap region of Zn(O,S) for electrons (Fermi level of Zn(O,S) is above mid gap (n-type material)). In the dark, acceptor-like defects compensate the dominant n-type (donor) doping of the Zn(O,S). These acceptor-like defect states capture electrons from the donor state and ionized, thus effective electron density of the Zn(O,S) decreases. Since more negative space charge is created inside the Zn(O,S), which results in reduction of conduction band bending. Under illumination, electron-hole pairs are generated by the photons with higher energy than the band gap of Zn(O,S). The acceptor traps capture the photo-generated holes and neutralize. They become mostly unoccupied because of the excess of the photo-generated holes. The photo-generated electrons are not affected and increases the free electron density of Zn(O,S). Deep donors are ionized (positively charged) and results in downward band bending in the Zn(O,S). Thus, the barrier height for electrons are reduced. However, if the band gap of Zn(O,S) is high (e.g. 3 eV), the amount of photo-generated electrons will be low, thus most free electrons in the Zn(O,S) buffer layer are captured by the acceptor traps in Zn(O,S). The barrier height relative to low band gap CdS will be higher due to the lack of high energy photons. Therefore, a J-V distortion can be observed even under white light for Zn(O,S) with higher band gap .

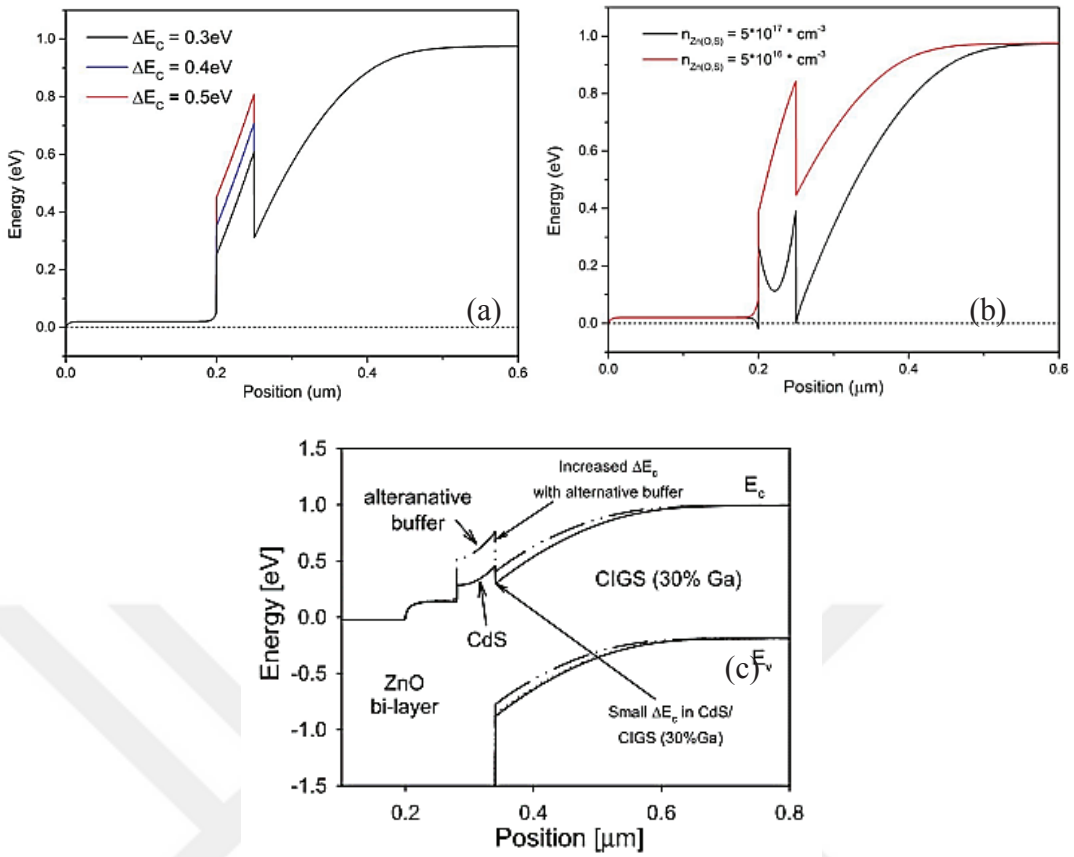

Figure 6.2. Effects of a) the conduction band offset between CZTS and Zn(O,S), b) electron doping density the Zn(O,S) and c) band gap of Zn(O,S) on the barrier height.
(Source: Pudov et al., 2005)

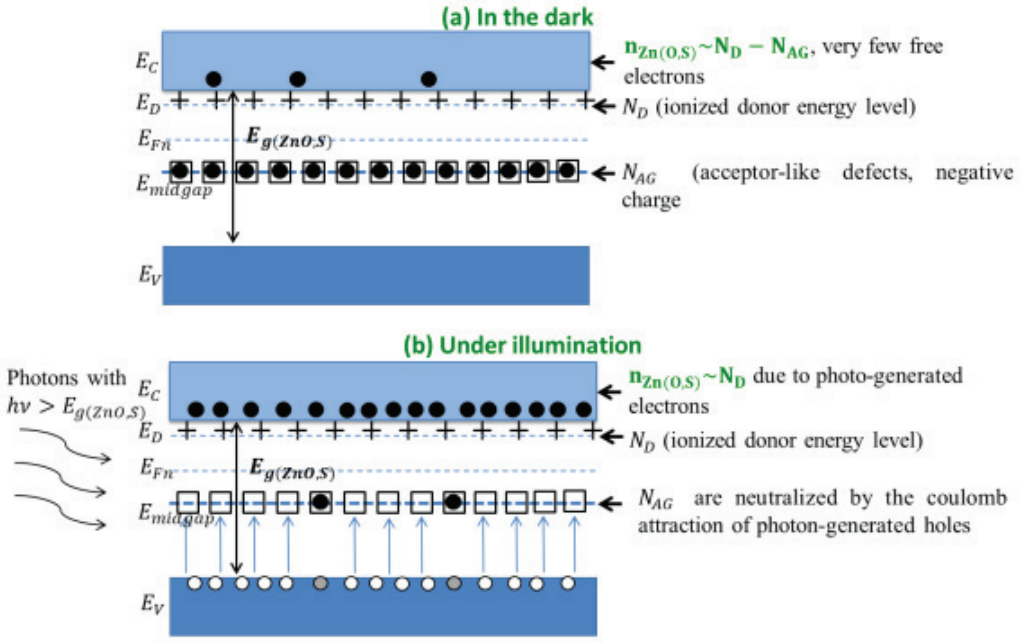

Figure 6.3. Change in Zn(O,S) effective doping density under the dark and light illumination conditions.
(Source: Song, 2013)

The analyses of distorted J–V curve (Figure 6.1.) is given below;

Point A (0 V, dark): The net current is zero. There is no photocurrent and forward current. There is only little thermionic current, which is a probability for majority carriers to overcome the potential barrier at the interface depending on the temperature.

Point B (0 V, light): The photocurrent starts to become blocked at a reverse bias. The net current is small and equal to the photocurrent at point B. The barrier height for electrons are reduced due to electron-hole pairs generated by the photons with higher energy than the band gap of Zn(O,S). Since the band gap of Zn(O,S) is high, the barrier height for electrons is still high due to lack of high energy photons, thus most free electrons are trapped in the deep-level defects. This leads to small photocurrent.

Point C and D (190 mV, light): In addition to photocurrent, there is also diode current and shunt current. Therefore, the net current decreases from point C to D suddenly due to impeded photo-current collection. This leads to kinked J-V curve and significantly decreases the FF of the device.

Point E (450 mV, light and dark): I–V crossover occurs due to voltage dependence photocurrent. Under illumination, the net electric field, which separates the photo-generated carriers, vanishes at the built-in potential. Built-in potential depends on barrier height (Φ). Since the barrier is reduced due to the electron-hole pairs generated by the photons, built-in potential under illumination is lower than that of dark. As a result, dark and light J-V curves are crossover. The net photocurrent becomes zero at the built-in potential where crossover occurs since there is an equal probability for photo-generated carriers two diffuse to either of the two contacts.

Point F (885 mV, dark): When the cell is biased to larger voltage, electrons can pass through the spike.

Point G (885 mV, light): At larger bias, direction of the electric field and photocurrent change. Therefore, more voltage must be consumed for point F to have the same current as point G under light.

6.2. Effect Sulfurization Time and the Thickness of Bottom Cu Layer in CZTS Precursors to the J-V Curves

Figure 6.4. and Figure 6.5. show the dark J–V and light J–V curves of devices fabricated using Type 1 and Type 2 CZTS absorber layers, respectively. In order to prevent confusion, we called Type 1 and Type 2 devices according to their absorber layers. Minutes in the graphs represents the sulfurization times of the CZTS absorber layers. We observed strong dependence of device performances on both sulfurization time and the thickness of bottom Cu layer in CZTS precursors. As it can be seen, short circuit current density (J_{sc}), open circuit voltage (V_{oc}) and efficiency (η) values are reduced with increasing sulfurization time. Moreover, Type 2 CZTS cells, which have high thickness of bottom Cu layer in CZTS precursors, have higher performance parameters at a certain sulfurization time.

As discussed above, impeded photo-current collection due to high barrier height has a negative effect on the device performance due to reduced fill factor (FF) and short circuit current density (J_{sc}). There are also many other factors that are critical for the performance of CZTS solar cells such as series resistance (R_s), shunt resistance (R_{sh}), secondary phases in the bulk CZTS, ordering level of CZTS, carrier concentration and carrier mobility. There are many reports for extracting the R_s and R_{sh} from the both dark and light J–V characteristics (Neuschitzer et al., 2015). In fact, light J-V measurements are commonly used to evaluate the electrical characteristics of solar cells. Light J-V measurements may provide more reliable information about loss parameters than dark-forward J–V characteristics due to the dependence of the series and shunt resistance on light-sensitive defect states inside the buffer, recombination velocity and device temperature (Chander, Purohit, Sharma, Nehra, & Dhaka, 2015; Neuschitzer et al., 2015; Sissoko & Mbodji, 2011). However, since light J-V curves of fabricated solar cells show strong distortion, dark J-V curves were employed to determine these loss parameters of the cells (Namin, Jivacate, Chenvidhya, Kirtikara, & Thongpron, 2012). R_s was evaluated from a slope of dark J-V at high bias in the first quadrant and R_{sh} was derived from a slope of dark J-V at zero voltage (Table 6.2.).

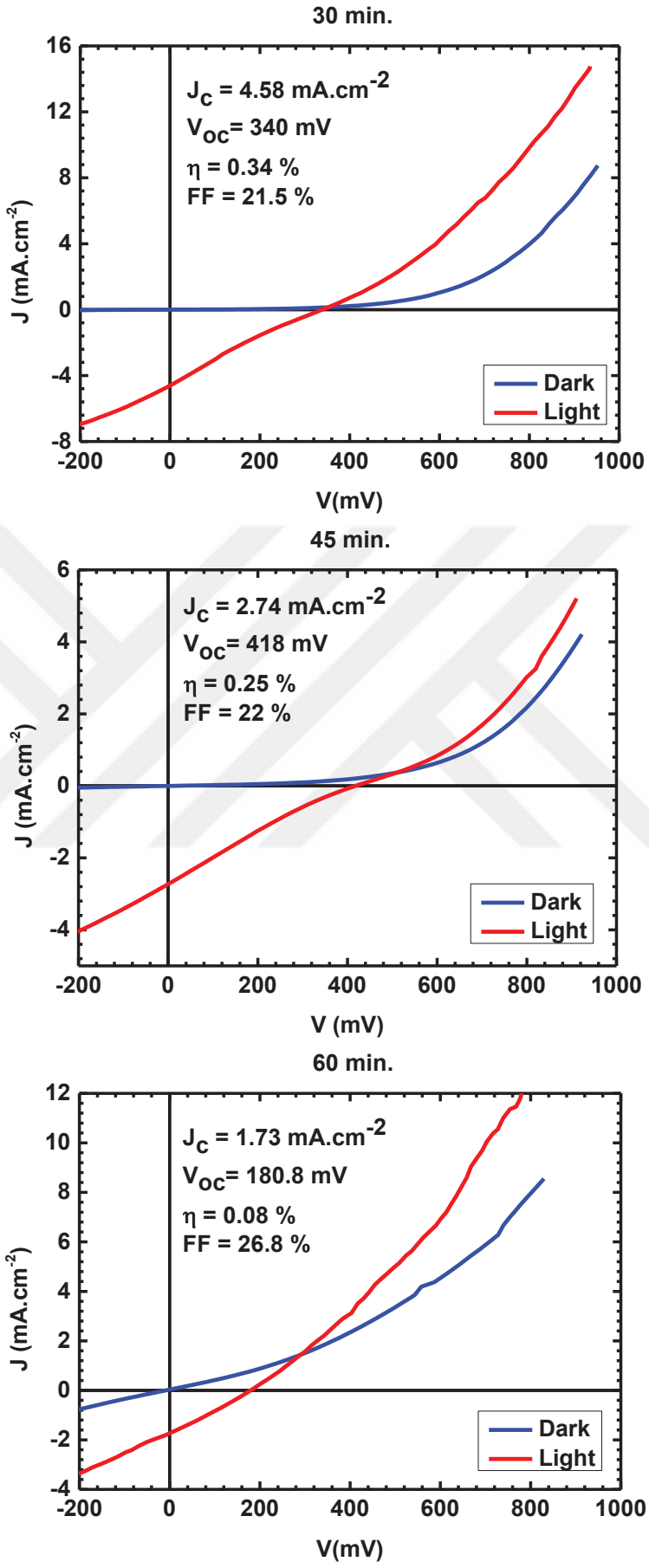

Figure 6.4. J-V curves of Type 1 CZTS solar cells.

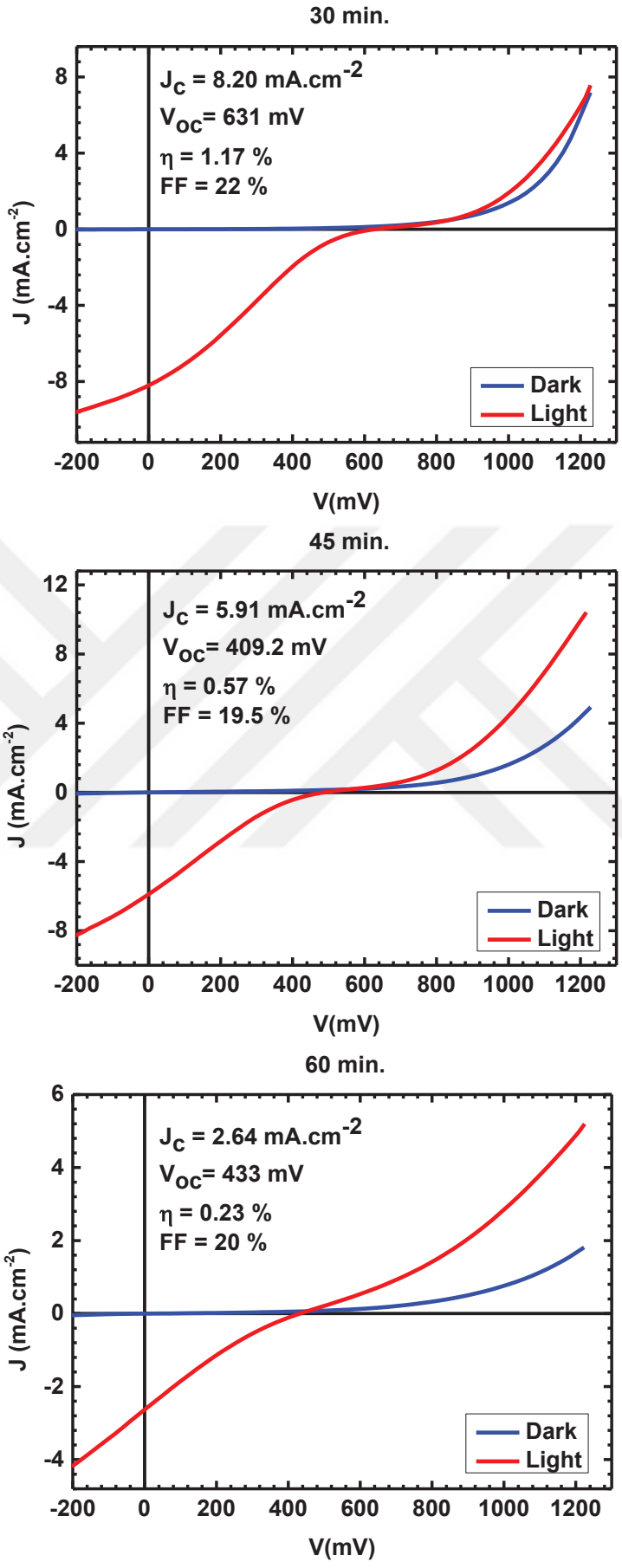

Figure 6.5. J-V curves of Type 2 CZTS solar cells.

Tablo 6.1. Parameters of the best solar cells obtained from CZTS absorber layer grown from precursors with Type 1 and Type 2.

		Sulfurization time of CZTS (min)	J_{sc} (mA.cm^{-2})	V_{oc} (mV)	P_{max} (µW)	Area (cm^2)	η (%)	FF (%)
Type 1 Devices	Device A	30	4.58	340.0	49.26	0.147	0.34	21.5
	Device B	45	2.74	418.0	71.77	0.285	0.25	22.0
	Device C	60	1.73	180.8	25.18	0.300	0.08	26.8
Type 2 Devices	Device D	30	8.20	631.0	101.39	0.086	1.17	22.6
	Device E	45	5.91	490.2	49.80	0.088	0.57	19.5
	Device F	60	2.64	433.0	33.89	0.148	0.23	20.0

Tablo 6.2. R_{sh} and R_s values of Type 1 and Type 2 devices.

		Sulfurization time of CZTS (min)	R_{sh} (kΩ)	R_s (Ω)
Type 1 Devices	Device A	30	61.67	215.56
	Device B	45	14.73	246.98
	Device C	60	0.83	333.33
Type 2 Devices	Device D	30	163.06	198.21
	Device E	45	54.69	701.28
	Device F	60	0.66	1225.16

For both Type 1 and Type 2 CZTS solar cells, R_s increases and R_{sh} decreases as the sulfurization duration increases. The R_s arises from resistances of bulk semiconductors and contacts. Zn(O,S) buffer layers is not responsible for the enhancement in the R_s with sulfurization duration because the process condition are the same for this layers. The increasing R_s of our samples may be attributed to high resistivity of the CZTS and the formation of a MoS_2 layer at the Mo/CZTS interface (Mitzi, Gunawan, Todorov, Wang, & Guha, 2011; Scragg et al., 2013). Unfortunately, we didn't measure resistivity values of the CZTS films.

Formation of MoS_2 can occur through decomposition reactions at CZTS/Mo and/or during the CZTS sulfurization process which supply S (Barkhouse et al., 2012; S Schorr, 2007). Since MoS_2 is indirect semiconductor with a low band gap of 1.29 eV (Mak, Lee, Hone, Shan, & Heinz, 2010), it reduces the V_{oc} of CZTS solar cells (Shin, Zhu, Bojarczuk, Jay Chey, & Guha, 2012). CZTS/Mo decomposition reactions were explained by Scragg, et al. 2012 (Scragg, Watjen, et al., 2012) (see section 3.2). Decomposition at CZTS/Mo interface could enhance recombination by the formation of

secondary phases (SnS, Cu_2S, ZnS). These secondary phases segregated at the Mo/CZTS interface potentially cause losses of V_{oc}, J_{sc} and FF in the CZTS device. While secondary phases with lower band gap may reduce the V_{oc} and FF, secondary phases with higher band gap may reduce the J_{sc} and FF. Besides secondary phases formation, an over-thick MoS_2 layer may deteriorate the electrical contact and increases RS. Side view SEM images of the Type 2 samples were given in Figure 6.6. to show the formation and evolution of a MoS_2 interfacial layer over the sulfurization time. The thickness of the MoS_2 phase is 59, 126 and 225 nm for sulfurization durations of 30, 45 and 60 min, respectively. This indicate that sulfurization for longer durations at high temperature (550 °C) trigger the formation of MoS_2. Moreover, voids results from out-diffusion of elements and the decomposition of CZTS films were observed near the CZTS/Mo interface. Reduced adhesion of CZTS on MoS_2 due to high amount of voids can be seen at high sulfurization duration. These voids may act as recombination centers, lower J_{sc} and V_{oc}. Moreover, they can act as shunting paths and decrease the shunt resistance (Liu et al., 2015). These indicate that low sulfurization time is favorable to obtain MoS_2 layer with low thickness and restrict to void formation.

Many methods to reduce the thickness of MoS_2 layer in CZTS solar cell have been proposed. These methods include deposition of thin intermediate layer between Mo and CZTS such as Ag, TiN and ZnO to prevent diffusion of S to Mo back. These intermediate layers led to significant improvements in performance of solar cells. Additionally, effect of intermediate thin MoO_2 layer was investigated for CZTSe and CZTS solar cells (Yang et al., 2015). Suppression of MoS_2 formation due to increase in oxygen content in the Mo layer observed in these works. However, this layer may also create a resistive barrier to carrier transport due to its band gap of 2.83 eV (Dukstiene, Sinkeviciute, & Guobiene, 2012) and degrade the device performance. Therefore, we have no comment on MoO_2 phase observed in XRD analyses of Type 2 samples.

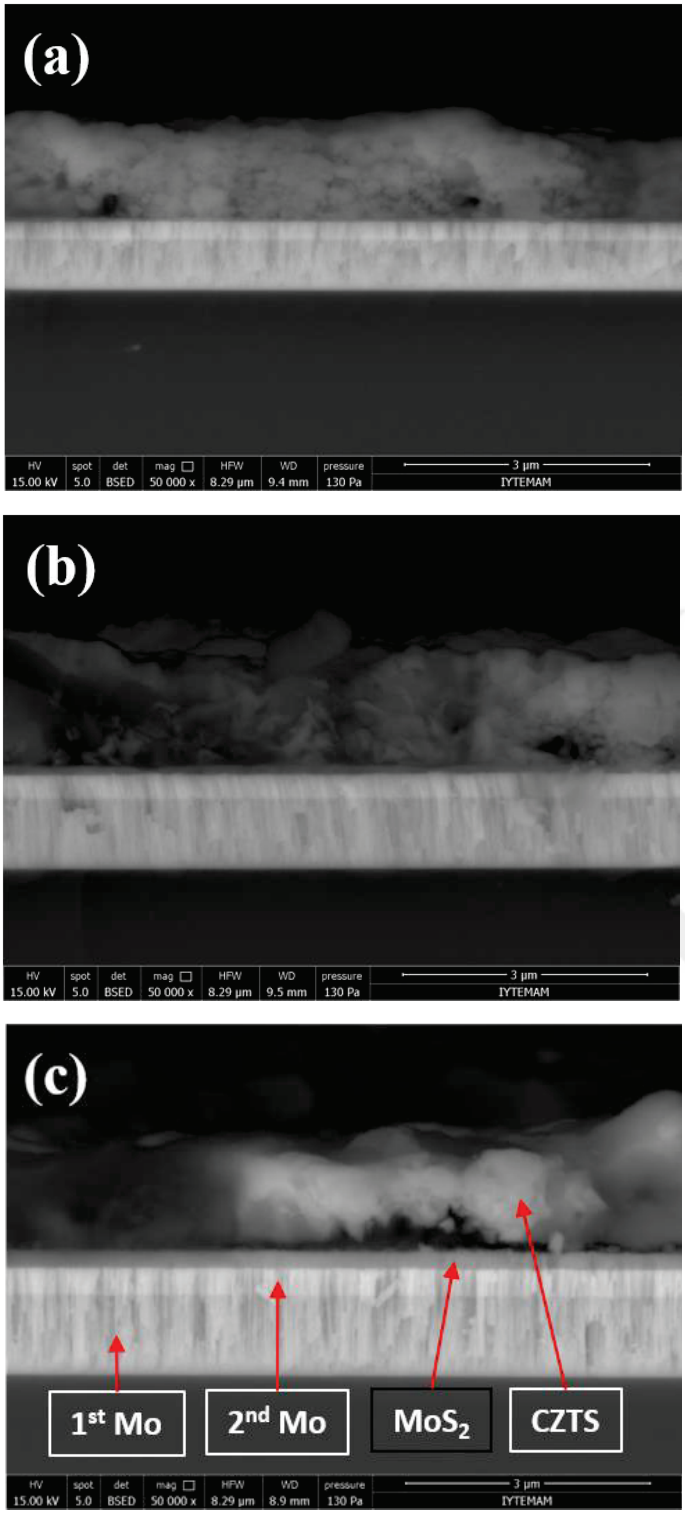

Figure 6.6. Cross-section image of (a) Sample D (b) Sample E (c) Sample F showing evolution of MoS_2 at the Mo/CZTS interface.

Although the presence of MoS_2 at Mo/CZTS interface mainly increase R_s of the device, this phase should not have a major effect on the lower J_{sc} values of Type 1 cells in comparison with Type 2 cells. Most probable reason of the low J_{sc} is defect and/or impurities present in the CZTS absorber layer, which also decreases shunt resistance.

Due to Cu_{Zn} and Zn_{Cu} antisite defects, the change in the ordering level depending on thickness of Cu adjacent to Sn was observed in Raman spectroscopy analyses. Timmo, et al. 2016 suggest that improved ordering increase the band gap of the CZTS and result in enhancement of V_{oc}. (Timmo et al., 2016). It should be noted that the change in the band gap energy ΔE_g is followed by change in V_{oc} for an ideal solar cell (Krämmer et al., 2015). Additionally, high densities of antisite disorder (Cu_{Zn}, Zn_{Cu}) lead to band tailing, thus causing reduction of V_{oc} (Gokmen, Gunawan, Todorov, & Mitzi, 2013). Improvement of V_{oc} due to increased Cu-Zn ordering has been also observed for $Cu_2ZnSnSe_4$ (Rey et al., 2016) and $Cu_2ZnSn(S,Se)_4$ (Krämmer et al., 2015). According to these works, we may also attribute the enhancement of V_{oc} for Type 2 devices to the improved ordering of the samples. Among all samples, the highest degree of ordering in CZTS was obtained for Sample D which has also highest V_{oc}.

One of the most important limitation to device performance is caused by the presence of secondary phases. Degraded device efficiencies due to increasing sulfurization time may be explained by the phases detected during CZTS absorber layer characterization.

Possible presence of ZnS and CTS phases realized by XRD and Raman analyses for CZTS films with Type 1 structure. The presence of ZnS can give insulator regions in the CZTS due to its the high band gap (3.6 eV). It doesn't influence the V_{oc}, but can cause an increase in the series resistance because of its low conductivity. ZnS segregations can both reduce the active area and inhibit the current conduction in the absorber, reduces the device performance. Large spikes for both the conduction and valence bands (above 0.8 eV) were observed at interfaces between CZTS and and ZnS (Bao, 2014). Such a high barrier may block the flow of photo-excited carriers (electrons), reduce the photo current and block the flow of majority carriers (holes) (Bao, 2014). On the other hand, this high barrier may reduce the interface recombination. Cu_2SnS_3 (CTS), which is a p-type semiconductor with metallic character, can reduce the E_g and increase the conductivity of the device by forming a solid solution with CZTS. Cliff conformation occurs for the band alignment of CTS/CZTS interface, CBM and VBM of CTS locate in the forbidden energy region of CZTS (Bao, 2014). Both of minority and majority carriers flow to CTS due to its small bandgap, thus it acts as a recombination center, reducing both I_{sc} and V_{oc}. Tin disulfide (SnS_2) observed in SEM analyses of Type 1 samples is a n-type semiconductor with a direct bandgap of 2.2 eV. This secondary phase can act as an insulator, if it is

present in larger quantities it is also possible to form a second diode with a polarity opposite to CZTS, which prevents the carrier collection and reduces the fill factor.

Presence of SnO_2 and ZnO phases observed in Type 1 and Type 2 CZTS films, respectively. These oxides were found to be locate at the grain boundaries. In fact, SnO_2 phase located at the grain boundaries is considered to be passivate grain boundary recombination sites, thus the presence of SnO_2 was correlated with high device performance (Ge et al., 2016; Sardashti et al., 2015). For CZTSSe absorber layer, VBO of 1.9–2.1 eV between SnO_2 and CZTSSe was found (Sardashti et al., 2015). This large VBO may provide a robust barrier to hole transport and thereby minimizing the electron–hole recombination at the interface. In another work, two types of grain boundaries were observed, one of them contain a nanometer-thick intergranular oxide layer while the other has a crystal−crystal interface without any intergranular phases (Kim et al., 2016). For the grain boundary with crystal−crystal interface, it was observed that Se substitute by oxygen to form Cu2ZnSn(Se_3,O). It was proposed that while the formation of Cu2ZnSn(Se_3,O) provides a robust barrier to hole transport and minimize the electron–hole recombination at the grain boundaries, formation of intergranular oxide layers cannot act as an active carrier-generation layer and they should be suppressed (Kim et al., 2016). We believe that there is a critical value for the oxygen substitution, when this value is exceeded the amount of intergranular oxide phases increases. Since these oxide phases have large bandgaps (E_g(ZnO)=3.2 eV, E_g(SnO_2)=3.8 eV), presence of these oxides may give insulator regions in the CZTS and inhibit the current conduction in the absorber, reduces the device performance. Moreover, high amount of these oxides leads to high densities of antisite disorder, thus causing reduction of V_{oc}. Additionally, presence of SnO_2 may provide a high barrier (0.6-0.8 eV for CZTSe) and such a high barrier may block the flow of photo-excited carriers (electrons).

All this phases present in CZTS absorbers explains how thickness of bottom Cu layer in CZTS precursors affect device performances. The high degree of ordering and complete CZTS formation with less secondary phases for Type 2 absorber layers with thicker Cu layer adjacent to Sn layer in precursors provides better device performances. Among these phases, formation and evolution with increasing sulfurization time is only observed for the MoS_2, ZnO and SnO_2 phases. Therefore, degradation of the device performances with increasing sulfurization time is mainly attributed to formation and evolution of the MoS_2 and SnO_2 phases for Type 1 devices and MoS_2 and ZnO for Type 2 devices with increasing sulfurization time. Reduction of J_{sc} with increasing sulfurization

time can be results from the evolution of the ZnO and SnO_2 phases and reduction of V_{oc} with increasing sulfurization time can be results from the evolution of the MoS_2 and voids. As in EDX, XRD and Raman analyzes, J-V results also confirms that Type 2 structure and 30 min sulfurization of CZTS precursors is the best to have better device performances.

CHAPTER 7

CONCLUSION

At the beginning of this research, several goals were set to be achieved. The main goal was to develop relatively new, rapidly developing Cu_2ZnSnS_4 thin film solar cells. In order to reach our objective, all of the thin films used in the CZTS device fabrication were investigated to identify the impact of the growth conditions on film properties, optimize the growth process and apply the developed films in photovoltaic devices to optimize growth conditions on the properties of these thin films and to apply these films to CZTS devices. Moreover, we have focused on fabrication of CZTS solar cells using only the magnetron sputtering technique for all thin films in the solar cell structure to provide easy adaptation to large-scale and reproducible manufacturing of the CZTS solar cells.

Aluminum doped zinc oxide (AZO) is currently most used material for making transparent conducting electrodes. A high deposition temperature above 300 $^{\circ}C$ is necessary to get a desired TCO property for AZO. However, a room temperature deposition process is required to avoid inter-diffusion between the layers of a solar cell. To get a desired TCO property for AZO thin film deposited at room temperature, we investigated the effect of the location of the samples on the sample holder and rotation speed of the sample holder during the sputtering on the properties of the AZO films deposited at room temperature. XRD measurements of AZO films indicates all films are under compressive stresses which indicates many of Al^{3+} ions cations sit in the films as an interstitial ion. It is observed that stress in the films decreases when the substrate position with respect to the target axis increases. Moreover, small reduction of the stress in the films with increasing rotation speed was observed. For the AZO films placed under the target, a broad single peak in the XRD spectra was observed which results from the peak overlapping of the AZO and the Al_2O_3 peaks. Formation of Al_2O_3 is attributed to direct bombardment of high energetic O atoms on the surface which combine with Al atoms to form aluminum oxides and limit the doping effect. When the sample placed away from the target, sputtered particles and argon ions collide frequently, their energy is reduced while traveling to the substrate. The films are protected from direct

bombardment of high energetic negative ions on the surface and the bombardment is significantly reduced with the off-center configuration. From the Raman and transmission measurements, we concluded that carrier concentration of the films increases for the samples in off-center configurations and rotating samples since defects induced by the bombardment of high energetic negative ions is significantly reduced for these samples. Resistivity values of AZO films were measured by the four-point. Strong enhancement of the resistivity for the substrate position facing the target were observed due to excess of Al and O atoms which form non-conducting Al_2O_3 clusters in the films, acting as carrier traps rather than electron donors. It is observed that resistivity of the films decreases when the substrate position with respect to the target axis increases. In addition, we further observed that as the sample holder rotated resistivity of the films decreases regardless of sample position. Here, we demonstrate that the crystallinity and resistivity of the AZO films fabricated at room temperature can be improved by off-center deposition and rotating the sample holder during sputtering. The lowest resistivity value was found to be $2\ 10^{-3}$ Ω.cm with 88 % average transmission in the visible range for the AZO films 6.5 cm away from the target axis rotating at 6.3 rpm.

Currently the standard technique of producing CZTS solar cells is to use cadmium sulphide (CdS) grown by chemical bath deposition (CBD) as buffer layer. Although yielding the best device performance, there are some debates on the fundamental issues with this buffer layer because it contains toxic cadmium. Among the different toxic free alternatives for CdS, we focused on Zinc oxysulfide Zn(O,S) buffer layer which is an excellent candidate for a wide band gap buffer layer because it can form a favorable CBO with various absorber layers by tuning oxygen flow during sputtering. So far, very few experimental attempts have been made to investigate the performance of CZTS/ Zn(O,S) devices. We investigate the effect of the sulfur concentration on the properties of Zn(O,S) thin films using EDX, XRD, SEM, Raman spectroscopy and transmission analyses. We showed that key parameters such as energy gap and crystal structure of the Zn(O,S) thin films can be tuned by changing the sulfur concentrations of the films. Band gap of the Zn(O,S) films was tuned from 2.92 to 3.27 eV by O_2 gas flow control during deposition. We succeed substitute conventionally used CdS buffer layer with environmentally friendly alternative Zn(O,S) buffer layer in CZTS solar cells.

Sulfurization duration is one of the most important parameter for the formation of the CZTS absorber material with desired stoichiometry and optimal crystalline quality which play important roles in solar cell performance. CZTS films based on a stacked

precursor (Cu/Sn/Zn/Cu) were prepared. The effect of sulfurization time and the thickness of top and bottom Cu layer in precursors on the properties of CZTS thin films were investigated.

Although thicknesses of the Cu, Zn, and Sn films were adjusted to get Cu-poor and Zn-rich composition, we could not succeed both Cu-poor and Zinc-rich composition for any of the samples. We attributed this behavior to Sn and S loss for the precursors having thinner Cu bottom layer and to Zn loss for the precursors having thicker Cu bottom layer. From XRD and Raman spectroscopy characterizations, we verified our assumption. The formation of SnO_2 phase was observed for the precursors having thinner Cu bottom layer which results from removing the Sn from the CZTS thin film and evidence of Sn loss in CZTS. The presence of ZnO phase was observed for the precursors having thicker Cu bottom layer and thin Cu cap layer which results from removing the Zn from the CZTS thin film and evidence of Zn loss in CZTS. Evolution of SnO_2 and ZnO interfacial phases over the sulfurization time was observed seen in the XRD graphs. The peak intensity of these oxide phases increases as the sulfurization time increases which indicates that sulfurization for longer durations at high temperature (550 °C) trigger the formation of these oxides. In the Raman spectra of the precursors having thinner Cu bottom layer, we observed shifting of the most intense peak (A mode of kesterite with disordered structure) towards lower frequencies (328 - 330 cm^{-1}) which is due to the existence of disorder effects caused by the high concentration of Cu_{Zn} and Zn_{Cu} antisite defects in the CZTS films. In the Raman spectra of the precursors having thicker Cu bottom layer, we observed that the most intense peaks lie between 337- 339 cm^{-1} and they are attributed to A mode of KS with ordered structure. This indicates the reduced amount of defects compared to samples having thinner Cu bottom layer. Raman spectra of samples having thinner Cu bottom layer also gave a general broadening due to the reduction in phonon correlation length caused by disorder (defects). Therefore, a special attention was given for the range 250-450 nm since main Raman modes of CZTS and many secondary phases lies in this range. In order to clarify the presence of the peaks was not experimentally resolved in our spectra, we fitted the experimental spectra. Tetragonal-CTS, Cubic-CTS and Cubic-ZnS are the possible secondary phases may present in the CZTS films according to the deconvolution results. Both disordered structure and remaining CTS and ZnS phases implies incomplete formation of CZTS.

Based on SEM, EDX, XRD and Raman analyzes, we concluded that 1) if the thick Cu layer is not adjacent to Sn layer, Cu cannot bound Sn by the formation of Cu_2SnS_3

which is reactant to produce CZTS with ZnS, and Sn loss increases, 2) when thick Cu layer is not adjacent to Sn, it's difficult to form Cu_2SnS_3 to produce CZTS, and as a consequence formation of CZTS is restricted, films exhibit disordered structure with many secondary phases, 3) thin Cu cap layer cannot prevent the Zn loss, while the Sn loss is prevented by thick Cu layer at the bottom of the stack since Sn is bounded by the formation of Cu_2SnS_3, 4) the sulfurization time should be lowered to avoid the Sn an Zn losses and formation of the oxide phases.

CZTS solar cell devices fabricated in this work suffer from low fill factor (FF) and short circuit current density (J_{sc}). Open circuit voltage (V_{oc}) values are comparable to that of best CZTS devices reported up to now. While the dark J-V characteristics indicate the formation of high quality junction between the CZTS absorbers and Zn(O,S) buffers with a sulfur concentration of Xs= 0.53, J-V characteristics show strong distortion under light which cause low FF and J_{sc} values. J-V distortion, the reduced current density and the reduced fill factors was explained by the barriers at the hetero-junctions. Moreover, we also observed strong dependence of device performances on both sulfurization time and the thickness of Cu layer adjacent to Sn in CZTS absorber. We observed that critical current density (J_{sc}), open circuit voltage (V_{oc}) and efficiency values are reduced with increasing sulfurization time. Degradation of the device performances with increasing sulfurization time was mainly attributed to formation and evolution of the MoS_2 and SnO_2 phases with increasing sulfurization time for the samples having low thickness of bottom Cu layer in CZTS precursors and to formation and evolution of the MoS_2 and ZnO with increasing sulfurization time for the samples having high thickness of bottom Cu layer in CZTS precursors. Reduction of J_{sc} with increasing sulfurization time can be results from the evolution of the ZnO and SnO_2 phases and reduction of V_{oc} with increasing sulfurization time can be results from the evolution of the MoS_2 and voids. Moreover, CZTS cells, which have high thickness of bottom Cu layer in CZTS precursors, have higher performance parameters due to high degree of ordering and complete CZTS formation with less secondary phases for the absorber layers. As in EDX, XRD and Raman analyzes, J-V results also confirms that thicker Cu layer should be adjacent to Sn layer in precursors and low sulfurization time of precursors are needed to have better device performances. The best device based on CZTS films sulfurized for 30 minutes and have thicker Cu layer adjacent to Sn layer in precursors yielded a power conversion efficiency of 1.17% with a V_{oc}= 631.0 mV, J_{sc}= 8.20 mA/cm^2 and FF= 22.6 %.

REFERENCES

Aktaruzzaman, A., Sharma, G., & Malhotra, L. (1991). Electrical, optical and annealing characteristics of ZnO: Al films prepared by spray pyrolysis. *Thin Solid Films, 198*(1-2), 67-74.

Alim, K. A., Fonoberov, V. A., Shamsa, M., & Balandin, A. A. (2005). Micro-Raman investigation of optical phonons in ZnO nanocrystals. *Journal of Applied Physics, 97*(12), 124313.

Altosaar, M., Raudoja, J., Timmo, K., Danilson, M., Grossberg, M., Krustok, J., & Mellikov, E. (2008). $Cu_2Zn_{1-x}Cd_xSn(Se_{1-y}S_y)_4$ solid solutions as absorber materials for solar cells. *physica status solidi (a), 205*(1), 167-170.

Ashrafi, A. A., Ueta, A., Avramescu, A., Kumano, H., Suemune, I., Ok, Y.-W., & Seong, T.-Y. (2000). Growth and characterization of hypothetical zinc-blende ZnO films on GaAs (001) substrates with ZnS buffer layers. *Applied Physics Letters, 76*(5), 550-552.

Avellaneda, D., Nair, M., & Nair, P. (2009). Photovoltaic structures using chemically deposited tin sulfide thin films. *Thin Solid Films, 517*(7), 2500-2502.

Babu, G. S., Kumar, Y. K., Bhaskar, P. U., & Vanjari, S. R. (2010). Effect of Cu/(Zn+ Sn) ratio on the properties of co-evaporated $Cu_2ZnSnSe_4$ thin films. *Solar Energy Materials and Solar Cells, 94*(2), 221-226.

Bag, S., Gunawan, O., Gokmen, T., Zhu, Y., Todorov, T. K., & Mitzi, D. B. (2012). Low band gap liquid-processed CZTSe solar cell with 10.1% efficiency. *Energy & Environmental Science, 5*(5), 7060-7065.

Bai, Z., Yang, J., & Wang, D. (2011). Thin film CdTe solar cells with an absorber layer thickness in micro-and sub-micrometer scale. *Applied Physics Letters, 99*(14), 143502.

Bao, W. (2014). *First Principles Study on Band Offsets at the Cu_2ZnSnS_4-Based Heterointerfaces.* (Ph.D. Dissertation), Nagoya Institute of Technology, Nagoya, JAPAN.

Bär, M., Schubert, B.-A., Marsen, B., Wilks, R. G., Pookpanratana, S., Blum, M., . . . Weinhardt, L. (2011). Cliff-like conduction band offset and KCN-induced recombination barrier enhancement at the CdS/Cu_2ZnSnS_4 thin-film solar cell heterojunction. *Applied Physics Letters, 99*(22), 222105.

Barkhouse, D. A. R., Haight, R., Sakai, N., Hiroi, H., Sugimoto, H., & Mitzi, D. B. (2012). Cd-free buffer layer materials on $Cu_2ZnSn(S_xSe_{1-x})_4$: Band alignments with ZnO, ZnS, and In_2S_3. *Applied Physics Letters, 100*(19), 193904.

Bates, C. H., White, W. B., & Roy, R. (1962). New high-pressure polymorph of zinc oxide. *Science, 137*(3534), 993-993.

Bergman, L., Dutta, M., Balkas, C., Davis, R. F., Christman, J. A., Alexson, D., & Nemanich, R. J. (1999). Raman analysis of the E1 and A1 quasi-longitudinal optical and quasi-transverse optical modes in wurtzite AlN. *Journal of Applied Physics, 85*(7), 3535-3539.

Bhattacharya, R., Ramanathan, K., Gedvilas, L., & Keyes, B. (2005). Cu(In, Ga)Se_2 thin-film solar cells with ZnS(O, OH), Zn–Cd–S(O, OH), and CdS buffer layers. *Journal of Physics and Chemistry of Solids, 66*(11), 1862-1864.

Bird, R. E., Hulstrom, R. L., & Lewis, L. (1983). Terrestrial solar spectral data sets. *Solar Energy, 30*(6), 563-573.

Brafman, O., & Mitra, S. (1968). Raman effect in wurtzite-and zinc-blende-type ZnS single crystals. *Physical Review, 171*(3), 931.

Bragg, W. H., & Bragg, W. L. (1913). The reflection of X-rays by crystals. *Proceedings of the Royal Society of London. Series A, Containing Papers of a Mathematical and Physical Character, 88*(605), 428-438.

Buffière, M., Harel, S., Arzel, L., Deudon, C., Barreau, N., & Kessler, J. (2011). Fast chemical bath deposition of Zn(O, S) buffer layers for Cu(In, Ga)Se_2 solar cells. *Thin Solid Films, 519*(21), 7575-7578.

Buffière, M., Harel, S., Guillot-Deudon, C., Arzel, L., Barreau, N., & Kessler, J. (2015). Effect of the chemical composition of co-sputtered Zn(O, S) buffer layers on Cu(In, Ga)Se_2 solar cell performance. *physica status solidi (a), 212*(2), 282-290.

Burstein, E. (1954). Anomalous optical absorption limit in InSb. *Physical Review, 93*(3), 632.

Cai, Y., Liu, W., He, Q., Zhang, Y., Yu, T., & Sun, Y. (2010). Influence of negative ion resputtering on Al-doped ZnO thin films prepared by mid-frequency magnetron sputtering. *Applied Surface Science, 256*(6), 1694-1697.

Catlow, C., Guo, Z., Miskufova, M., Shevlin, S., Smith, A., Sokol, A., . . . Woodley, S. (2010). Advances in computational studies of energy materials. *Philosophical Transactions of the Royal Society of London A: Mathematical, Physical and Engineering Sciences, 368*(1923), 3379-3456.

Cebulla, R., Wendt, R., & Ellmer, K. (1998). Al-doped zinc oxide films deposited by simultaneous rf and dc excitation of a magnetron plasma: relationships between plasma parameters and structural and electrical film properties. *Journal of Applied Physics, 83*(2), 1087-1095.

Chan, C., Lam, H., & Surya, C. (2010). Preparation of Cu_2ZnSnS_4 films by electrodeposition using ionic liquids. *Solar Energy Materials and Solar Cells, 94*(2), 207-211.

Chander, S., Purohit, A., Sharma, A., Nehra, S., & Dhaka, M. (2015). Impact of temperature on performance of series and parallel connected mono-crystalline silicon solar cells. *Energy Reports, 1*, 175-180.

Chen, Q., Cheng, S., Zhuang, S., & Dou, X. (2012). Cu_2ZnSnS_4 solar cell prepared entirely by non-vacuum processes. *Thin Solid Films, 520*(19), 6256-6261.

Chen, S., Gong, X., Walsh, A., & Wei, S.-H. (2010). Defect physics of the kesterite thin-film solar cell absorber Cu_2ZnSnS_4. *Applied Physics Letters, 96*(2), 021902.

Chen, S., Gong, X. G., Walsh, A., & Wei, S.-H. (2009). Crystal and electronic band structure of Cu_2ZnSnX_4 (X=S and Se) photovoltaic absorbers: First-principles insights. *Applied Physics Letters, 94*(4), 041903.

Chen, S., Walsh, A., Gong, X. G., & Wei, S. H. (2013). Classification of lattice defects in the kesterite Cu_2ZnSnS_4 and $Cu_2ZnSnSe_4$ earth-abundant solar cell absorbers. *Advanced Materials, 25*(11), 1522-1539.

Chen, S., Wang, L.-W., Walsh, A., Gong, X., & Wei, S.-H. (2012). Abundance of Cu_{Zn}+Sn_{Zn} and 2Cu_{Zn}+Sn_{Zn} defect clusters in kesterite solar cells. *Applied Physics Letters, 101*(22), 223901.

Chen, S., Yang, J.-H., Gong, X.-G., Walsh, A., & Wei, S.-H. (2010). Intrinsic point defects and complexes in the quaternary kesterite semiconductor Cu_2ZnSnS_4. *Physical Review B, 81*(24), 245204.

Cheng, Y., Jin, C., Gao, F., Wu, X., Zhong, W., Li, S., & Chu, P. K. (2009). Raman scattering study of zinc blende and wurtzite ZnS. *Journal of Applied Physics, 106*(12), 123505.

Chopra, K., & Das, S. (1983). Thin film solar cells: New York: Plenum Press.

Conti, J., Holtberg, P., Doman, L., Smith, K., Sullivan, J., Vincent, K., . . . Kearney, D. (2011). International energy outlook 2011. *US Energy Information Administration, Technical Report No. DOE/EIA-0484*.

Contreras, M. A., Tuttle, J., Gabor, A., Tennant, A., Ramanathan, K., Asher, S., . . . Noufi, R. (1996). High efficiency graded bandgap thin-film polycrystalline Cu(In, Ga)Se_2-based solar cells. *Solar Energy Materials and Solar Cells, 41*, 231-246.

Cui, Y., Zuo, S., Jiang, J., Yuan, S., & Chu, J. (2011). Synthesis and characterization of co-electroplated Cu_2ZnSnS_4 thin films as potential photovoltaic material. *Solar Energy Materials and Solar Cells, 95*(8), 2136-2140.

Damen, T. C., Porto, S., & Tell, B. (1966). Raman effect in zinc oxide. *Physical Review, 142*(2), 570.

Deshpande, N., Sagade, A., Gudage, Y., Lokhande, C., & Sharma, R. (2007). Growth and characterization of tin disulfide (SnS_2) thin film deposited by successive ionic layer adsorption and reaction (SILAR) technique. *Journal of Alloys and Compounds, 436*(1), 421-426.

Deulkar, S. H., Huang, J.-L., & Neumann-Spallart, M. (2010). Zinc Oxysulfide Thin Films Grown by Pulsed Laser Deposition. *Journal of Electronic Materials, 39*(5), 589-594.

Dhakal, T. P., Peng, C. Y., Tobias, R. R., Dasharathy, R., & Westgate, C. R. (2014). Characterization of a CZTS thin film solar cell grown by sputtering method. *Solar Energy, 100*, 23-30.

Dona, J., & Herrero, J. (1997). Dependence of Electro-optical Properties on the Deposition Conditions of Chemical Bath Deposited CdS Thin Films. *Journal of the Electrochemical Society, 144*(11), 4091-4098.

Dukstiene, N., Sinkeviciute, D., & Guobiene, A. (2012). Morphological, structural and optical properties of MoO2 films electrodeposited on SnO_2 | glass plate. *Open Chemistry, 10*(4), 1106-1118.

EIA, U. (2011). International energy outlook. *US Energy Information Administration, Washington, DC, USA*.

Eicke, A., Ciba, T., Hariskos, D., Menner, R., Tschamber, C., & Witte, W. (2013). Depth profiling with SNMS and SIMS of Zn(O, S) buffer layers for $Cu(In,Ga)Se_2$ thin-film solar cells. *Surface and Interface Analysis, 45*(13), 1811-1820.

El Manouni, A., Manjón, F., Mollar, M., Marí, B., Gómez, R., López, M., & Ramos-Barrado, J. (2006). Effect of aluminium doping on zinc oxide thin films grown by spray pyrolysis. *Superlattices and Microstructures, 39*(1), 185-192.

Ellmer, K., Klein, A., & Rech, B. (2008). *Transparent Conductive Zinc Oxide: Basics and Applications in Thin Film Solar Cells.*: Springer.

Ennaoui, A., Lux-Steiner, M., Weber, A., Abou-Ras, D., Kötschau, I., Schock, H.-W., . . . Hock, R. (2009). Cu_2ZnSnS_4 thin film solar cells from electroplated precursors: novel low-cost perspective. *Thin Solid Films, 517*(7), 2511-2514.

Ericson, T., Scragg, J. J., Hultqvist, A., Watjen, J. T., Szaniawski, P., Torndahl, T., & Platzer-Bjorkman, C. (2014). Zn(O, S) Buffer Layers and Thickness Variations of CdS Buffer for Cu_2ZnSnS_4 Solar Cells. *IEEE Journal of Photovoltaics, 4*(1), 465-469.

Fairbrother, A., Fourdrinier, L., Fontané, X., Izquierdo-Roca, V., Dimitrievska, M., Pérez-Rodríguez, A., & Saucedo, E. (2014). Precursor Stack Ordering Effects in $Cu_2ZnSnSe_4$ Thin Films Prepared by Rapid Thermal Processing. *The Journal of Physical Chemistry C, 118*(31), 17291-17298.

Fairbrother, A., García-Hemme, E., Izquierdo-Roca, V., Fontané, X., Pulgarín-Agudelo, F. A., Vigil-Galán, O., . . . Saucedo, E. (2012). Development of a selective chemical etch to improve the conversion efficiency of Zn-rich Cu_2ZnSnS_4 solar cells. *Journal of the American Chemical Society, 134*(19), 8018-8021.

Fairbrother, A., Izquierdo-Roca, V., Fontané, X., Ibáñez, M., Cabot, A., Saucedo, E., & Pérez-Rodríguez, A. (2014). ZnS grain size effects on near-resonant Raman scattering: optical non-destructive grain size estimation. *CrystEngComm, 16*(20), 4120-4125.

Ferekides, C. S., Marinskiy, D., Viswanathan, V., Tetali, B., Palekis, V., Selvaraj, P., & Morel, D. (2000). High efficiency CSS CdTe solar cells. *Thin Solid Films, 361*, 520-526.

Fernandes, P., Salomé, P., & Da Cunha, A. (2009). Precursors' order effect on the properties of sulfurized Cu_2ZnSnS_4 thin films. *Semiconductor Science and Technology, 24*(10), 105013.

Fernandes, P., Salomé, P., & Da Cunha, A. (2011). Study of polycrystalline Cu_2ZnSnS_4 films by Raman scattering. *Journal of Alloys and Compounds, 509*(28), 7600-7606.

Friedlmeier, T. M., Jackson, P., Bauer, A., Hariskos, D., Kiowski, O., Wuerz, R., & Powalla, M. (2015). Improved photocurrent in Cu(In, Ga)Se_2 solar cells: from 20.8% to 21.7% efficiency with CdS buffer and 21.0% Cd-free. *IEEE Journal of Photovoltaics, 5*(5), 1487-1491.

Frontier, S. (2014). Solar Frontier sets thin-film PV world record with 20.9% CIS cell. *Press Release, April*.

Ge, J., Yu, Y., Ke, W., Li, J., Tan, X., Wang, Z., . . . Yan, Y. (2016). Improved Performance of Electroplated CZTS Thin-Film Solar Cells with Bifacial Configuration. *ChemSusChem, 9*(16), 2149-2158.

Gokmen, T., Gunawan, O., Todorov, T. K., & Mitzi, D. B. (2013). Band tailing and efficiency limitation in kesterite solar cells. *Applied Physics Letters, 103*(10), 103506.

Gordon, R. G. (2000). Criteria for choosing transparent conductors. *MRS Bulletin, 25*(08), 52-57.

Green, M. A. (1982). Solar cells: operating principles, technology, and system applications. United States: Prentice-Hall, Inc.,Englewood Cliffs, NJ.

Green, M. A. (2007). Thin-film solar cells: review of materials, technologies and commercial status. *Journal of Materials Science: Materials in Electronics, 18*(1), 15-19.

Green, M. A., Emery, K., Hishikawa, Y., Warta, W., & Dunlop, E. D. (2016). Solar cell efficiency tables (version 47). *Progress in Photovoltaics: Research and Applications, 24*(1), 3-11.

GreenRhinoEnergy. (2013). Defining standard spectra for solar panels. Retrieved from http://www.greenrhinoenergy.com/solar/radiation/spectra.php.

Grimm, A., Just, J., Kieven, D., Lauermann, I., Palm, J., Neisser, A., . . . Klenk, R. (2010). Sputtered Zn(O, S) for junction formation in chalcopyrite-based thin film solar cells. *physica status solidi (RRL)-Rapid Research Letters, 4*(5-6), 109-111.

Grimm, A., Kieven, D., Klenk, R., Lauermann, I., Neisser, A., Niesen, T., & Palm, J. (2011). Junction formation in chalcopyrite solar cells by sputtered wide gap compound semiconductors. *Thin Solid Films, 520*(4), 1330-1333.

Guc, M., Neuschitzer, M., Hariskos, D., Bauer, A., Witte, W., Hempel, W., . . . Izquierdo-Roca, V. (2016). Raman scattering quantitative assessment of the anion composition ratio in Zn(O, S) layers for Cd-free chalcogenide-based solar cells. *RSC Advances, 6*(29), 24536-24542.

Haight, R., Barkhouse, A., Gunawan, O., Shin, B., Copel, M., Hopstaken, M., & Mitzi, D. B. (2011). Band alignment at the $Cu_2ZnSn(S_xSe_{1-x})_4$/CdS interface. *Applied Physics Letters, 98*(25), 253502.

Hall, S., Szymanski, J., & Stewart, J. (1978). Kesterite, $Cu_2(Zn, Fe)SnS_4$, and stannite, $Cu_2(Fe, Zn)SnS_4$, structurally similar but distinct minerals. *The Canadian Mineralogist, 16*(2), 131-137.

Han, D., Sun, Y., Bang, J., Zhang, Y., Sun, H.-B., Li, X.-B., & Zhang, S. (2013). Deep electron traps and origin of p-type conductivity in the earth-abundant solar-cell material Cu_2ZnSnS_4. *Physical Review B, 87*(15), 155206.

He, Y., Wang, L., Zhang, L., Li, M., Shang, X., Fang, Y., & Chen, C. (2012). Solubility limits and phase structures in epitaxial ZnOS alloy films grown by pulsed laser deposition. *Journal of Alloys and Compounds, 534*, 81-85.

Hergert, F., & Hock, R. (2007). Predicted formation reactions for the solid-state syntheses of the semiconductor materials Cu_2SnX_3 and Cu_2ZnSnX_4 (X=S, Se) starting from binary chalcogenides. *Thin Solid Films, 515*(15), 5953-5956.

Herve, P., & Vandamme, L. (1994). General relation between refractive index and energy gap in semiconductors. *Infrared Physics & Technology, 35*(4), 609-615.

Hiroi, H., Sakai, N., & Sugimoto, H. (2011). *Cd-free 5× 5cm^2-sized Cu_2ZnSnS_4 submodules.* Paper presented at the Photovoltaic Specialists Conference (PVSC), 2011 37th IEEE.

Hiroi, H., Sakai, N., Kato, T., & Sugimoto, H. (2013). *High voltage* Cu_2ZnSnS_4 *submodules by hybrid buffer layer.* Paper presented at the Photovoltaic Specialists Conference (PVSC), 2013 IEEE 39th.

Horwat, D., & Billard, A. (2007). Effects of substrate position and oxygen gas flow rate on the properties of ZnO: Al films prepared by reactive co-sputtering. *Thin Solid Films, 515*(13), 5444-5448.

Htay, M. T., Hashimoto, Y., Momose, N., Sasaki, K., Ishiguchi, H., Igarashi, S., . . . Ito, K. (2011). A cadmium-free Cu_2ZnSnS_4/ZnO hetrojunction solar cell prepared by practicable processes. *Japanese Journal of Applied Physics, 50*(3R), 032301.

Hu, J., & Gordon, R. G. (1992). Textured aluminum-doped zinc oxide thin films from atmospheric pressure chemical-vapor deposition. *Journal of Applied Physics, 71*(2), 880-890.

Hu, X., Song, G., Li, W., Peng, Y., Jiang, L., Xue, Y., . . . Hu, J. (2013). Phase-controlled synthesis and photocatalytic properties of SnS, SnS_2 and SnS/SnS_2 heterostructure nanocrystals. *Materials Research Bulletin, 48*(6), 2325-2332.

Insignares-Cuello, C., Fontané, X., Sánchez-González, Y., Placidi, M., Broussillou, C., López-García, J., . . . Izquierdo-Roca, V. (2015). Non-destructive assessment of ZnO: Al window layers in advanced Cu(In, Ga)Se_2 photovoltaic technologies. *physica status solidi (a), 212*(1), 56-60.

Ito, K., & Nakazawa, T. (1988). Electrical and optical properties of stannite-type quaternary semiconductor thin films. *Japanese Journal of Applied Physics, 27*(11R), 2094.

Jackson, P., Hariskos, D., Wuerz, R., Kiowski, O., Bauer, A., Friedlmeier, T. M., & Powalla, M. (2015). Properties of Cu(In, Ga)Se_2 solar cells with new record efficiencies up to 21.7%. *physica status solidi (RRL)-Rapid Research Letters, 9*(1), 28-31.

Jahagirdar, A. H., Kadam, A. A., & Dhere, N. G. (2006). *Role of i-ZnO in optimizing open circuit voltage of $CIGS_2$ and CIGS thin film solar cells.* Paper presented at the Photovoltaic Energy Conversion, Conference Record of the 2006 IEEE 4th World Conference on.

Janotti, A., & Van de Walle, C. G. (2009). Fundamentals of zinc oxide as a semiconductor. *Reports on Progress in Physics, 72*(12), 126501.

Jiang, F., Ikeda, S., Harada, T., & Matsumura, M. (2014). Pure sulfide Cu_2ZnSnS_4 thin film solar cells fabricated by preheating an electrodeposited metallic stack. *Advanced Energy Materials, 4*(7), 1301381.

Jimbo, K., Kimura, R., Kamimura, T., Yamada, S., Maw, W. S., Araki, H., . . . Katagiri, H. (2007). Cu_2ZnSnS_4-type thin film solar cells using abundant materials. *Thin Solid Films, 515*(15), 5997-5999.

Johnston, D. (2010). Functional requirements for component films in a solar thin-film photovoltaic/thermal panel. *Solar Energy, 84*(3), 384-389.

Jost, S. (2008). *The formation of $CuInSe_2$-based thin-film solar cell absorbers from alternative low-cost precursors.* (Ph.D. Dissertation), Universität Erlangen-Nürnberg. GERMANY.

Karthikeyan, S., Zhang, L., & Campbell, S. A. (2014). *In-situ stress and thermal stability studies of molybdenum bilayer back contacts for photovoltaic applications.* Paper presented at the Photovoltaic Specialist Conference (PVSC), 2014 IEEE 40th.

Katagiri, H. (2005). Cu_2ZnSnS_4 thin film solar cells. *Thin Solid Films, 480*, 426-432.

Katagiri, H., Ishigaki, N., Ishida, T., & Saito, K. (2001). Characterization of Cu_2ZnSnS_4 thin films prepared by vapor phase sulfurization. *Japanese Journal of Applied Physics, 40*(2R), 500.

Katagiri, H., Jimbo, K., Tahara, M., Araki, H., & Oishi, K. (2009). The influence of the composition ratio on CZTS-based thin film solar cells. *MRS Proceedings*, 1165.

Katagiri, H., Jimbo, K., Yamada, S., Kamimura, T., Maw, W. S., Fukano, T., . . . Motohiro, T. (2008). Enhanced conversion efficiencies of Cu_2ZnSnS_4-based thin film solar cells by using preferential etching technique. *Applied Physics Express, 1*(4), 041201.

Katagiri, H., Jimbo, K., Moriya, K., & Tsuchida, K. (2003). *Solar cell without environmental pollution by using CZTS thin film.* Paper presented at the Photovoltaic Energy Conversion, 2003. Proceedings of 3rd World Conference on.

Katagiri, H., Sasaguchi, N., Hando, S., Hoshino, S., Ohashi, J., & Yokota, T. (1997). Preparation and evaluation of Cu_2ZnSnS_4 thin films by sulfurization of E-B evaporated precursors. *Solar Energy Materials and Solar Cells, 49*(1-4), 407-414.

Kato, T., Hiroi, H., Sakai, N., Muraoka, S., & Sugimoto, H. (2012). *Characterization of front and back interfaces on Cu_2ZnSnS_4 thin-film solar cells.* Paper presented at the 27th European photovoltaic solar energy conference and exhibition.

Kemell, M., Ritala, M., & Leskelä, M. (2005). Thin film deposition methods for $CuInSe_2$ solar cells. *Critical Reviews in Solid State and Materials Sciences, 30*(1), 1-31.

Kessler, F., & Rudmann, D. (2004). Technological aspects of flexible CIGS solar cells and modules. *Solar Energy, 77*(6), 685-695.

Khare, A., Himmetoglu, B., Johnson, M., Norris, D. J., Cococcioni, M., & Aydil, E. S. (2012). Calculation of the lattice dynamics and Raman spectra of copper zinc tin chalcogenides and comparison to experiments. *Journal of Applied Physics, 111*(8), 083707.

Kieven, D., Grimm, A., Lauermann, I., Lux-Steiner, M. C., Palm, J., Niesen, T., & Klenk, R. (2012). Band alignment at sputtered ZnS_xO_{1-x}/Cu(In, Ga)$(Se,S)_2$ heterojunctions. *physica status solidi (RRL)-Rapid Research Letters, 6*(7), 294-296.

Kim, J., Park, C., Pawar, S., Inamdar, A. I., Jo, Y., Han, J., . . . Jung, W. (2014). Optimization of sputtered ZnS buffer for Cu_2ZnSnS_4 thin film solar cells. *Thin Solid Films, 566*, 88-92.

Kim, J. H., Choi, S. Y., Choi, M., Gershon, T., Lee, Y. S., Wang, W., . . . Chung, S. Y. (2016). Atomic-Scale Observation of Oxygen Substitution and Its Correlation with Hole-Transport Barriers in $Cu_2ZnSnSe_4$ Thin-Film Solar Cells. *Advanced Energy Materials, 6*(6).

Kim, M.-S., Yim, K.-G., Son, J.-S., & Leem, J.-Y. (2012). Effects of Al concentration on structural and optical properties of Al-doped ZnO thin films. *Bulletin of the Korean Chemical Society, 33*(4), 1235-1241.

Klenk, R. (2001). Characterisation and modelling of chalcopyrite solar cells. *Thin Solid Films, 387*(1), 135-140.

Klenk, R., Steigert, A., Rissom, T., Greiner, D., Kaufmann, C. A., Unold, T., & Lux-Steiner, M. C. (2014). Junction formation by Zn(O, S) sputtering yields CIGSe-based cells with efficiencies exceeding 18%. *Progress in Photovoltaics: Research and Applications, 22*(2), 161-165.

Kobayashi, T., Jimbo, K., Tsuchida, K., Shinoda, S., Oyanagi, T., & Katagiri, H. (2005). Investigation of Cu_2ZnSnS_4-based thin film solar cells using abundant materials. *Japanese Journal of Applied Physics, 44*(1S), 783.

Kobayashi, T., Kumazawa, T., Kao, Z. J. L., & Nakada, T. (2013). Cu(In, Ga)Se_2 thin film solar cells with a combined ALD-Zn(O, S) buffer and MOCVD-ZnO: B window layers. *Solar Energy Materials and Solar Cells, 119*, 129-133.

Koseoglu, H., Turkoglu, F., Kurt, M., Yaman, M. D., Akca, F. G., Aygun, G., & Ozyuzer, L. (2015). Improvement of optical and electrical properties of ITO thin films by electro-annealing. *Vacuum, 120*, 8-13.

Krämmer, C., Huber, C., Schnabel, T., Zimmermann, C., Lang, M., Ahlswede, E., . . . Hetterich, M. (2015). *Order-disorder related band gap changes in $Cu_2ZnSn(S, Se)_4$: impact on solar cell performance.* Paper presented at the Photovoltaic Specialist Conference (PVSC), 2015 IEEE 42nd.

Kumar, Y., Bhaskar, P. U., Babu, G. S., & Raja, V. S. (2010). Effect of copper salt and thiourea concentrations on the formation of Cu_2ZnSnS_4 thin films by spray pyrolysis. *physica status solidi (a), 207*(1), 149-156.

Kushiya, K. (2004). Development of $Cu(InGa)Se_2$-based thin-film PV modules with a $Zn(O, S, OH)_x$ buffer layer. *Solar Energy, 77*(6), 717-724.

Lee, J. C., Kang, K. H., Kim, S. K., Yoon, K. H., Park, I. J., & Song, J. (2000). RF sputter deposition of the high-quality intrinsic and n-type ZnO window layers for $Cu(In, Ga)Se_2$-based solar cell applications. *Solar Energy Materials and Solar Cells, 64*(2), 185-195.

Lewerenz, H.-J., & Jungblut, H. (2013). *Photovoltaik: Grundlagen und anwendungen*: Springer-Verlag.

Li, J., Du, Q., Liu, W., Jiang, G., Feng, X., Zhang, W., . . . Zhu, C. (2012). The band offset at CdS/Cu_2ZnSnS_4 heterojunction interface. *Electronic Materials Letters, 8*(4), 365-367.

Li, J. B., Chawla, V., & Clemens, B. M. (2012). Investigating the role of grain boundaries in CZTS and CZTSSe thin film solar cells with scanning probe microscopy. *Advanced Materials, 24*(6), 720-723.

Lin, L.-Y., Qiu, Y., Zhang, Y., & Zhang, H. (2016). Analysis of Effect of Zn(O, S) Buffer Layer Properties on CZTS Solar Cell Performance Using AMPS. *Chinese Physics Letters, 33*(10), 107801.

Liu, F., Li, Y., Zhang, K., Wang, B., Yan, C., Lai, Y., . . . Liu, Y. (2010). In situ growth of Cu_2ZnSnS_4 thin films by reactive magnetron co-sputtering. *Solar Energy Materials and Solar Cells, 94*(12), 2431-2434.

Liu, F., Zhang, K., Lai, Y., Li, J., Zhang, Z., & Liu, Y. (2010). Growth and characterization of Cu_2ZnSnS_4 thin films by dc reactive magnetron sputtering for photovoltaic applications. *Electrochemical and Solid-State Letters, 13*(11), H379-H381.

Liu, X., Cui, H., Kong, C., Hao, X., Huang, Y., Liu, F., . . . Green, M. (2015). Rapid thermal annealed Molybdenum back contact for Cu_2ZnSnS_4 thin film solar cells. *Applied Physics Letters, 106*(13), 131110.

Liu, X., Feng, Y., Cui, H., Liu, F., Hao, X., Conibeer, G., . . . Green, M. (2016). The current status and future prospects of kesterite solar cells: a brief review. *Progress in Photovoltaics: Research and Applications*.

Locmelis, S., Brünig, C., Binnewies, M., Börger, A., Becker, K., Homann, T., & Bredow, T. (2007). Optical band gap in the system $ZnO_{1-x}S_x$. An experimental and quantum chemical study. *Journal of Materials Science, 42*(6), 1965-1971.

Luque, A., & Hegedus, S. (2011). *Handbook of photovoltaic science and engineering*: John Wiley & Sons.

Maeda, T., Nakamura, S., & Wada, T. (2009). *Electronic structure and phase stability of In-free photovoltaic semiconductors, $Cu_2ZnSnSe_4$ and Cu_2ZnSnS_4 by first-principles calculation.* MRS Proceedings, 1165.

Maeda, T., Nakamura, S., & Wada, T. (2011). First-principles calculations of vacancy formation in In-free photovoltaic semiconductor $Cu_2ZnSnSe_4$. *Thin Solid Films, 519*(21), 7513-7516.

Mak, K. F., Lee, C., Hone, J., Shan, J., & Heinz, T. F. (2010). Atomically thin MoS_2: a new direct-gap semiconductor. *Physical Review Letters, 105*(13), 136805.

Masuko, K., Shigematsu, M., Hashiguchi, T., Fujishima, D., Kai, M., Yoshimura, N., . . . Matsubara, N. (2014). Achievement of more than 25% conversion efficiency with crystalline silicon heterojunction solar cell. *IEEE Journal of Photovoltaics, 4*(6), 1433-1435.

Matsui, T., Sai, H., Suezaki, T., Matsumoto, M., Saito, K., Yoshida, I., & Kondo, M. (2013). *Development of highly stable and efficient amorphous silicon based solar cells.* Paper presented at the Proc. 28th European Photovoltaic Solar Energy Conference.

McCandless, B., & Hegedus, S. (1991). *Influence of CdS window layers on thin film CdS/CdTe solar cell performance.* Paper presented at the Photovoltaic Specialists Conference, 1991., Conference Record of the Twenty Second IEEE.

Mei, Z., Zhang, N., Ouyang, S., Zhang, Y., Kako, T., & Ye, J. (2012). Photoassisted fabrication of zinc indium oxide/oxysulfide composite for enhanced photocatalytic H_2 evolution under visible-light irradiation. *Science and Technology of Advanced Materials, 13*(5), 055001.

Meyer, B., Polity, A., Farangis, B., He, Y., Hasselkamp, D., Krämer, T., & Wang, C. (2004). Structural properties and bandgap bowing of $ZnO_{1-x}S_x$ thin films deposited by reactive sputtering. *Applied Physics Letters, 85*(21), 4929-4931.

Minemoto, T., Matsui, T., Takakura, H., Hamakawa, Y., Negami, T., Hashimoto, Y., . . . Kitagawa, M. (2001). Theoretical analysis of the effect of conduction band offset of window/CIS layers on performance of CIS solar cells using device simulation. *Solar Energy Materials and Solar Cells, 67*(1), 83-88.

Mitzi, D. B., Gunawan, O., Todorov, T. K., Wang, K., & Guha, S. (2011). The path towards a high-performance solution-processed kesterite solar cell. *Solar Energy Materials and Solar Cells, 95*(6), 1421-1436.

Mohanty, B. C., Jo, Y. H., Yeon, D. H., Choi, I. J., & Cho, Y. S. (2009). Stress-induced anomalous shift of optical band gap in ZnO: Al thin films. *Applied Physics Letters, 95*(6), 062103.

Moholkar, A., Shinde, S., Babar, A., Sim, K.-U., Lee, H. K., Rajpure, K., . . . Kim, J. (2011). Synthesis and characterization of Cu_2ZnSnS_4 thin films grown by PLD: solar cells. *Journal of Alloys and Compounds, 509*(27), 7439-7446.

Moriya, K., Tanaka, K., & Uchiki, H. (2005). Characterization of Cu_2ZnSnS_4 thin films prepared by photo-chemical deposition. *Japanese Journal of Applied Physics, 44*(1S), 715.

Moriya, K., Tanaka, K., & Uchiki, H. (2007). Fabrication of Cu_2ZnSnS_4 thin-film solar cell prepared by pulsed laser deposition. *Japanese Journal of Applied Physics, 46*(9R), 5780.

Moriya, K., Tanaka, K., & Uchiki, H. (2008). Cu_2ZnSnS_4 thin films annealed in H_2S atmosphere for solar cell absorber prepared by pulsed laser deposition. *Japanese Journal of Applied Physics, 47*(1S), 602.

Moriya, K., Watabe, J., Tanaka, K., & Uchiki, H. (2006). Characterization of Cu_2ZnSnS_4 thin films prepared by photo-chemical deposition. *Physica Status Solidi (c), 3*(8), 2848-2852.

Moss, T. (1954). The interpretation of the properties of indium antimonide. *Proceedings of the Physical Society. Section B, 67*(10), 775.

Muffler, H., Bar, M., Fischer, C.-H., Gay, R., Karg, F., & Lux-Steiner, M. C. (2000). *ILGAR technology. VIII. Sulfidic buffer layers for Cu(InGa)(S, Se)$_2$solar cells prepared by ion layer gas reaction (ILGAR).* Paper presented at the Photovoltaic Specialists Conference, 2000. Conference Record of the Twenty-Eighth IEEE.

Naghavi, N., Abou-Ras, D., Allsop, N., Barreau, N., Bücheler, S., Ennaoui, A., . . . Herrero, J. (2010). Buffer layers and transparent conducting oxides for chalcopyrite Cu(In, Ga)(S, $Se)_2$ based thin film photovoltaics: present status and current developments. *Progress in Photovoltaics: Research and Applications, 18*(6), 411-433.

Nagiri, R. C. R., Yambem, S. D., Lin, Q., Burn, P. L., & Meredith, P. (2015). Room-temperature tilted-target sputtering deposition of highly transparent and low sheet resistance Al doped ZnO electrodes. *Journal of Materials Chemistry C, 3*(20), 5322-5331.

Nagoya, A., Asahi, R., & Kresse, G. (2011). First-principles study of Cu_2ZnSnS_4 and the related band offsets for photovoltaic applications. *Journal of Physics: Condensed Matter, 23*(40), 404203.

Nagoya, A., Asahi, R., Wahl, R., & Kresse, G. (2010). Defect formation and phase stability of Cu_2ZnSnS_4 photovoltaic material. *Physical Review B, 81*(11), 113202.

Nakada, T., & Mizutani, M. (2000). *Improved efficiency of Cu(In, Ga) Se_2 thin film solar cells with chemically deposited ZnS buffer layers by air-annealing-formation of homojunction by solid phase diffusion.* Paper presented at the Photovoltaic Specialists Conference, 2000. Conference Record of the Twenty-Eighth IEEE.

Nakamura, M., Kouji, Y., Chiba, Y., Hakuma, H., Kobayashi, T., & Nakada, T. (2013). *Achievement of 19.7% efficiency with a small-sized Cu(InGa)$(SeS)_2$ solar cells prepared by sulfurization after selenizaion process with Zn-based buffer.* Paper presented at the Photovoltaic Specialists Conference (PVSC), 2013 IEEE 39th.

Nakayama, N., & Ito, K. (1996). Sprayed films of stannite Cu_2ZnSnS_4. *Applied Surface Science, 92*, 171-175.

Namin, A., Jivacate, C., Chenvidhya, D., Kirtikara, K., & Thongpron, J. (2012). Construction of Tungsten Halogen, Pulsed LED, and Combined Tungsten Halogen-LED Solar Simulators for Solar Cell-Characterization and Electrical Parameters Determination. *International Journal of Photoenergy,* 2012, 527820.

Nandur, A., & White, B. (2014). *Growth of Cu_2ZnSnS_4 (CZTS) by Pulsed Laser Deposition for Thin film Photovoltaic Absorber Material.* Paper presented at the APS Meeting Abstracts.

Nelson, J. (2003). *The physics of solar cells*: World Scientific Publishing Co Inc.

Neuschitzer, M., Sanchez, Y., López-Marino, S., Xie, H., Fairbrother, A., Placidi, M., . . . Saucedo, E. (2015). Optimization of CdS buffer layer for high-performance $Cu_2ZnSnSe_4$ solar cells and the effects of light soaking: elimination of crossover and red kink. *Progress in Photovoltaics: Research and Applications, 23*(11), 1660-1667.

Nguyen, H. C., Trinh, T. T., Le, T., Tran, C. V., Tran, T., Park, H., . . . Yi, J. (2011). The mechanisms of negative oxygen ion formation from Al-doped ZnO target and the improvements in electrical and optical properties of thin films using off-axis dc magnetron sputtering at low temperature. *Semiconductor Science and Technology, 26*(10), 105022.

Nozaki, H., Shibata, K., & Ohhashi, N. (1991). Metallic hole conduction in CuS. *Journal of Solid State Chemistry, 91*(2), 306-311.

NREL, L. K. (2015). Best Research-Cell Efficiencies. *Research Cell Efficiency Records*.

Ogah, O. E., Zoppi, G., Forbes, I., & Miles, R. (2009). Thin films of tin sulphide for use in thin film solar cell devices. *Thin Solid Films, 517*(7), 2485-2488.

Olekseyuk, I., Dudchak, I., & Piskach, L. (2004). Phase equilibria in the Cu_2S–ZnS–SnS_2 system. *Journal of Alloys and Compounds, 368*(1), 135-143.

Ou, S. L., Wuu, D. S., Liu, S. P., Fu, Y. C., Huang, S. C., & Horng, R. H. (2011). Pulsed laser deposition of ITO/AZO transparent contact layers for GaN LED applications. *Optics express, 19*(17), 16244-16251.

Özgür, H. M. Ü., & Morkoç, H. (2007). Zinc Oxide Fundamentals, Materials and Device Technology: Weinheim: WILEY VCH Verlag GmbH & Co. KGaA.

Özgür, Ü., Alivov, Y. I., Liu, C., Teke, A., Reshchikov, M., Doğan, S., . . . Morkoc, H. (2005). A comprehensive review of ZnO materials and devices. *Journal of Applied Physics, 98*(4), 11.

Paier, J., Asahi, R., Nagoya, A., & Kresse, G. (2009). Cu_2ZnSnS_4 as a potential photovoltaic material: a hybrid Hartree-Fock density functional theory study. *Physical Review B, 79*(11), 115126.

Pal, M., Mathews, N., Gonzalez, R. S., & Mathew, X. (2013). Synthesis of Cu_2ZnSnS_4 nanocrystals by solvothermal method. *Thin Solid Films, 535*, 78-82.

Pamplin, B. (1960). Super-cell structure of semiconductors. *Nature, 188*(4745), 136-137.

Pan, H., Yang, T., Yao, B., Deng, R., Sui, R., Gao, L., & Shen, D. (2010). Characterization and properties of $ZnO_{1-x}S_x$ alloy films fabricated by radio-frequency magnetron sputtering. *Applied Surface Science, 256*(14), 4621-4625.

Pandey, S. K., Pandey, S., Pandey, A. C., & Mehrotra, G. (2013). Zinc oxysulfide ternary alloy nanocrystals: A bandgap modulated photocatalyst. *Applied Physics Letters, 102*(23), 233110.

Pandey, S. K., Pandey, S., Parashar, V., Yadav, R. S., Mehrotra, G., & Pandey, A. C. (2014). Bandgap engineering of colloidal zinc oxysulfide via lattice substitution with sulfur. *Nanoscale, 6*(3), 1602-1606.

Park, S.-N., Sung, S.-J., Son, D.-H., Kim, D.-H., Gansukh, M., Cheong, H., & Kang, J.-K. (2014). Solution-processed Cu_2ZnSnS_4 absorbers prepared by appropriate inclusion and removal of thiourea for thin film solar cells. *RSC Advances, 4*(18), 9118-9125.

Paul, G., Ghosh, R., Bera, S., Bandyopadhyay, S., Sakurai, T., & Akimoto, K. (2008). Deep level transient spectroscopy of cyanide treated polycrystalline p-Cu_2O/n-ZnO solar cell. *Chemical Physics Letters, 463*(1), 117-120.

Persson, C. (2010). Electronic and optical properties of Cu_2ZnSnS_4 and $Cu_2ZnSnSe_4$. *Journal of Applied Physics, 107*(5), 053710.

Persson, C., Platzer-Björkman, C., Malmström, J., Törndahl, T., & Edoff, M. (2006). Strong valence-band offset bowing of $ZnO_{1-x}S_x$ enhances p-type nitrogen doping of ZnO-like alloys. *Physical Review Letters, 97*(14), 146403.

Physics-and-Radio-Electronics. (2013). P-N Junction. Retrieved from http://www.physics-and-radio-electronics.com.

Platzer-Bjorkman, C., Kessler, J., & Stolt, L. (2003). *Atomic layer deposition of Zn(O, S) buffer layers for high efficiency Cu(In, Ga)Se_2 solar cells.* Paper presented at the Photovoltaic Energy Conversion, 2003. Proceedings of 3rd World Conference on.

Platzer-Björkman, C., Frisk, C., Larsen, J., Ericson, T., Li, S.-Y., Scragg, J., . . . Törndahl, T. (2015). Reduced interface recombination in Cu_2ZnSnS_4 solar cells with atomic layer deposition $Zn_{1-x}Sn_xO_y$ buffer layers. *Applied Physics Letters, 107*(24), 243904.

Platzer-Björkman, C., Lu, J., Kessler, J., & Stolt, L. (2003). Interface study of $CuInSe_2$/ZnO and Cu(In, Ga)Se_2/ZnO devices using ALD ZnO buffer layers. *Thin Solid Films, 431*, 321-325.

Platzer-Björkman, C., Törndahl, T., Abou-Ras, D., Malmström, J., Kessler, J., & Stolt, L. (2006). Zn(O, S) buffer layers by atomic layer deposition in Cu(In, Ga)Se_2 based thin film solar cells: band alignment and sulfur gradient. *Journal of Applied Physics, 100*(4), 044506.

Prabhakar, T., & Nagaraju, J. (2010). *Ultrasonic spray pyrolysis of CZTS solar cell absorber layers and characterization studies.* Paper presented at the Photovoltaic Specialists Conference (PVSC), 2010 35th IEEE.

Pudov, A., Kanevce, A., Al-Thani, H., Sites, J., & Hasoon, F. (2005). Secondary barriers in CdS–$CuIn_{1-x}Ga_xSe_2$ solar cells. *Journal of Applied Physics, 97*(6), 064901.

Rajeshmon, V., Kartha, C. S., Vijayakumar, K., Sanjeeviraja, C., Abe, T., & Kashiwaba, Y. (2011). Role of precursor solution in controlling the opto-electronic properties of spray pyrolysed Cu_2ZnSnS_4 thin films. *Solar Energy, 85*(2), 249-255.

Ramanathan, K., Contreras, M. A., Perkins, C. L., Asher, S., Hasoon, F. S., Keane, J., . . . Noufi, R. (2003). Properties of 19.2% efficiency ZnO/CdS/$CuInGaSe_2$ thin-film solar cells. *Progress in Photovoltaics: Research and Applications, 11*(4), 225-230.

Ramasamy, K., Malik, M. A., & O'Brien, P. (2011). The chemical vapor deposition of Cu_2ZnSnS_4 thin films. *Chemical Science, 2*(6), 1170-1172.

Rau, U., & Schmidt, M. (2001). Electronic properties of ZnO/CdS/Cu(In, Ga)Se_2 solar cells-aspects of heterojunction formation. *Thin Solid Films, 387*(1), 141-146.

Redinger, A., Berg, D. M., Dale, P. J., & Siebentritt, S. (2011). The consequences of kesterite equilibria for efficient solar cells. *Journal of the American Chemical Society, 133*(10), 3320-3323.

Reeber, R. R. (1970). Lattice parameters of ZnO from 4.2 to 296 K. *Journal of Applied Physics, 41*(13), 5063-5066.

Repins, I., Vora, N., Beall, C., Wei, S.-H., Yan, Y., Romero, M., . . . Young, M. (2011). *Kesterites and chalcopyrites: a comparison of close cousins.* Paper presented at the MRS proceedings.

Rey, G., Weiss, T., Sendler, J., Finger, A., Spindler, C., Werner, F., . . . Siebentritt, S. (2016). Ordering kesterite improves solar cells: A low temperature post-deposition annealing study. *Solar Energy Materials and Solar Cells, 151*, 131-138.

Rios, L. E. V., Neldner, K., Gurieva, G., & Schorr, S. (2016). Existence of off-stoichiometric single phase kesterite. *Journal of Alloys and Compounds, 657*, 408-413.

Romeo, A., Gysel, R., Buzzi, S., & Abou-Ras, D. (2004). *DL B7tzner, D. Rudmann, H. Zogg, AN Tiwari.* Paper presented at the Proceedings 14th Photovoltaic Science and Engineering Conference (PVSEC-14), Bangkok, Thailand.

Romeo, N., Bosio, A., & Romeo, A. (2010). An innovative process suitable to produce high-efficiency CdTe/CdS thin-film modules. *Solar Energy Materials and Solar Cells, 94*(1), 2-7.

Rousseau, D., Bauman, R. P., & Porto, S. (1981). Normal mode determination in crystals. *Journal of Raman Spectroscopy, 10*(1), 253-290.

Rudigier, E., Luck, I., & Scheer, R. (2003). Quality assessment of $CuInS_2$-based solar cells by Raman scattering. *Applied Physics Letters, 82*(24), 4370-4372.

Russo, V., Ghidelli, M., Gondoni, P., Casari, C., & Li Bassi, A. (2014). Multi-wavelength Raman scattering of nanostructured Al-doped zinc oxide. *Journal of Applied Physics, 115*(7), 073508.

Sáez-Araoz, R., Ennaoui, A., Kropp, T., Veryaeva, E., Niesen, T., & Lux-Steiner, M. C. (2008). Use of different Zn precursors for the deposition of Zn(S, O) buffer layers by chemical bath for chalcopyrite based Cd-free thin-film solar cells. *physica status solidi (a), 205*(10), 2330-2334.

Sai, H., Matsui, T., Koida, T., Matsubara, K., Kondo, M., Sugiyama, S., . . . Yoshida, I. (2015). Triple-junction thin-film silicon solar cell fabricated on periodically textured substrate with a stabilized efficiency of 13.6%. *Applied Physics Letters, 106*(21), 213902.

Sanders, B., & Kitai, A. (1992). Zinc oxysulfide thin films grown by atomic layer deposition. *Chemistry of Materials, 4*(5), 1005-1011.

Santoni, A., Biccari, F., Malerba, C., Valentini, M., Chierchia, R., & Mittiga, A. (2013). Valence band offset at the CdS/Cu_2ZnSnS_4 interface probed by x-ray photoelectron spectroscopy. *Journal of Physics D: Applied Physics, 46*(17), 175101.

Sardashti, K., Haight, R., Gokmen, T., Wang, W., Chang, L. Y., Mitzi, D. B., & Kummel, A. C. (2015). Impact of Nanoscale Elemental Distribution in High-Performance Kesterite Solar Cells. *Advanced Energy Materials, 5*(10).

Schorr, S. (2007). Structural aspects of adamantine like multinary chalcogenides. *Thin Solid Films, 515*(15), 5985-5991.

Schorr, S. (2011). The crystal structure of kesterite type compounds: A neutron and X-ray diffraction study. *Solar Energy Materials and Solar Cells, 95*(6), 1482-1488.

Schorr, S., Weber, A., Honkimäki, V., & Schock, H.-W. (2009). In-situ investigation of the kesterite formation from binary and ternary sulphides. *Thin Solid Films, 517*(7), 2461-2464.

Schurr, R., Hölzing, A., Jost, S., Hock, R., Voβ, T., Schulze, J., . . . Weber, A. (2009). The crystallisation of Cu_2ZnSnS_4 thin film solar cell absorbers from co-electroplated Cu–Zn–Sn precursors. *Thin Solid Films, 517*(7), 2465-2468.

Scofield, J. H., Duda, A., Albin, D., Ballard, B., & Predecki, P. (1995). Sputtered molybdenum bilayer back contact for copper indium diselenide-based polycrystalline thin-film solar cells. *Thin Solid Films, 260*(1), 26-31.

Scragg, J. J. (2010). *Studies of Cu_2ZnSnS_4 films prepared by sulfurisation of electrodeposited precursors.* (Ph.D. Dissertation), University of Bath, UK.

Scragg, J. J., Dale, P. J., Colombara, D., & Peter, L. M. (2012). Thermodynamic Aspects of the Synthesis of Thin-Film Materials for Solar Cells. *ChemPhysChem, 13*(12), 3035-3046.

Scragg, J. J., Dale, P. J., Peter, L. M., Zoppi, G., & Forbes, I. (2008). New routes to sustainable photovoltaics: evaluation of Cu_2ZnSnS_4 as an alternative absorber material. *physica status solidi (b), 245*(9), 1772-1778.

Scragg, J. J., Ericson, T., Kubart, T., Edoff, M., & Platzer-Björkman, C. (2011). Chemical insights into the instability of Cu_2ZnSnS_4 films during annealing. *Chemistry of Materials, 23*(20), 4625-4633.

Scragg, J. J., Kubart, T., Wätjen, J. T., Ericson, T., Linnarsson, M. K., & Platzer-Björkman, C. (2013). Effects of back contact instability on Cu_2ZnSnS_4 devices and processes. *Chemistry of Materials, 25*(15), 3162-3171.

Scragg, J. J., Watjen, J. T., Edoff, M., Ericson, T., Kubart, T., & Platzer-Björkman, C. (2012). A detrimental reaction at the molybdenum back contact in $Cu_2ZnSn(S, Se)_4$ thin-film solar cells. *Journal of the American Chemical Society, 134*(47), 19330-19333.

Sekiguchi, K., Tanaka, K., Moriya, K., & Uchiki, H. (2006). Epitaxial growth of Cu_2ZnSnS_4 thin films by pulsed laser deposition. *Physica Status Solidi (c), 3*(8), 2618-2621.

Seol, J.-S., Lee, S.-Y., Lee, J.-C., Nam, H.-D., & Kim, K.-H. (2003). Electrical and optical properties of Cu_2ZnSnS_4 thin films prepared by rf magnetron sputtering process. *Solar Energy Materials and Solar Cells, 75*(1), 155-162.

Serrano, J., Romero, A., Manjon, F., Lauck, R., Cardona, M., & Rubio, A. (2004). Pressure dependence of the lattice dynamics of ZnO: An ab initio approach. *Physical Review B, 69*(9), 094306.

Shibata, T., Muranushi, Y., Miura, T., & Kishi, T. (1990). Photoconductive properties of single-crystal 2H-SnS_2. *Journal of Physics and Chemistry of Solids, 51*(11), 1297-1300.

Shin, B., Gunawan, O., Zhu, Y., Bojarczuk, N. A., Chey, S. J., & Guha, S. (2013). Thin film solar cell with 8.4% power conversion efficiency using an earth-abundant Cu_2ZnSnS_4 absorber. *Progress in Photovoltaics: Research and Applications, 21*(1), 72-76.

Shin, B., Zhu, Y., Bojarczuk, N. A., Jay Chey, S., & Guha, S. (2012). Control of an interfacial $MoSe_2$ layer in $Cu_2ZnSnSe_4$ thin film solar cells: 8.9% power conversion efficiency with a TiN diffusion barrier. *Applied Physics Letters, 101*(5), 053903.

Shockley, W., & Queisser, H. J. (1961). Detailed balance limit of efficiency of p-n junction solar cells. *Journal of Applied Physics, 32*(3), 510-519.

Siebentritt, S. (2004). Alternative buffers for chalcopyrite solar cells. *Solar Energy, 77*(6), 767-775.

Singh, U. P., & Patra, S. P. (2010). Progress in Polycrystalline Thin-Film Cu(In, Ga) Solar Cells. *International Journal of Photoenergy, 2010*.

Sinsermsuksakul, P., Hartman, K., Bok Kim, S., Heo, J., Sun, L., Hejin Park, H., . . . Gordon, R. G. (2013). Enhancing the efficiency of SnS solar cells via band-offset engineering with a zinc oxysulfide buffer layer. *Applied Physics Letters, 102*(5), 053901.

Sissoko, G., & Mbodji, S. (2011). A method to determine the solar cell resistances from single IV characteristic curve considering the junction recombination velocity (Sf). *International Journal of Pure and Applied Sciences and Technology, 6*(2), 103-114.

Solar, F. (2011). Press Release. Retrieved from http. *investor. firstsolar. com/releasedetail. cfm.*

Song, T. (2013). *Distortions to current-voltage curves of cigs cells with sputtered Zn(O, S) buffer layers.* (Ph.D. Dissertation), Colorado State University, USA.

Srikant, V., & Clarke, D. R. (1998). On the optical band gap of zinc oxide. *Journal of Applied Physics, 83*(10), 5447-5451.

Srinatha, N., No, Y., Kamble, V. B., Chakravarty, S., Suriyamurthy, N., Angadi, B., . . . Choi, W. (2016). Effect of RF power on the structural, optical and gas sensing properties of RF-sputtered Al doped ZnO thin films. *RSC Advances, 6*(12), 9779-9788.

Staebler, D., & Wronski, C. (1977). Reversible conductivity changes in discharge-produced amorphous Si. *Applied Physics Letters, 31*(4), 292-294.

Su, Z., Sun, K., Han, Z., Cui, H., Liu, F., Lai, Y., . . . Green, M. A. (2014). Fabrication of Cu_2ZnSnS_4 solar cells with 5.1% efficiency via thermal decomposition and reaction using a non-toxic sol–gel route. *Journal of Materials Chemistry A, 2*(2), 500-509.

Sugimoto, H., Hiroi, H., Sakai, N., Muraoka, S., & Katou, T. (2012). *Over 8% efficiency* Cu_2ZnSnS_4 *submodules with ultra-thin absorber.* Paper presented at the Photovoltaic Specialists Conference (PVSC), 2012 38th IEEE.

Sun, L., Haight, R., Sinsermsuksakul, P., Bok Kim, S., Park, H. H., & Gordon, R. G. (2013). Band alignment of SnS/Zn(O, S) heterojunctions in SnS thin film solar cells. *Applied Physics Letters, 103*(18), 181904.

Tajima, S., Umehara, M., Hasegawa, M., Mise, T., & Itoh, T. (2017). Cu_2ZnSnS_4 photovoltaic cell with improved efficiency fabricated by high-temperature annealing after CdS buffer-layer deposition. *Progress in Photovoltaics: Research and Applications, 25*(1), 14-22.

Tanaka, H., Shimakawa, T., Miyata, T., Sato, H., & Minami, T. (2005). Effect of AZO film deposition conditions on the photovoltaic properties of AZO–Cu_2O heterojunctions. *Applied Surface Science, 244*(1), 568-572.

Tanaka, K., Fukui, Y., Moritake, N., & Uchiki, H. (2011). Chemical composition dependence of morphological and optical properties of Cu_2ZnSnS_4 thin films deposited by sol–gel sulfurization and Cu_2ZnSnS_4 thin film solar cell efficiency. *Solar Energy Materials and Solar Cells, 95*(3), 838-842.

Tanaka, K., Moritake, N., Oonuki, M., & Uchiki, H. (2008). Pre-annealing of precursors of Cu_2ZnSnS_4 thin films prepared by sol–gel sulfurizing method. *Japanese Journal of Applied Physics, 47*(1S), 598.

Tanaka, K., Oonuki, M., Moritake, N., & Uchiki, H. (2009). Cu_2ZnSnS_4 thin film solar cells prepared by non-vacuum processing. *Solar Energy Materials and Solar Cells, 93*(5), 583-587.

Tanaka, T., Nagatomo, T., Kawasaki, D., Nishio, M., Guo, Q., Wakahara, A., . . . Ogawa, H. (2005). Preparation of Cu_2ZnSnS_4 thin films by hybrid sputtering. *Journal of Physics and Chemistry of Solids, 66*(11), 1978-1981.

Tanaka, T., Yoshida, A., Saiki, D., Saito, K., Guo, Q., Nishio, M., & Yamaguchi, T. (2010). Influence of composition ratio on properties of Cu_2ZnSnS_4 thin films fabricated by co-evaporation. *Thin Solid Films, 518*(21), S29-S33.

Tao, J., Zhang, K., Zhang, C., Chen, L., Cao, H., Liu, J., . . . Chu, J. (2015). A sputtered CdS buffer layer for co-electrodeposited Cu_2ZnSnS_4 solar cells with 6.6% efficiency. *Chemical Communications, 51*(51), 10337-10340.

Terasako, T., Yagi, M., Ishizaki, M., Senda, Y., Matsuura, H., & Shirakata, S. (2007). Growth of zinc oxide films and nanowires by atmospheric-pressure chemical vapor deposition using zinc powder and water as source materials. *Surface and Coatings Technology, 201*(22), 8924-8930.

Thangaraju, B., & Kaliannan, P. (2000). Spray pyrolytic deposition and characterization of SnS and SnS_2 thin films. *Journal of Physics D: Applied Physics, 33*(9), 1054.

Timmo, K., Kauk-Kuusik, M., Pilvet, M., Raadik, T., Altosaar, M., Danilson, M., . . . Ernits, K. (2016). Influence of order-disorder in Cu_2ZnSnS_4 powders on the performance of monograin layer solar cells. *Thin Solid Films*, 633, 122-126.

Todorov, T. K., Tang, J., Bag, S., Gunawan, O., Gokmen, T., Zhu, Y., & Mitzi, D. B. (2013). Beyond 11% efficiency: characteristics of state-of-the-art $Cu_2ZnSn(S, Se)_4$ solar cells. *Advanced Energy Materials, 3*(1), 34-38.

Tsai, T. C., & Staack, D. (2011). Low-temperature Polymer Deposition in Ambient Air Using a Floating-electrode Dielectric Barrier Discharge Jet. *Plasma Processes and Polymers, 8*(6), 523-534.

Turcu, M., Pakma, O., & Rau, U. (2002). Interdependence of absorber composition and recombination mechanism in $Cu(In, Ga)(Se, S)_2$ heterojunction solar cells. *Applied Physics Letters, 80*(14), 2598-2600.

Valakh, M. Y., Kolomys, O., Ponomaryov, S., Yukhymchuk, V., Babichuk, I., Izquierdo-Roca, V., . . . Schorr, S. (2013). Raman scattering and disorder effect in Cu_2ZnSnS_4. *physica status solidi (RRL)-Rapid Research Letters, 7*(4), 258-261.

Waalkes, M. P. (2000). Cadmium carcinogenesis in review. *Journal of Inorganic Biochemistry, 79*(1), 241-244.

Wadia, C., Alivisatos, A. P., & Kammen, D. M. (2009). Materials availability expands the opportunity for large-scale photovoltaics deployment. *Environmental Science & Technology, 43*(6), 2072-2077.

Wagner, R., & Wiemhöfer, H.-D. (1983). Hall effect and conductivity in thin films of low temperature chalcocite Cu_2S at 20 °C as a function of stoichiometry. *Journal of Physics and Chemistry of Solids, 44*(8), 801-805.

Walsh, A., Chen, S., Wei, S. H., & Gong, X. G. (2012). Kesterite Thin-Film Solar Cells: Advances in Materials Modelling of Cu_2ZnSnS_4. *Advanced Energy Materials, 2*(4), 400-409.

Wang, F., He, H., Ye, Z., Zhu, L., Tang, H., & Zhang, Y. (2005). Raman scattering and photoluminescence of quasi-aligned ternary ZnCdO nanorods. *Journal of Physics D: Applied Physics, 38*(16), 2919.

Wang, H., Xu, J., Ren, M., & Yang, L. (2008). Room temperature deposition and properties of ZnO: Al thin films by nonreactive DC magnetron sputtering. *Journal of Materials Science: Materials in Electronics, 19*(11), 1135-1139.

Wang, K., Gunawan, O., Todorov, T., Shin, B., Chey, S., Bojarczuk, N., . . . Guha, S. (2010). Thermally evaporated Cu_2ZnSnS_4 solar cells. *Applied Physics Letters, 97*(14), 143508.

Wang, K., Shin, B., Reuter, K. B., Todorov, T., Mitzi, D. B., & Guha, S. (2011). Structural and elemental characterization of high efficiency Cu_2ZnSnS_4 solar cells. *Applied Physics Letters, 98*(5), 051912.

Wang, W., Winkler, M. T., Gunawan, O., Gokmen, T., Todorov, T. K., Zhu, Y., & Mitzi, D. B. (2014). Device characteristics of CZTSSe thin-film solar cells with 12.6% efficiency. *Advanced Energy Materials, 4*(7).

Wang, X., Xu, J., Yu, X., Xue, K., Yu, J., & Zhao, X. (2007). Structural evidence of secondary phase segregation from the Raman vibrational modes in $Zn_{1-x}Co_xO$ ($0< x< 0.6$). *Applied Physics Letters, 91*(3), 031908.

Wang, Y., Huang, Y., Lee, A. Y., Wang, C. F., & Gong, H. (2012). Influence of sintering temperature on screen printed Cu_2ZnSnS_4 (CZTS) films. *Journal of alloys and compounds, 539*, 237-241.

Wangperawong, A., King, J., Herron, S., Tran, B., Pangan-Okimoto, K., & Bent, S. (2011). Aqueous bath process for deposition of Cu_2ZnSnS_4 photovoltaic absorbers. *Thin Solid Films, 519*(8), 2488-2492.

Wasa, K., Hayakawa, S., & Hada, T. (1971). Electrical and optical properties of sputtered np ZnO–Si heterojunctions. *Japanese Journal of Applied Physics, 10*(12), 1732.

Washio, T., Shinji, T., Tajima, S., Fukano, T., Motohiro, T., Jimbo, K., & Katagiri, H. (2012). 6% Efficiency Cu_2ZnSnS_4-based thin film solar cells using oxide precursors by open atmosphere type CVD. *Journal of Materials Chemistry, 22*(9), 4021-4024.

Weber, A. (2009). *Growth of thin films of the material system Cu-Zn-Sn-S.* (Ph.D. Dissertation), Friedrich-Alexander-Universität Erlangen-Nürnberg, GERMANY.

Weber, A., Mainz, R., Unold, T., Schorr, S., & Schock, H. W. (2009). In-situ XRD on formation reactions of Cu_2ZnSnS_4 thin films. *Physica Status Solidi (c), 6*(5), 1245-1248.

Weinhardt, L., Fuchs, O., Groß, D., Storch, G., Umbach, E., Dhere, N. G., . . . Heske, C. (2005). Band alignment at the CdS/$Cu(In,Ga)S_2$ interface in thin-film solar cells. *Applied Physics Letters, 86*(6), 062109.

Williams, D. (2004). Sun fact sheet. NASA.

Witte, W., Abou-Ras, D., & Hariskos, D. (2013). Chemical bath deposition of Zn(O, S) and CdS buffers: Influence of Cu(In, Ga)Se_2 grain orientation. *Applied Physics Letters, 102*(5), 051607.

Wu, C., Hu, Z., Wang, C., Sheng, H., Yang, J., & Xie, Y. (2007). Hexagonal Cu_2SnS_3 with metallic character: Another category of conducting sulfides. *Applied Physics Letters, 91*(14), 143104.

Xinkun, W., Wei, L., Shuying, C., Yunfeng, L., & Hongjie, J. (2012). Photoelectric properties of Cu_2ZnSnS_4 thin films deposited by thermal evaporation. *Journal of Semiconductors, 33*(2), 022002.

Xu, X., Lau, S., Chen, J., Chen, G., & Tay, B. (2001). Polycrystalline ZnO thin films on Si (100) deposited by filtered cathodic vacuum arc. *Journal of Crystal Growth, 223*(1), 201-205.

Yahia, S. B., Znaidi, L., Kanaev, A., & Petitet, J. (2008). Raman study of oriented ZnO thin films deposited by sol–gel method. *Spectrochimica Acta Part A: Molecular and Biomolecular Spectroscopy, 71*(4), 1234-1238.

Yan, C., Liu, F., Song, N., Ng, B. K., Stride, J. A., Tadich, A., & Hao, X. (2014). Band alignments of different buffer layers (CdS, Zn(O, S), and In_2S_3) on Cu_2ZnSnS_4. *Applied Physics Letters, 104*(17), 173901.

Yang, K. J., Sim, J. H., Jeon, B., Son, D. H., Kim, D. H., Sung, S. J., . . . Kim, J. (2015). Effects of Na and MoS_2 on Cu_2ZnSnS_4 thin-film solar cell. *Progress in Photovoltaics: Research and Applications, 23*(7), 862-873.

Yazici, S., Olgar, M. A., Akca, F. G., Cantas, A., Kurt, M., Aygun, G., . . . Ozyuzer, L. (2015). Growth of Cu_2ZnSnS_4 absorber layer on flexible metallic substrates for thin film solar cell applications. *Thin Solid Films, 589*, 563-573.

Yeh, M.-Y., Lei, P.-H., Lin, S.-H., & Yang, C.-D. (2016). Copper-Zinc-Tin-Sulfur Thin Film Using Spin-Coating Technology. *Materials, 9*(7), 526.

Yoo, H., & Kim, J. (2011). Comparative study of Cu_2ZnSnS_4 film growth. *Solar Energy Materials and Solar Cells, 95*(1), 239-244.

Yoo, Y.-Z., Chikyow, T., Ahmet, P., Kawasaki, M., Makino, T., Segawa, Y., & Koinuma, H. (2001). High-temperature epitaxy of metastable sulfides on oxide substrates using stoichiometric transportation. *Advanced Materials, 13*(21), 1624.

Yoo, Y.-Z., Jin, Z.-W., Chikyow, T., Fukumura, T., Kawasaki, M., & Koinuma, H. (2002). S doping in ZnO film by supplying ZnS species with pulsed-laser-deposition method. *Applied Physics Letters, 81*(20), 3798-3800.

Yousfi, E., Asikainen, T., Pietu, V., Cowache, P., Powalla, M., & Lincot, D. (2000). Cadmium-free buffer layers deposited by atomic later epitaxy for copper indium diselenide solar cells. *Thin Solid Films, 361*, 183-186.

Zeng, J. N., Low, J. K., Ren, Z. M., Liew, T., & Lu, Y. F. (2002). Effect of deposition conditions on optical and electrical properties of ZnO films prepared by pulsed laser deposition. *Applied Surface Science, 197*, 362-367.

ZHANG, J., Lexi, S., Yujun, F., & Erqing, X. (2006). Cu_2ZnSnS_4 thin films prepared by sulfurization of ion beam sputtered precursor and their electrical and optical properties. *Rare Metals, 25*(6), 315-319.

Zhang, J., & Shao, L. (2009). Cu_2ZnSnS_4 thin films prepared by sulfurizing different multilayer metal precursors. *Science in China Series E: Technological Sciences, 52*(1), 269-272.

Zhao, H., & Persson, C. (2011). Optical properties of Cu(In, Ga)Se_2 and $Cu_2ZnSn(S, Se)_4$. *Thin Solid Films, 519*(21), 7508-7512.

Zhou, Z., Wang, Y., Xu, D., & Zhang, Y. (2010). Fabrication of Cu_2ZnSnS_4 screen printed layers for solar cells. *Solar Energy Materials and Solar Cells, 94*(12), 2042-2045.

Zhu, X.-G., Long, S. P., & Ort, D. R. (2008). What is the maximum efficiency with which photosynthesis can convert solar energy into biomass?. *Current Opinion in Biotechnology, 19*(2), 153-159.

Zimmermann, U., Ruth, M., & Edoff, M. (2006). *Cadmium-free CIGS mini-modules with ALD-grown Zn(O, S)-based buffer layers*. Paper presented at the 21st Eproceedings of the international conference held in Dresden, Germany, 4-8 September 2006 European Photovoltaic Solar Energy Conference.

VİTA

Fulya Köseoğlu was born in İzmir, Turkey, on December 6, 1984, the daughter of Feyzi Türkoğlu and Tülay Türkoğlu. After finishing Bornova Anatolian High School, she went on to the İzmir Institute of Technology and she completed a Bachelor of Science in Physics in June of 2007. In September 2007, she entered the graduate school at İzmir Institute of Technology. She received an M.Sc. degree in June 2010 in Physics and Ph.D. degree in June 2017 in Materials Science and Engineering from İzmir Institute of Technology. She worked as a research assistant between 2007 and 2017 at department of Physics, İzmir Institute of Technology. She has also experience on various deposition techniques such as evaporation and magnetron sputtering technique, and characterization techniques such as electrical and optical characterization.

Some Publications:

Y.Demirhan, H.Saglam, **F. Turkoglu**, H. Alaboz, L. Ozyuzer, N. Miyakawa and K. Kadowaki, "Area dependence and influence of crystal inhomogeneity on superconducting properties of Bi2212 mesa structures", *Vacuum* **120**, 89–94 (2015)

Hasan Koseoglu, **Fulya Turkoglu**, Mutlu D. Yaman, Metin Kurt, Fatime G. Akça, Gülnur Aygün, Lütfi Özyüzer, "Improvement of optical and electrical properties of ITO thin films by electro-annealing", *Vacuum* **120**, 8-13 (2015)

F. Turkoglu, L. Ozyuzer, H. Koseoglu Y. Demirhan, S. Preu, S. Malzer, Y. Simsek, H.B. Wang, P. Muller, "Emission of the THz waves from large area mesas of superconducting $Bi_2Sr_2CaCu_2O_{8+\delta}$ by the injection of spin polarized current", *Physica C: Superconductivity* **491**, 7-10 (2013)

F. Turkoglu, H. Koseoglu, Y. Demirhan, L Ozyuzer, S Preu, S Malzer, Y Simsek, P Müller, T Yamamoto and K Kadowaki, "Interferometer measurements of terahertz waves from $Bi_2Sr_2CaCu_2O_{8+\delta}$ mesas", *Superconductor Science and Technology* **25**, 125004 (2012)

H. Koseoglu, **F. Turkoglu**, Y. Simsek, L. Ozyuzer, "The Fabrication of THz Emitting Mesas by Reactive Ion-Beam Etching of Superconducting Bi2212 with Multilayer Masks", *Journal of Superconductivity and Novel Magnetism* **24**, 1083-1086 (2011)

L. Ozyuzer, Y. Simsek, H. Koseoglu, **F. Turkoglu**, C Kurter, U Welp, AE Koshelev, KE Gray, WK Kwok, T Yamamoto, K Kadowaki, Y Koval, HB Wang and P Müller, "Terahertz wave emission from intrinsic Josephson junctions in high-Tc superconductors", *Superconductor Science and Technology* **22**, 114009 (2009)

Y. Demirhan, **F. Turkoglu**, H. Koseoglu, H. Saglam, N. Miyakawa K. Kadowaki and L. Ozyuzer, "Inhomogeneity of Micron-Sized Triple Terahertz Emitters Fabricated from Intrinsic Josephson Junctions in Single Crystal $Bi_2Sr_2CaCu_2O_{8+\delta}$ ", *Springer: NATO Science for Peace and Security Series B: Physics and Biophysics, Terahertz and Mid Infrared Radiation: Detection of Explosives and CBRN Edited by Mauro F. Pereira and Oleksiy Shulika* **Book Chapter**, pp 95-102 (2014)